Nonequilibrium dynamics of Coulomb crystals in double well traps

Dissertation zur Erlangung des Doktorgrades
an der Fakultät für Mathematik, Informatik und Naturwissenschaften,
Fachbereich Physik der Universität Hamburg

vorgelegt von
Andrea Klumpp
aus Königs Wusterhausen

Hamburg, Juli 2018

Gutachter der Dissertation:	Prof. Dr. Peter Schmelcher
	Prof. Dr. Ludwig Mathey
Zusammensetzung der Prüfungskommission:	Prof. Dr. Peter Schmelcher
	Prof. Dr. Ludwig Mathey
	Prof. Dr. Markus Drescher
Vorsitzender des Prüfungskommission:	Prof. Dr. Wolfgang Hansen
Datum der Disputation:	19. September 2018
Vorsitzender des Fach-Promotionsausschusses Physik:	Prof. Dr. Wolfgang Hansen
Leiter des Fachbereichs Physik:	Prof. Dr. Michael Potthoff
Dekan der Fakultät MIN:	Prof. Dr. Heinrich Graener

Zusammenfassung

In der vorliegenden Arbeit wird ein System aus zwei Coulomb-Kristallen in einem Doppeltopfpotential untersucht. Coulomb Kristalle sind stabile Gleichgewichtskonfigurationen von Ionen in einem externen Potential. Abhängig von den Potentialparametern, der Anzahl und der Art der Ionen ergeben sich unterschiedliche Kristallstrukturen. Im häufig verwendeten harmonischen Potential sind dies vorallem die lineare Kette (eindimensional), die zig-zag-Kette (zweidimensional), die Ringkonfiguration (zweidimensional) und die Anordnung der Ionen in Schalen (dreidimensional). Durch Änderung der Potentialparameter können die Strukturen ineinander übergehen.

Der Fokus in dieser Arbeit liegt auf der zig-zag Konfiguration im Doppeltopfpotential. In der Forschung wird die zig-zag Kette häufig verwendet um grundlegende Prinzipien wie z.B. die Landau Theorie [1] oder den Kibble-Zurek Mechanismus [2] zu untersuchen.

Durch eine Änderung der Position eines endständigen Ions werden Wellen in einem der Coulombkristalle erzeugt. Die entstehende Dynamik im System beider Kristalle wird am Beispiel der zig-zag Konfiguration diskutiert. Die erzeugten Wellen propagieren durch den ersten Kristall, werden an der Potentalbarriere teilweise reflektiert, aber auch durch die langreichweitige Coulomb Wechselwirkung auf den zweiten Kristall übertragen.

In der zig-zag-Konfiguration im Doppeltopf mit gleicher Anzahl von Ionen in beiden Töpfen kann durch die Senkung der Barriere eine komplexe Umordnungsdynamik beobachtet werden. In der Richtung mit hoher Fallenfrequenz erfolgt eine komplette Umordnung der Ionen, die Ordnung der Ionen in Richtung entlang der Doppeltopfanordnung bleibt jedoch in dem gewählten Parameterbereich erhalten. Die beobachtete Dynamik in den Kristallen ist nicht ausschließlich irregular. Geordnete Ionenkonfigurationen, wie Bögen, Linien oder Kreuze, wechseln mit ungeordneten Strukturen ab.

Eine ungleiche Verteilung der Ionen verursacht durch das Absenken der Barriere eine Umordnung der Ionen in den Kristallen und ermöglicht den Transfer von Ionen. Für vier verschiedene Kristallstrukturen, die lineare und die zig-zag Kette, die Ring- und die Schalenkonfiguration, wird die Abhängigkeit der Transferdynamik von der Barrierenhöhe diskutiert.

Abstract

In the present work a system of two Coulomb crystals confined in a double well potential, with a crystal in each well, is investigated. Coulomb crystals are stable equilibrium configurations of ions in an external potential. The configurations differ, depending on the potential parameters, the number and the species of ions. In the often used anisotropic harmonic potential one can observe e.g. linear chains (one dimensional), zig-zag chains (two dimensional) circle configuration (two dimensional) or ions arranged in shells (three dimensional). By changing the potential parameters the configurations merge into each other.

The main example for the discussion in this work will be the zig-zag configuration This system is often used to study basic principles such as the Landau theory [1] or Kibble-Zurek mechanism [2].

By displacing an ion at the outer end of one of the zig-zag chains, one can observe different kind of waves propagating through the crystal, which are partially reflected at the potential barrier between the wells, but are transmitted into the second crystal via the long-range Coulomb interaction as well.

In the system of two equal-sized zig-zag chains of trapped ions in a double well potential, a quench in the barrier height induces a complex pattern of non-equilibrium dynamics. For the chosen parameter regime a complete loss of spatial order in the radial direction can be observed, although the axial arrangement of the ions remains unchanged. The dynamics in the crystals, however, are not exclusively irregular. In the course of the dynamics some ions arrange in ordered structures such as bows, lines or crosses. This ordered structures alternate with disordered phases.

A quench of the barrier height in a system of Coulomb crystals with different sizes can induce additional transfers of ions over the barrier. Depending on the amplitude of the quench ions travel over the barrier. For four different crystal structures, linear chain, zig-zag chain, ring and shell configuration, the ion dynamics and the ion transfer is investigated as a function of the amplitude of the quench.

Contents

CHAPTER 1

Introduction

Since their development many decades ago [3–5], ion traps have established themselves as a powerful tool in physics with applications ranging from mass spectroscopy [6, 7] to high precision tests for quantum electrodynamics [8–10] and quantum information processing [11–13].

The development of new trapping techniques, such as optical trapping [14] and the miniaturization of ion traps by exploiting on chip technologies (micro fabrication) [15, 16] open new possibilities for controlling the ions and accessing physically interesting and yet unexplored trapping conditions. Consequently, the experimental and theoretical understanding of the behavior of ions (both single species and mixtures) in different traps have become the focus of many recent studies [17–20].

A particular example is the study of Coulomb crystals. Using several cooling techniques such as Doppler cooling [21, 22], electromagnetically induced-transparency (EIT) [23, 24] or sympathetic cooling [23] it is possible to reduce the kinetic energy of the trapped particles to the regime of micro-Kelvin where the ions self-organize to the so-called Coulomb crystals (CCs) [25]. The structures of such crystals depend on the trap parameters and range from linear chain (1D), concentric rings (2D), shells (3D) [26–28] and string-of-disks configurations [29] to two-component Coulomb bi-crystals [30]. By tuning the parameters of the trap potential, such as the amplitude of the DC and the amplitude and frequency of the AC potential (in the case of a Paul trap) or the number of ions, Coulomb crystals can undergo various transitions from one structure to another [27, 31].

Special attention has been given in the literature to the case of the second order phase transition from the linear to the zigzag chain of ions [32–34] which results in structures with [2, 35, 36] or without [37, 38] topological defects (so-called kinks). In such a way the structural transitions of trapped ions serve among others as a playground for studying fundamental processes in physics, an example being here the Kibble-Zurek mechanism

introduced originally in the field of cosmology [2].

Given the wealth of effects resulting from a trapping of ions in an ordinary Paul trap [3] it is natural to ask for the effects stemming from a more involved trapping potential. Such a potential can be provided for ions through micro-fabrication [15, 39], where for example segmentation can be added to the standard Paul trap [40, 41]. This techniques give rise to a plethora of new possibilities for trapping potentials [13] like a double well with tunable positions of minimums used for studying ion transport [42] or for splitting small ion crystals [43–46] .

In the case of the double well trapping potential, the long-range inter- and intra-well interactions among the Coulomb crystals occupying each potential well give rise to a very complex non-equilibrium dynamics.

In this work the initial states are Coulomb crystals in the double well potential. Emanating from the equilibrium state of the ions, the ion dynamics introduced by a displacement of an ion or a quench in the potential is analyzed by numerically solving the classical equation of motion. The quantum effects are neglected.

In the quantum mechanical system two mechanism could influence the dynamics of the ions. First, in the quantum regime the frequencies of the center of mass oscillation could be changed and an ion could tunnel through the barrier. In [47] the breathing mode of an ion crystal in a harmonic potential (in one and two dimensions) both in the quantum and in the classical regime was investigated. It was found, that the quantum mode amplitude decreased with the number of particles and in all considered two dimensional systems the frequency converged to its classical asymptotic interaction. The quantum effects in the one dimensional system are stronger than in the two dimensional system. This work focuses on the three dimensional dynamics, so the expected influence should be less for the system and the chosen number of particle on all frequencies. The second mechanism is the tunneling. The tunneling strength of one ion in the double well potential (one dimension) is six order of magnitudes smaller than the mean kinetic energy of an ion for the investigated perturbation regime. Hence, the probability of tunneling in the investigated perturbation regime is negligible. A further argument for the classical treatment is the melting of the crystals which is caused by the energy introduced by the quench and the large number of ions, which would destroy the quantum effects by interference.

Mainly (chaps. 5 and 6) the chosen initial configuration is a zig-zag chain in each well. The large experimental and theoretical interest in the configuration caused the deeper investigation of the zig-zag structure in this work.

The thesis starts with an introduction of the physical and technical basics in the context of the presented investigations. The crystalization of ions in an external potential

in general and the technical realizations including the trapping and cooling of the ions are discussed.

In the second chapter, the setup is introduced and the basic principles are translated to the current setup with explicit discussion about parameters and the equations of motion. The equations of motion are not analytically solvable and therefore the out of equilibrium dynamics is numerically simulated.

The preparation of the initial ion configurations and the numerical results as well as the comparison with the well known harmonic potential are treated in chapter 4. In addition a short overview over the numerical algorithm solving the equation of motion are presented.

In chapter 5, the initial configuration are two zig-zag chains trapped in the double well potential. The aim is to characterize the Coulomb coupling of the crystals by introducing a perturbation in the form of a displacement of an edge ion. The energy transfer between the two crystals is analyzed and depending on the direction of the displacement, the oscillation of the ions in the crystals is visualized. One can observe shock waves traveling through the crystals as well as collective oscillations with phase shifts and bifurcations.

The following chapter 6 treats the case of symmetric populated wells, each having the same number of ions in an initial zig-zag configuration. Lowering the barrier height by a sudden quench changes the potential energy of the crystals and results in nonlinear dynamics. The symmetry of the initial crystal configurations, the two energetically-lowest equilibrium states of the zig-zag chains, induced interesting nonlinear dynamics with alternate disordered and transient structures. In order to characterize the order of the system, the Voronoi measure, based on Voronoi diagrams [48] is introduced and it is shown that it reflected the creation and the annihilation of the structures quite well. Furthermore, the dynamics of the ions is analyzed in the basis of the eigenvectores.

In chapter 7 the study is extended to the case of an asymmetric population of the wells. This asymmetric population paves the way for an even richer dynamics inducing transfer processes of ions above the barrier. The transfer dynamics is analyzed not only for the zig-zag chains, but also for linear chains, the two dimensional circle configuration and the three dimensional spherical (shell-like) configuration. A non-smooth (step-like) dependence of the ion passage time on the height of the barrier can be observed. The transport process is analyzed for crystalline structures of different dimensionality. The Voronoi measure is used to discuss the effects of the transport on the order of the two crystals.

The possibility of realizing the setup experimentally is briefly discusses in the conclusion (chap. 8) and the main results of the work is summarized.

CHAPTER 2

Basics

In this chapter, the physical principles which underlie this work are discussed. Section 2.1 elucidates the importance in science and technology as well as explains the crystallization process and the structure of Coulomb crystals (CCs). Afterwards the mechanisms required for the investigation of the CC in the laboratory including their trapping (sec. 2.2) and their cooling (sec. 2.3) are discussed. Special emphasis is put on the RF Paul trap due to its particular importance for this work. The presentation of the basics follows the discussion in [49–51].

2.1 Coulomb crystals

Coulomb crystals (Ccs), also named Wigner crystals, are spatially ordered structures of ions. Their formation is solely based on classical electromagnetic interactions between confined charged particles of the same type of charge. Particles in an external potential build a Coulomb crystal, if they are in a stable equilibrium state. The number of particles which build a CCs varies from two particles [52] to, in principle, an infinite number of ions [53, 54]. In contrast to crystals in solid state physics, CCs need the external field to compensate for the Coulomb repulsion between the ions.

First interest in Coulomb crystals arouse in astronomy. When a star dies it can turn into a white dwarf or neutron star, which are assumed to incorporate Coulomb crystallized matter [55]. Nowadays, the applications of CCs are broad. With the help of CCs, many theories in various physical and chemical research fields such as non-linear dynamics [52, 56], cavity quantum-electro dynamics related experiments [9, 10, 57] or statistical physics [2, 36] can be evaluated. Modern technical applications of CCs are extremely precise clocks defining new time standards [58], molecular investigations of chemical interest [59], quantum simulations [60, 61] and implementations for quantum-information processors [62, 63].

CCs form up when a hot trapped plasma of charged particles is frozen out in a way that the charged particles can arrange themselves in an equilibrium configuration defined by the Coulomb interaction between them and by an external field. In order to reach the equilibrium state, the particles have to lose kinetic energy, hence, they have to cool down. This process can be characterized by the plasma coupling parameter

$$\Gamma = \frac{Q^2}{4\pi\epsilon_0 a k_b T}, \tag{2.1}$$

where ϵ_0 is the electric constant, k_B is the Boltzmann constant, Q is the charge of the particle, a the Wigner-Seitz radius corresponding to the radius of a sphere whose volume is equal to the mean volume per particle and T is the temperature of the particles. Γ can be interpreted as a measure for the ratio of the inter-particle Coulomb energy and their kinetic energy:

$$\Gamma \sim \frac{E_{Coul}}{E_{kin}}. \tag{2.2}$$

It has been proven [53, 64], that the criterion for the crystallization is given by

$$\Gamma \geq 175. \tag{2.3}$$

In order to reach such high values for Γ, one needs to control the charge, the number of the particles and the kinetic energy of the particles in the crystallization process. For a given particle number and particle species, the temperature T and thereby the kinetic energy is the only adjustable parameter. In common ion traps, the highest particle density of single charged ions which can be experementally achieved is $< 1 \times 10^{15}\,\mathrm{m}^{-3}$ [50] corresponding to a Wigner-size radius of $a \sim 10\,\mu\mathrm{m}$. This results in a temperature of

$$T \sim 10\,\mathrm{mK} \tag{2.4}$$

which is necessary to achieve Coulomb crystallization. Such low temperatures for the formation of CCs were first realized with the development of laser cooling techniques (sec. 2.3) in the late 1970s and early 1980s [65, 66].

The CCs show a rich variety of structures. The structural properties strongly depend on the number of ions, the involved species, as well as on the trapping potential Φ. Being the simplest trapping potential, the harmonic confinement with

$$\Phi(x, y, z) = \omega_x x^2 + \omega_y y^2 + \omega_z z^2 \tag{2.5}$$

plays a dominant role in the investigation of CCs. Therefore, here only the structures of CCs in an harmonic potential are introduced. Moreover, the discussion is restricted to

the single-species case. For differently designed potentials as well as mixed ion species the ions can organize in more complex equilibrium states [30, 31]. The total number of equilibrium states depends exponentially on the number of particles in the CCs. However, the most stable and most investigated structures are the lowest-energy states.

The simplest case for a CC is the one dimensional linear chain, having non-equidistant spacings which are largest near the ends of the chain and smallest in the center (fig. 2.1). This structure can be found in strongly anisotropic three dimensional trapping potentials with a much stronger confinement in radial than in axial direction ($\omega_z \ll \omega_x = \omega_y$).

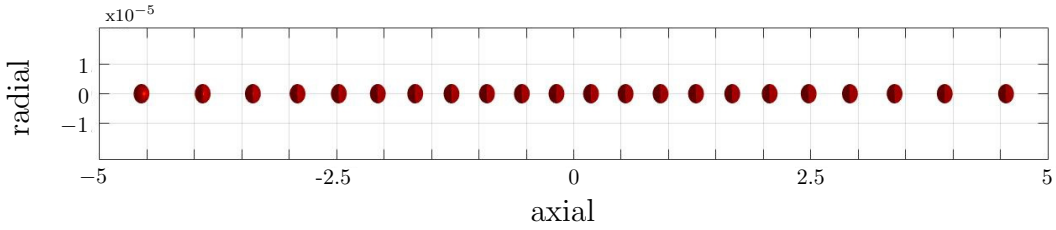

Figure 2.1: Example for a linear ion chain with 22 ions in an harmonic potential with a ratio of $\alpha = \frac{1}{8}$ from the axial to the radial confinement.

Changing the aspect ratio of the trapping frequencies in such anisotropic potentials, the charged particles can undergo a transition [36, 38, 67] from a linear to a zigzag chain without or with defects (so-called kinks). This transition is a second order phase transition, which is characterized by an abrupt change in the system when varying a parameter by a small amount. This process can be understand in terms of the Landau theory [1].

Other possible structures of CCs in two-dimensional anisotropic harmonic potentials are elliptic and concentric rings with magical numbers, and hexagonal lattices for infinite planar crystals. Furthermore, helix structures can be found in the transition from two to three dimensional traps. Finally, concentric shells arise in the isotropic harmonic potential with finite number of ions.

In this work, in particular the zigzag structure is investigated. Additionally, in chapter 7 the linear chain in one dimension, the concentric rings in two dimensions and the concentric spheres in three dimensions are chosen as initial configurations for the investigation of the ion dynamics.

2.2 Trapping of ions

The formation of Coulomb crystals (CCs) in an equilibrium state is realized in experiments by confining the charged particles within the fields of ion traps, thereby compensating for the repulsive Coulomb force between the ions. The basic concepts and techniques to construct trapping potentials are introduced in this section. Special attention is payed to the Paul trap, because it is the most suitable trap to reproduce the findings in this work.

2.2.1 Earnshaw theorem

In 1842, S. Earnshaw proved, that there does not exist a solely static magnetic or electric field which can trap a charged particle in a stable stationary equilibrium position [68]. To achieve stable trapping, a minimum at some point r_0 has to exist. Such a minimum is characterized by a vanishing first derivative of the electric potential itself: $\nabla\Phi(\mathbf{r})|_{\mathbf{r}_0} = 0$. A further necessary condition for a stable minimum in $\mathbf{r}_0$ is given by the fact, that for the eigenvalues E_i of the Hesse-matrix (the second derivative in $\Phi(\mathbf{r})|_{\mathbf{r}_0}$)

$$H(\Phi(\mathbf{r}))|_{\mathbf{r}_0} = \begin{bmatrix} \partial_x^2\Phi(\mathbf{r}) & \partial_{xy}\Phi(\mathbf{r}) & \partial_{xz}\Phi(\mathbf{r}) \\ \partial_{yx}\Phi(\mathbf{r}) & \partial_y^2\Phi(\mathbf{r}) & \partial_{yz}\Phi(\mathbf{r}) \\ \partial_{zx}\Phi(\mathbf{r}) & \partial_{zy}\Phi(\mathbf{r}) & \partial_z^2\Phi(\mathbf{r}) \end{bmatrix}_{\mathbf{r}=\mathbf{r}_0} , \tag{2.6}$$

the condition $E_i \geq 0$ for all i has to hold. In the case of all eigenvalues E_i being zero, the point r_0 is a saddle point. Assuming in the next step a charge free space also the Maxwell equation

$$\Delta\Phi(\mathbf{r}) = \nabla \cdot \mathbf{E} = 0 \tag{2.7}$$

holds. Exploiting $\Delta\Phi = Spur(H|_{r_0}) = \sum_i E_i$, the latter can only be fulfilled with all $E_i = 0$ or by an indefinite Hesse-matrix (the matrix has positive and negative eigenvalues). Hence, there can be no minimum in $\mathbf{r}_0$ for a static electric field.

To resolve this issue, time-dependent fields, such as in optical traps (sec. 2.2.2) or any other additional field can be applied. In the case of the Penning trap (sec. 2.2.3) an additional magnetic field is used while for the Paul trap (sec. 2.2.4) a radio frequency electric (RF) field is added.

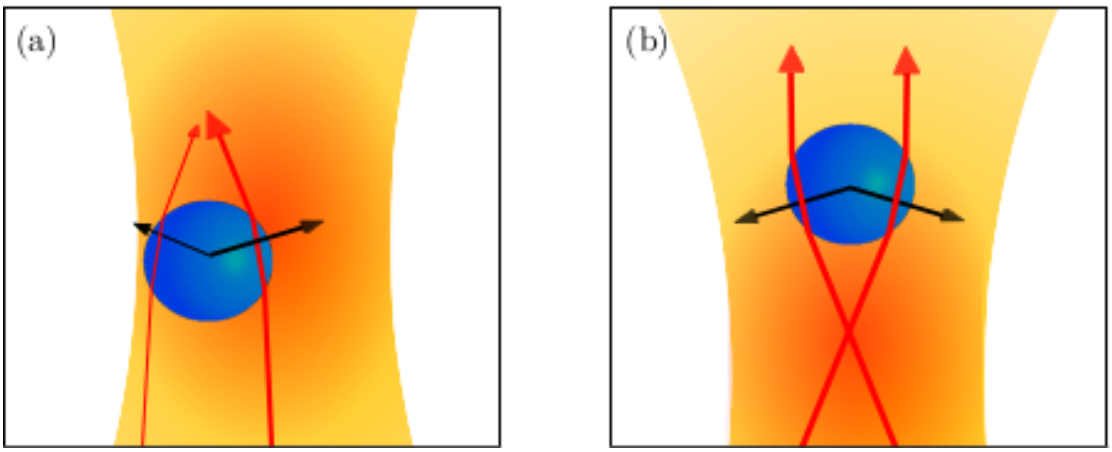

Figure 2.2: Qualitative scheme of the radiation pressure on a particle in the focus of a laser beam based on the ray-optics approximation [71]. The direction of the ray is depicted as red arrows. The forces (black arrows) on a transparent particle (blue) in a focused laser beam is shown (a) if the particle is transversal displaced to the focus (b) and if the particle is longitudinal displaced to the focus of the laser. The net forces trap the particle in the focus.

2.2.2 Optical traps

The concept of an optical dipole trap bases upon the time-dependent electromagnetic field of light. In 1970, Arthur Ashkin demonstrated theoretically and experimentally that one can trap and accelerate a micron-sized particle in a focused laser beam [69, 70] leading to the development of the first optical dipole trap for an ion in 2010 [14]. Through the strong focusing of the laser beam the particle is trapped by the dipole force and the radiation pressure of the beam [71, 72].

The optical force in the trap has two components, the scattering force, in the direction of light propagation, and the gradient force, in the direction of the spatial field gradient. The theoretical treatment separates two regimes depending on the particle size. The principle of optical trapping of particles with sizes much larger than the wavelength of the trapping laser, i.e., the radius $a \gg \lambda$, can be understood by the ray optics approximation: First the surface reflection is neglected. Second if a particle moves out to one side out of the laser beam focus, it deflects the laser beam and, hence, increases the momentum of the photons to the same side. Due to the conservation of momentum, the particle will be pushed back to the laser beam focus (compare fig. 2.2). Thus, the laser forms a stable three dimensional optical trap. Finally, considering a particle with a reflecting surface, the reflected photons push the particle away from the focus. In summary, there are two competing processes. To maximize the restoring force, it is necessary to strongly focus the laser beam and to choose a suitable medium.

A particle which is much smaller than the wavelength of the laser, (radius $a \ll \lambda$)

can be approximated as a dipole and the optical force can be calculated with the help of the Rayleigh approximation. For the scattering force one obtains for a particle with radius a [71]:

$$|F_{scatt}| = \frac{I_0 \sigma n_m}{c} \tag{2.8}$$

$$\text{with} \qquad \sigma = \frac{128\pi^5 a^6}{3\lambda^4}\left(\frac{m^2-1}{m^2+1}\right)^2 \tag{2.9}$$

$$\text{and} \qquad m = \frac{n_p}{n_m}.$$

In this formula, the scattering cross section σ is a function of the radius a, the refraction n_p of the particle and the refraction n_m of the medium as well as of the wavelength λ of the laser. I_0 is the intensity of the laser beam and c the speed of light. This scattering force pushes the particle out of the focus. The gradient force arises from the interaction of the inhomogeneous electric field $\mathbf{E}(\mathbf{r},t)$ of the laser and the induced dipole $\mathbf{p}(\mathbf{r})$ [71]:

$$\mathbf{F}_{grad} = [\mathbf{p}(\mathbf{r},t)\cdot\nabla]\mathbf{E}(\mathbf{r},t) = \frac{2\pi n_m^2 a^3}{c}\left(\frac{m^2-1}{m^2+1}\right)\nabla I_0. \tag{2.10}$$

$\mathbf{F}_{grad}$ tends to push the particle towards the laser beam and moves it to the focus where the light intensity is highest. It is proportional to the laser intensity and forms a trapping potential of the form:

$$V(\mathbf{r}) = -\frac{2\pi n_m a^3}{c}\left(\frac{m^2-1}{m^2+1}\right) I(\mathbf{r}). \tag{2.11}$$

In practice, optical traps have a relatively weak optical potential depth ($\approx 1\times10^{-3}\,\mathrm{K}$) [14].

2.2.3 Penning traps

The working principle of the Penning trap bases on combining a static electric and a magnetic field to confine the charged particles. Typically, a Penning trap is build out of three electrodes, a ring electrode and two end caps. The trapping potential is a superposition of a homogeneous magnetic field $\mathbf{B} = (0,0,B_0)$ and an electric field $\mathbf{E} = -\nabla\Phi$ with

$$\Phi = \frac{U_0}{2d^2}(2z^2 - x^2 - y^2). \tag{2.12}$$

Here, d is a geometrical factor of the trap and U_0 is the applied voltage between the end caps and ring electrode.

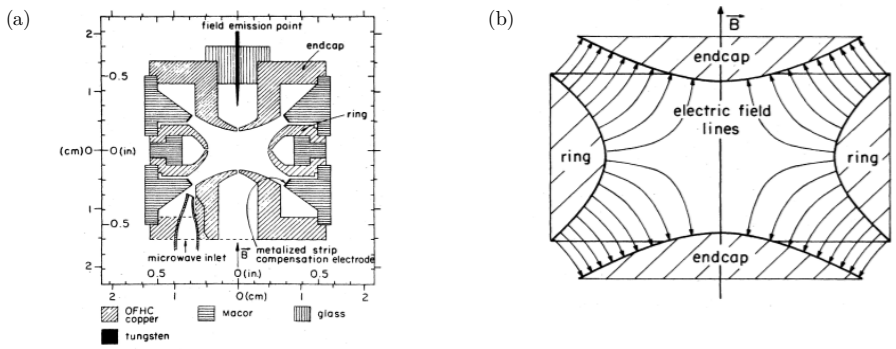

Figure 2.3: (a) Scale drawing of an experimental Penning trap [73] and (b) electric and magnetic field configuration of a penning trap [74].

Caused by the Lorentz force

$$\mathbf{F}_L = -q\mathbf{E} + q(\mathbf{v} \times \mathbf{B}) \tag{2.13}$$

a particle with charge Q, mass M and the velocity $\mathbf{v}$ in a Penning trap obeys the following equations of motion:

$$\begin{aligned} \frac{d^2x}{dt^2} &= \frac{1}{2}\omega_z^2 x + \omega_0 \frac{dy}{dt} \\ \frac{d^2y}{dt^2} &= \frac{1}{2}\omega_z^2 y - \omega_0 \frac{dx}{dt} \\ \frac{d^2z}{dt^2} &= -\omega_z^2 z. \end{aligned} \tag{2.14}$$

In radial direction, the charged particle follows a circular path with the cyclotron frequency $\omega_0 = \frac{|QB_0|}{M}$ caused by the magnetic field, while in axial direction the particle is confined in a simple harmonic oscillation with the axial frequency $\omega_z = \sqrt{\frac{2QU_0}{Md^2}}$ (fig. 2.3).

One observes that the radial and the axial motion are decoupled. Hence, the radial equation of motion can be rewritten as

$$\frac{d^2u}{dt^2} = \frac{1}{2}\omega_z^2 u - i\omega_0 \frac{du}{dt}, \tag{2.15}$$

with the substitution $u = x + iy$. Using the general ansatz $u = \exp(-i\omega t)$ this results in

$$\omega - \omega_0 \omega + \frac{1}{2}\omega_z^2 = 0. \tag{2.16}$$

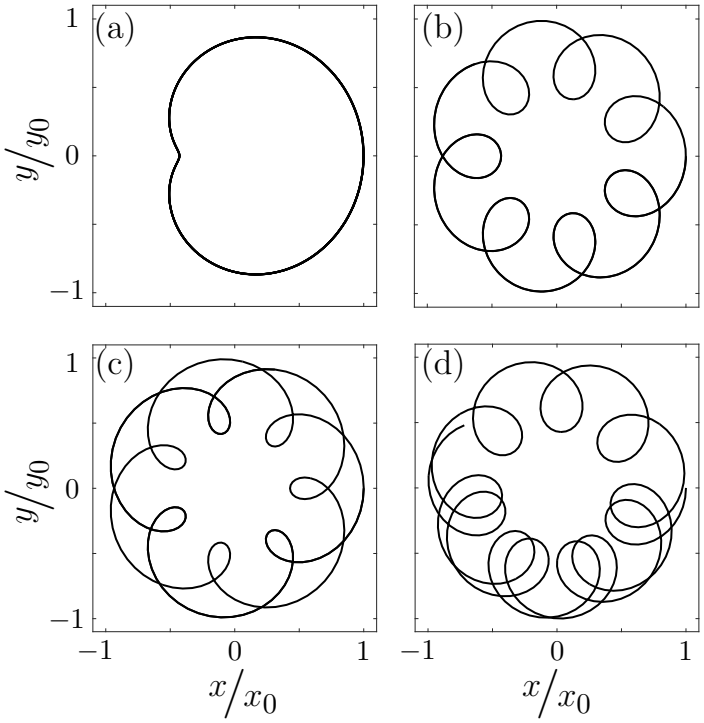

Figure 2.4: Examples for the radial trajectories in an ideal Penning trap with $R_- = 2.5R_+$ for periodic orbits (a) $\omega_+ = 2\,\omega_-$ (b) $\omega_+ = 8\,\omega_-$ (c) $\omega_+ = \frac{9}{2}\,\omega_-$ and for a quasi-periodic orbit (d) $\omega_+ = 2\sqrt{17}\,\omega_-$ with the initial coordinates (x_0, y_0) [49].

A stable confinement of the charged particle will therefore be achieved when the conditions

$$\frac{|Q|}{M} B_0^2 > \frac{4|U_0|}{d^2} \quad \text{and} \quad QU_0^2 > 0 \tag{2.17}$$

are fulfilled. In this case, the trajectories for the particle are given by

$$\begin{aligned} x =& R_+ \cos(\omega_+ t + \phi_+) + R_- \cos(\omega_- t + \phi_-) \\ y =& \frac{Q}{|Q|} \left[R_+ \sin(\omega_+ t + \phi_+) + R_- \sin(\omega_- t + \phi_-) \right] \\ z =& R_z \cos(\omega_z t + \phi_z), \end{aligned} \tag{2.18}$$

with the modified cyclotron frequency $\omega_+ = \frac{1}{2}(\omega_c + \sqrt{\omega_c^2 - 2\omega_z^2})$ and the magnetron frequency $\omega_- = \frac{1}{2}(\omega_c - \sqrt{\omega_c^2 - 2\omega_z^2})$. The cyclotron radius R_+, the magnetron radius R_-, the axial amplitude R_z and phases ϕ_+, ϕ_-, ϕ_z are defined by the initial conditions. In the radial (x,y)- plane, the motion of a charged particle can described as an epitrochoid. Some examples for this motion are shown in figure 2.4.

2.2.4 Radio-frequency traps

The solution of the Laplace equation of a static electric field allows no stable trapping but can result in a saddle point in the potential (sec. 2.2.1). In order to trap charged particles an additional radio frequency field (RF) to such a saddle point can be added, thereby rotating it. The Paul trap consists of an electrostatic field Φ_{stat} and an additional time-dependent electric field Φ_{rf} that varies sinusoidally with the frequency ω_{rf}. For simplification, the potentials are here assumed to be harmonic:

$$\begin{aligned}\Phi(x,y,z,t) &= \Phi_{\text{stat}}(x,y,z) + \Phi_{\text{rf}}(x,y,z,t) \\ &= \frac{1}{2}U_0(c_x x^2 + c_y y^2 + c_z z^2) + \frac{1}{2}U_{\text{rf}}\cos(\omega_{\text{rf}}t)(d_x x^2 + d_y y^2 + d_z z^2), \quad (2.19)\end{aligned}$$

where U_0 is the voltage of the static potential and U_{rf} is the voltage of the RF potential. The c_i and d_i are geometrical parameters which depend on the design of the trap. As discussed in section 2.2.1 the Maxwell equation (eq. 2.2.1) has to be fulfilled, which restricts the geometrical parameters to

$$\begin{aligned} c_x + c_y + c_z &= 0 \quad (2.20)\\ d_x + d_y + d_z &= 0. \end{aligned}$$

There are different possibilities to fulfill these conditions. For a three dimensional confinement, the geometrical parameters can be chosen as:

$$c_x = c_y = c_z, \qquad d_x + d_y = -d_z. \quad (2.21)$$

For a dynamical confinement in the (x,y)-plane with an axial static restriction, the so-called linear trap [75], the parameters have to be chosen as:

$$-(c_x + c_y) = c_z, \qquad d_x = -d_y. \quad (2.22)$$

Equations of motion and Mathieu equation

The classical equations of motion for a particle with charge Q and the mass M in a RF Paul trap defined by the potential $\Phi(x, y, z, t)$ (see eq. 2.2.4) are given by

$$\begin{aligned}
\ddot{x} &= -\frac{Q}{M}\Big(U_0 c_x + U_{\mathrm{rf}} d_x \cos(\omega_{\mathrm{rf}} t)\Big)x, \\
\ddot{y} &= -\frac{Q}{M}\Big(U_0 c_y + U_{\mathrm{rf}} d_y \cos(\omega_{\mathrm{rf}} t)\Big)y, \\
\ddot{z} &= -\frac{Q}{M}\Big(U_0 c_z + U_{\mathrm{rf}} d_z \cos(\omega_{\mathrm{rf}} t)\Big)z.
\end{aligned} \tag{2.23}$$

These non-coupled equations can be transformed to the Mathieu differential equations [76] by introducing the following variables:

$$\tau = \frac{\omega_{\mathrm{rf}} t}{2}, \qquad a_u = \frac{4QU_0 c_u}{M\omega_{\mathrm{rf}}^2}, \qquad q_u = -\frac{2QU_{\mathrm{rf}} d_u}{M\omega_{\mathrm{rf}}^2}, \tag{2.24}$$

where u represent either x, y or z. This leads to the standard form of the Mathieu equation:

$$\frac{d^2u}{d\tau^2} + (a_u - 2q_u \cos(2\tau))u = 0. \tag{2.25}$$

From the Floquet theorem [76, 77] the solution of this equation can be obtained as

$$u(\tau) = A_u e^{\mu_u \tau} \sum_{n=-\infty}^{\infty} C_{2n,u} e^{i2n\tau} + B_u e^{-\mu_u \tau} \sum_{n=-\infty}^{\infty} C_{2n,u} e^{-i2n\tau} \tag{2.26}$$

The characteristic exponent μ_u, and C_{2n} are functions of a_u while and A_u and B_u depend on the initial conditions. The stability of the solution is determined solely by the exponent μ_u. If the real part of the characteristic exponent μ_u is non-zero, the amplitude grows exponentially in time, such that the solution is not stable and the particle trajectory is not bound. The condition for stable trapping is $\mu_u = i\beta_u$. Inserting the general solution (eq. 2.26) into the Matthieu equation (eq. 2.25) one ends up with the relation between the parameters β_u, a_u and q_u:

$$\beta_u^2 = a_u - q_u\Big(\frac{1}{D_2 - \frac{1}{D_4 - \frac{1}{\dots}}} + \frac{1}{D_{-2} - \frac{1}{D_{-4} - \frac{1}{\dots}}}\Big) \tag{2.27}$$

with $D_{2n} = \frac{\left[a_u - (2n+\beta_u)^2\right]}{q_u}$. Moreover, for the coefficients C_{2n} one obtains the recursive formula:

$$\frac{C_{2n,u}}{C_{2n\pm,u}} = -\frac{q_u}{(2n+\beta_u)^2 - a_u - \frac{q^2}{(2n\pm2+\beta_u)^2 - a_u - \dots}} \tag{2.28}$$

The pairs of a_u and q_u which satisfy the condition $0 \leq \beta_u \leq 1$ [3] result in stable solutions. The parameters for stable and instable solutions can be depicted in a stability diagram in the (a_u, q_u)-plane (fig. 2.5). The boundaries of the stability regions fulfill the conditions $\beta_u = 1$ or $\beta_u = 0$.

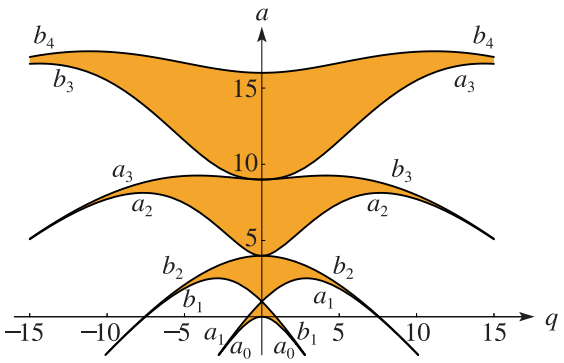

Figure 2.5: Stability diagram in the (a_u, q_u)-plane [77]. In the orange regions the pair of parameters (a_u, q_u) allows the stable trapping of ions.

Effective potential and potential depth

In order to trap a charged particle in the RF Paul trap the trapping frequency has to be of the order of MHz. Typically, experimental parameters for the rf potential are $\frac{\omega_{\mathrm{rf}}}{2\pi} \sim$(4 to 50) MHz and $U_{\mathrm{rf}} \sim$(8 to 350) V. This fast rotating voltage results in a time-averaged an effective potential Φ_{av} with a potential depth $D(\mathbf{r})$. The calculation of the effective potential follows [49]. The first assumption is, that the motion of the particle in the trap potential (eq. 2.2.4) is influenced by an electric field $\mathbf{E} = -\nabla\Phi$ with a static $\mathbf{E}_0(\mathbf{r})$ and a high frequency component $\mathbf{E}_\omega(\mathbf{r}, t)$ while $\mathbf{r} = (x, y, z)$. Under the assumption that the oscillation of the particle by the action of $E_\omega(r, t)$ is small, the trajectory of the particle can be written as

$$\mathbf{r}(t) = \mathbf{R}(t) + \chi(t). \tag{2.29}$$

Here, $\chi(t)$ is a fast oscillatory motion of the particle evoked by the frequency ω, while $\mathbf{R}(t)$ represents the average of $\mathbf{r}(t)$ over a period of the field $\mathbf{E}_\omega(\mathbf{r}, t)$. The amplitude of $\chi(t)$ is assumed to be small and, hence, the equation of motion can be expanded in powers of $\chi(t)$, taking only the first order terms are taken into account. This results in

$$\frac{d^2\mathbf{R}(t)}{dt^2} + \frac{d^2\chi(t)}{dt^2} = \frac{Q}{M}\left[\mathbf{E}_0(\mathbf{r}) + \chi(t)\frac{d\mathbf{E}_0(\mathbf{r})}{d\mathbf{r}(t)} + \mathbf{E}_\omega(\mathbf{R}, t)\cos(\omega t) + \chi(t)\frac{d\mathbf{E}_\omega(\mathbf{R})}{d\mathbf{R}(t)}\cos(\omega t)\right] \tag{2.30}$$

and leads for $\chi(t)$ to the differential equation

$$\frac{d^2\chi(t)}{dt^2} = \frac{Q}{M}\mathbf{E}_\omega(\mathbf{R},t)\cos(\omega t) \tag{2.31}$$

and the solution

$$\chi(t) = -\frac{Q}{M}\frac{E_\omega(\mathbf{R},t)}{\omega^2}\cos(\omega t). \tag{2.32}$$

Inserting this result into the equation of motion (eq. 2.30) and averaging over the oscillation period of the field $\mathbf{E}_\omega(\mathbf{r},t)$, one gets:

$$\frac{d^2\mathbf{R}(t)}{dt^2} = \frac{Q}{M}\mathbf{E}_0(\mathbf{r}) - \frac{Q^2}{M^2\omega^2}\left\langle \mathbf{E}_\omega(\mathbf{r},t)\frac{d\mathbf{E}_\omega(\mathbf{r},t)}{d\mathbf{R}}\cos^2(\omega t)\right\rangle. \tag{2.33}$$

With the identity $(\mathbf{E}_\omega\cdot\nabla)\mathbf{E}_\omega = \frac{1}{2}\nabla\mathbf{E}_\omega^2$ and calculation of the average, the effective potential reads

$$\begin{aligned}\Phi_{\mathrm{av}}(x,y,z,t) =& \Phi_{\mathrm{stat}}(x,y,z) + \frac{Q}{4M\omega^2}E_\omega^2(x,y,z,t)\\ =& \frac{1}{2}U_0(c_x x^2 + c_y y^2 + c_z^2) + \frac{Q}{4M\omega^2}U_{\mathrm{rf}}^2(d_x x^2 + d_y y^2 + d_z z^2).\end{aligned} \tag{2.34}$$

Considering the total energy in the effective potential Φ_{av}:

$$\begin{aligned}W =& W_{kin}(R) + Q\Phi_{\mathrm{av}}\\ =& \frac{1}{2}M\dot{R}^2 + Q\Phi_{\mathrm{stat}} + \frac{Q^2}{4M\omega^2}E_\omega^2\end{aligned} \tag{2.35}$$

and the time average over the kinetic energy of the fast oscillatory motion, called micro-motion:

$$\left\langle \frac{1}{2}M\dot{\chi}^2\right\rangle = \frac{Q^2}{4M\omega^2}E_\omega^2(R,t) \tag{2.36}$$

one might assume to the intuition, that the effective potential energy of the RF field is stored as kinetic energy in the fast oscillatory motion. Therefore, motion through an inhomogeneous field leads to a permanent exchange between the kinetic energies of the secular and the oscillatory motion and the electrostatic potential energy.

The depth of the effective potential without a static electric field ($U_{\mathrm{dc}} = 0$) is [49]:

$$D(r) = \frac{qU_{\mathrm{rf}}^2}{4Md_i^2\omega^2}, \qquad (i = x,y,z). \tag{2.37}$$

Micro-motion

In the last subsection it was shown, that the dynamics in the Paul trap is given by a superposition of the secular motion following the effective potential (eq. 2.34) and a micro-motion induced by the RF voltage. Following [78] the equation of motion can be approximated to the lowest order in q and a (eq. 2.24) for $|a| \ll 1$ and $|q| \ll 1$ yielding

$$u(t) = (u_0 \cos(\omega_{sec} t))(1 + \frac{q}{2} \cos \omega_{\mathrm{rf}} t), \tag{2.38}$$

with $\omega_{sec} = \frac{\omega_{\mathrm{rf}}}{2}\sqrt{a + \frac{q^2}{2}}$. The ion oscillates with ω_{sec} in the harmonic potential (eq. 2.34) superposed by the micro-motion.

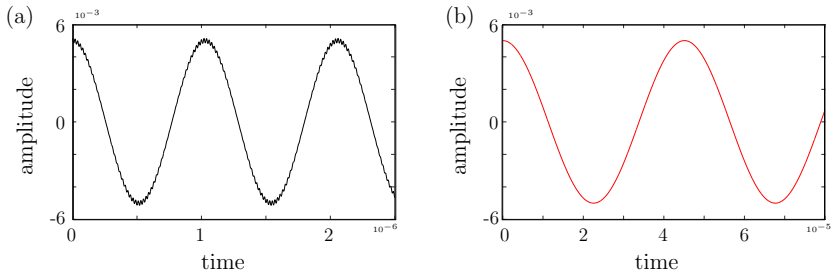

Figure 2.6: Dynamics for a trapped ion for the parameters (a) $q = 0.055$ and $a = 8 \cdot 10^{-7}$ (b) $q = 0.0049$ and $a = 7.8127 \cdot 10^{-5}$. The oscillation with the large amplitude is the secular motion and the small amplitude corresponds to the micro-motion.

In figure 2.6 the dynamics of a trapped ion in an harmonic potential for different parameters a and q are shown. Obviously, the secular motion dominates the dynamics and the micro-motion is just a small beating on the larger amplitude.

In contrast, in a CC the ions oscillate with a small amplitude around their equilibrium positions because of the finite temperature. In this regime the micro-motion is able to influence the system and with this the equilibrium position of the ions and the eigenvalues and the eigenfrequencies are affected by the micro-motion. This effects are subject of experimental and theoretical studies.

In [79] the results of the standard pseudo (effective) potential theory are compared with the experimental investigations for an planar CC. Their results show that the positions of the ions and the location of structural transitions between different crystal configurations are accurately by the use of the effective potential used in this setup (see fig. 2.7). The determination of the eigenfrequencies of the two dimensional ion crystals with the pseudo potential theory is insufficient showing significant deviations from the experimental data obtained from resolved sideband spectroscopy [79]. The accuracy depends on the value q_u (eq. 2.24).

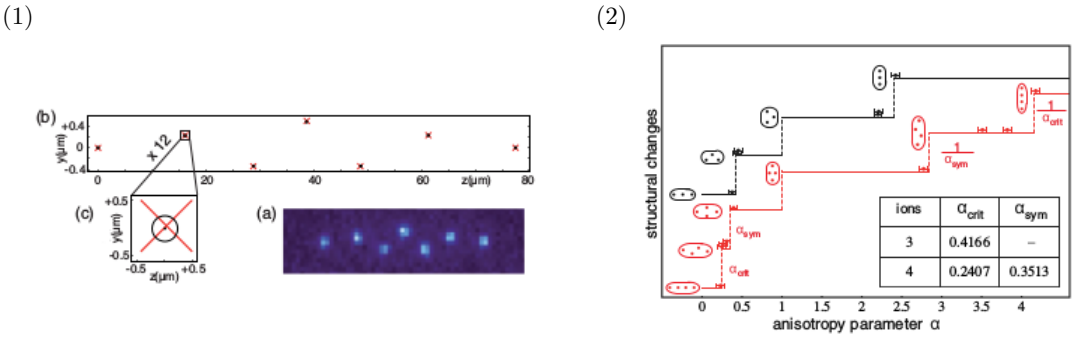

Figure 2.7: (1) Determination of ion positions in planar crystals: (a) The ion fluorescence near 397 nm is imaged on a CCD chip. (b) The ion positions (black dots) are determined by averaging over 100 exposures and compared with the result of a numerical simulation assuming Coulomb repulsion in a harmonic trap pseudo potential (red crosses). The experimental data allow for a precision of 50 nm as indicated by the circle for a 1σ standard deviation. (2) Phase transitions for a three-ion (black) and a four-ion (red) crystal. Theoretical (PPT) critical α's are indicated by vertical dashed lines with the corresponding crystal configurations. Experimental data are plotted at those α where a certain configuration is observed, with an error of 0.05 in α. For an ion crystal with an even number of ions (here, $N = 4$), α_{sym} is the relevant parameter, where the structure symmetry changes. The measurements are taken in a linear micro trap with $\Omega = 2\pi{\cdot}22.7\,\mathrm{MHz}$, $U_{\mathrm{rf}} \approx 300\,\mathrm{V}_{pp}$ yielding frequencies $\omega_y = 0.421\,\mathrm{MHz}$, $\omega_z = 0.626\,\mathrm{MHz}$, and a much larger ω_x. Inset: Table of calculated critical α [79]

Furthermore, the micro-motion influences atomic transition line shapes, second order Doppler shifts, induces Stark shifts [80] and chaos in the dynamics [81]. The most imported fact is the heating of the crystal via the micro-motion [82, 83] and its influence on the laser cooling [84]. The heating is produced by the interaction of the fast oscillating ions and electromagnetic stray fields in the trap. There are some techniques presented in [78] to minimize the micro-motion. The influence of the micro-motion scales with the distance of the ions from the minimum of the trap potential. In a linear trap, ions in the linear chain configuration are slightly affected by the micro-motion.

2.2.5 Comparison of available trap designs

In order to decide which trap design is suited to realize the topics discussed in this work, here, the advantages and disadvantages of the different trapping techniques are presented.

The main advantage of an optical trap (sec. 2.2.2) is the idealized harmonic motion of an ion in the trapping potential. However, it has a weak potential depth such that the Coulomb force between ions can lead to the escape of ions. In [14] the trapping of a single ion with the help of an optical trap was presented.

The potentials in the Penning trap (sec. 2.2.3) are time independent. Therefore, there is no micro-motion and hence, no heating occurs. The motion of the ions consists of

a cyclotron and a magnetron oscillation, which results in a complex trajectory of the ions (fig. 2.4). Moreover, a Penning trap can be larger, thereby for fixed trap depth compared to alternative trap designs. So the distance of the charged particles to the electrodes is larger reducing the interaction with the electrode surfaces and with this the heating.

The Paul trap potential (sec. 2.2.4) is time dependent. The particle trajectories are more complex than in the optical trap. Additionally the micro-motion can result in a heating process in the presence of stray fields in the electrodes of the trap [83]. The micro-motion is a fast and small oscillation such that in a first approximation the micro-motion is negligible leading to an approximately harmonic motion.

In the Penning as well in the Paul trap, CCs can be trapped [65, 66, 85]. In the last decades, the Paul trap has experienced a lot progress in the development of its design. The traps were miniaturized and the electrodes became segmented. This miniaturization and segmentation allowed an enrichment in the trapping potential forms. Multiple wells were created and the transport of ions [42] as well as splitting of CCs [43–46] was demonstrated. These developments in the design, the possible large potential depth and the minor role of the micro-motion qualifies the RF Paul trap for the experimental confirmation of the results in this work.

2.3 Cooling techniques

For many applications and experiments, it is necessary that the kinetic energy and with this the temperature of the trapped ions is small, especially for the crystallization processes (temperatures below 10 mK). Unfortunately, the production of the ions, the loading of the trap and the interaction with electric fields, in the case of the Paul trap with the RF field, can result in heating. Hence, cooling procedures have to be employed to reach low temperatures. In the following, schemes of the different cooling techniques are presented in a short overview.

One of the first cooling procedures for trapped ions has been the buffer gas cooling [49]. Here, a lighter inert gas, mostly helium, at room temperature or below is introduced in the system. The ions collide with the gas atoms, which results in an energy and momentum transfer thermalizing the ion temperature to that of the gas. However, this simple method has its limitations: (i) it works well only for massive ions, (ii) it may perturb the internal energy levels, causing frequency shifts and (iii) it broadens the spectral lines and the motional resonances.

Another way to reduce the kinetic energy of the ions is the resistive cooling [86]. Here, the ion motion in the trap induces a current in the electrodes of the trap. The induced

current reduces the kinetic energy of the ions. In Paul traps using this technique only the secular motion can be cooled, but not the micro-motion, thus this kind of cooling is not efficient.

The stochastic cooling [87] uses the fact, that there are stochastic fluctuations in the ensemble average of the positions in a finite number of interacting particles. This method is divided in three parts, (i) the measuring of the mean positions of the particles, (ii) the generation of a field pulse, which kicks the particles along the beam direction and (iii) the particles interact until they reach a new equilibrium state.

With all these different cooling techniques, it was not possible to reach the temperature regime where the crystallization process of ions takes place. Only with the advent of lasers [88, 89] the investigations of CCs started [90, 91].

2.3.1 Laser cooling

The idea of laser cooling is to reduce the kinetic energy of a trapped ion by driving one of its electronic transition by a near resonant laser. In the process of absorption and emission of photons, the total energy and the momentum of the ion and the field is conserved. The cooling of the ions is possible by choosing convenient excitation conditions. Here, the main concepts of the different laser colling techniques are presented. An explicit discussion of cooling techniques can be found in [92] and references therein. For the cooling, two processes are used, (i) the recoil dynamic (fig. 2.8) and (ii) the difference in the frequencies of the absorbed and the emitted photon. In the following, the so-called Doppler cooling, based on the recoil dynamic and the Doppler effect, is discussed. This is followed by a short presentation of further cooling techniques exploiting the energetic difference of the absorbed and emitted photon.

The Doppler cooling of ions is based on the reduction of the kinetic energy of the particle by the interaction with photons. An ion can absorb a photon of a suitable frequency and, obeying momentum conservation, it encounters a recoil in direction of the initial photon momentum. This results in a change of the ion velocity. Subsequently, the ion emits spontaneously a fluorescence photon in a random direction. Again, obeying momentum conservation, the ion velocity in opposite direction of the photon emission direction increases. For Doppler cooling this recoil dynamics are employed by a laser system. To reduce the kinetic energy of an ion in one direction (p_i) only photons counter propagating to this direction are supposed to be absorbed. Hence, the laser frequency (ω_l) has to be chosen in the way, that only ions with a given momentum p_i can absorb a photon. The laser system is red detuned to the electronic transition of the ion (ω_{ion})

$$\omega_l = \omega_{ion} - \Delta\omega \tag{2.39}$$

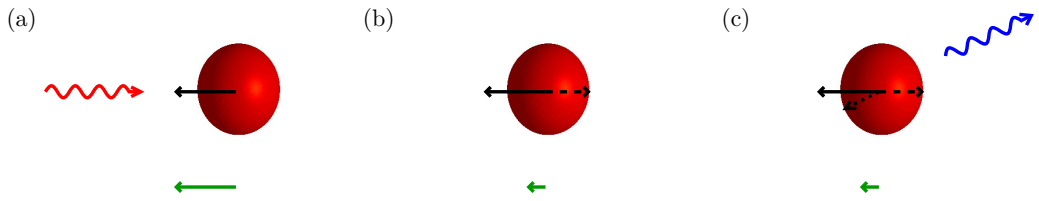

Figure 2.8: (a) The red-shifted laser photon (red waved line) can be absorbed only by an ion (red sphere) with a suited impulse component (black arrow) in opposite direction to the beam defined by the Doppler effect. (b) The absorption of a photon results in a recoil (black dashed arrow). (c) By spontaneous emission of a photon (blue waved line) in a random direction the ion gets an additional recoil. The average of recoil momentum over a large number of emissions is zero. This results in a net decrease of the momentum in the opposite direction to the laser beam. The momentum average of the ion is shown below the sketches as a green arrow.

with $\Delta\omega$ being the detuning frequency of the laser beam. By the Doppler effect, the photons can be absorbed only by ions moving in opposite direction to the laser beam (fig. 2.8 (a)). The spontaneous emission of the photon happens in a random direction and with this the ion momentum in the opposite direction increases (fig. 2.8 (c)). The average of the recoil momentum over a large number of N spontaneous emissions is zero, caused by the isotropic distribution of the momentum direction of the spontaneously emitted photons. With the directed absorption and the undirected emission of photons, the ions are decelerated in the opposite direction of the laser beam.

For the Doppler cooling, dipole transitions with a broad natural line width γ are used, in order to to cool down ions with a broad velocity distribution. One finds that the lower limit of the temperature of the ions after cooling is given by

$$T_{Doppler} = \frac{\hbar\gamma}{2k_B} \tag{2.40}$$

with k_B the Boltzmann's constant and $\hbar$ the reduced Planck's constant [50]. For an efficient cooling in all directions, a system of three orthogonal laser beams is needed.

Beyond the Doppler cooling other cooling techniques are established such as the resolved sideband cooling [21, 84, 93] or the electromagnetic-induced transparency (EIT) [23, 24, 94]. These techniques are based on the energy difference between the absorbed and the emitted photon related to the vibrational states of tightly bounded ions.

CHAPTER 3

Setup

3.1 The potential confining the Coulomb Crystals

The interest in Coulomb crystals (CCs) and their properties has grown in the last years [56, 57, 62]. Their applications range from quantum simulators for solids [60, 61] to technical utilization like extremely precise clocks [58]. So far, most of the studies have only published on single CCs [17, 18, 52, 56], altough the Coulomb force generally allows for long range interactions between different crystals as well. With the advent of segmented traps [40, 41] it has become possible to construct potentials with more than one well and to manipulate their parameters. Hence, multiple crystals can be trapped, moved, combined or split [43–46].

The simplest case of such trapping potentials is the double well potential with two identically wells, separated by a barrier, in axial direction combined with a potential of a linear Paul trap in the radial direction. The position of the wells, the height of the barrier, and the trap frequencies can be tuned.

In this work, the dynamics of two Coulomb crystals confined by a linear quadrupole Paul trap in the radial direction (x, y) and by a double well potential[1] (segmented trap) along the axial direction z are studied.

The ions are treated as classical point particles with mass m and charge Q that follow the radially confining potential $V(x, y)$ in the (x, y)-plane:

$$V(x, y, t) = \frac{U_{\mathrm{dc}}}{2}(c_x x^2 + c_y y^2) + \frac{U_{\mathrm{rf}}}{2}\cos(\omega_{\mathrm{rf}} t)(d_x x^2 + d_y y^2). \tag{3.1}$$

[1] The combination of the linear quadrupole trap potential and a double well potential is not allowed by the Laplace equation. Therefore, to fulfill the Laplace equation it is necessary to compensate the DC potential part of the trap in the radial direction by a complex form. In recent experiments with segmented Paul traps (e.g. [95, 96]) this combination was realized, giving rise to a potential similar to the one, which is chosen here or to a Mexican hat like potential.

U_{dc} and U_{rf} are the applied constant (DC) and radio frequency (RF) voltages, while ω_{rf} denotes the (radio) frequency. The parameters c_i and d_i specify the geometry of the trap. For the chosen linear trap geometry it follows $d = d_x = -d_y$ (compare sec. 2.2.4). For simplicity $c_x = c_y = c$ is chosen.

The ion dynamics in such a potential is composed of a fast motion, so-called micro-motion, and a comparatively slow average motion (the secular motion) governed by a time averaged (thus effective) harmonic potential [51]

$$V_{\mathrm{av}}(x, y) = \frac{m}{2}(\omega_x^2 x^2 + \omega_y^2 y^2). \tag{3.2}$$

Here, $\omega_x = \frac{\omega_{\mathrm{rf}}}{2}\sqrt{a - q^2/2}$ and $\omega_y = \frac{\omega_{\mathrm{rf}}}{2}\sqrt{a + q^2/2}$ are the effective trapping frequencies with dimensionless parameters $a = \frac{4QU_{\mathrm{dc}}}{m\omega_{\mathrm{rf}}^2}c$ and $q = \frac{2QU_{\mathrm{rf}}}{m\omega_{\mathrm{rf}}^2}d$ (compare sec. 2.2.4).

The influence of the micro-motion on CCs is discussed in section 2.2.4. The micro-motion depends strongly on the value of q (eq. 2.24) which can be optimized such [78, 80], that the oscillations of the ion caused by the micro-motion are very small compared with the secular motion (compare fig. 2.6). When investigating long time dynamics of the ions, exact trajectories of single ions including the micro-motion can be neglected for the averaged system dynamics. Furthermore, as mentioned in subsection 2.2.4, micro-motion heats the system which is compensated in experiments by laser cooling. For the sake of simplicity the micro-motion and the damping by the laser cooling process will be neglected in the following. Equation 3.2 is used for calculations of the crystal configurations and the simulation of the dynamics. In order to take into account the change by the RF field in the crystal configuration and the effect of finite (low) temperature, a small random initial velocity to the ions is added, leading to small oscillations around their equilibrium positions.

The double well potential in the axial direction should have a simple (differentiable) analytic form and the profiles of each well should be as close as possible to the chosen well potential $W(z)$ [2]. Furthermore, the barrier height should be easy to adjust. Following [97] one can construct a superposition of the potential $W(z)$ at the positions $\pm z_0$ such that the original potentials are connected to each other:

$$\begin{bmatrix} W(z + z_0) & C \\ C & W(z - z_0) \end{bmatrix}. \tag{3.3}$$

[2] $W(z)$ can be any differentiable trapping potential. In this work $W(z) = {}^1\!/\!_2 m\omega_z z^2$ is chosen because the structure and the dynamics of Coulomb crystals in experiments, as well as in theoretical works, are investigated in an harmonic potential (compare chap. 2) mainly.

The parameter C is responsible for the smoothness of this connection. The eigenvalues for this matrix are:

$$\lambda_{\pm} = \frac{1}{2}(W(z+z_0) + W(z-z_0) \pm \sqrt{4C^2 + (W(z+z_0) - W(z-z_0))^2}). \tag{3.4}$$

The lowest eigenvalue of the matrix fulfills the requirements and is chosen as the double well potential:

$$V_{\mathrm{d}}(z) = \frac{1}{2}(W(z+z_0) + W(z-z_0) - \sqrt{4C^2 + (W(z+z_0) - W(z-z_0))^2}). \tag{3.5}$$

The wells of the potential are connected to each other and C is the parameter which controls the height of the barrier B (for harmonic wells $W(z) = {}^1\!/\!_2 m\omega_z z^2$)

$$B = \frac{m}{2}(\omega_z^2 z_0^2 + \frac{C^2}{\omega_z^2 z_0^2}) - mC \qquad \text{with} \quad C \in (0\,, \omega_z^2 z_0^2], \tag{3.6}$$

illustrated in figure 3.1 (a) and (b). The minimums of the wells are located approximately at $\pm z_0$.

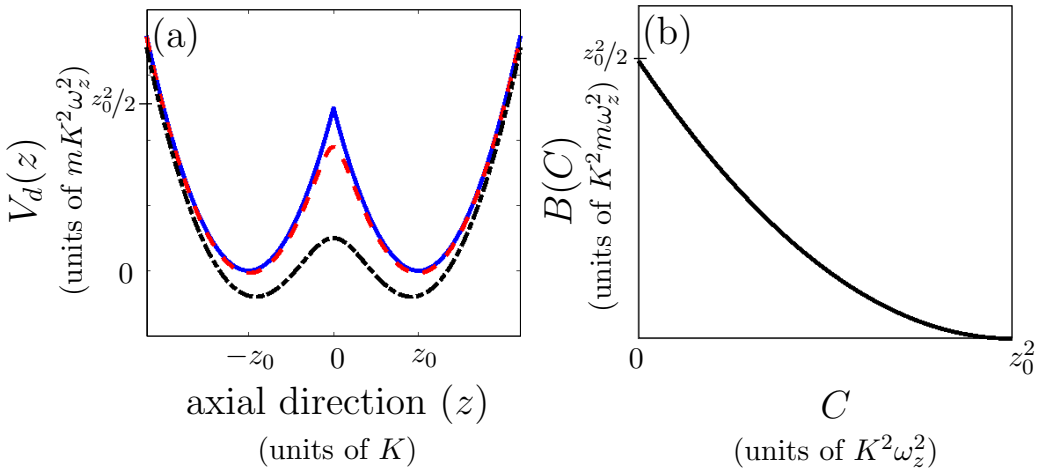

Figure 3.1: (a) The double well trapping potential in axial direction $V_{\mathrm{d}}(z)$ for different values of the smoothness C (blue solid line $C = 0.02$, red dashed line $C = 3$, black dashed-dotted line $C = 10$) and (b) the barrier height B as a function of C (with the scaling factor K equation 3.11).

For the case of the double well potential with harmonic wells $W(z) = \frac{1}{2}m\omega_z z^2$, which is investigated in this work, the Taylor expansion of V_d around $z = z_0$ provides:

$$\begin{aligned} V_\mathrm{d}(\xi)|_{z=z_0} =& m\omega_z^2\Bigg[z_0^2 - \sqrt{\chi} + \left(z_0 - \frac{z_0^3}{\chi^{1/2}}\right)\xi + \frac{1}{2}\left(1 - \frac{z_0^2}{\chi^{1/2}} + \frac{z_0^6}{\chi^{3/2}}\right)\xi^2 \\ &+ \frac{1}{2}\left(\frac{z_0^5}{\chi^{3/2}} - \frac{z_0^9}{\chi^{5/2}}\right)\xi^3 + \frac{1}{8}\left(\frac{z_0^4}{\chi^{3/2}} - \frac{6z_0^8}{\chi^{5/2}} + \frac{5z_0^{12}}{\chi^{7/2}}\right)\xi^4 + \mathcal{O}(\xi^5)\Bigg] \end{aligned} \tag{3.7}$$

with $\xi = z - z_0$ and $\chi = C^2 + z_0^4$. For $C \to 0$ it results in $\chi \approx z_0^4$ and therefore

$$\begin{aligned} V_\mathrm{d}(\xi)|_{z=z_0} =& m\omega_z^2\Bigg[z_0^2 - z_0^2 + \left(z_0 - \frac{z_0^3}{z_0^2}\right)\xi + \frac{1}{2}\left(1 - \frac{z_0^2}{z_0^2} + \frac{z_0^6}{z_0^6}\right)\xi^2 \\ &+ \frac{1}{2}\left(\frac{z_0^5}{z_0^6} - \frac{z_0^9}{z_0^{10}}\right)\xi^3 + \frac{1}{8}\left(\frac{z_0^4}{z_0^6} - \frac{6z_0^8}{z_0^{10}} + \frac{5z_0^{12}}{z_0^{14}}\right)\xi^4 + \mathcal{O}(\xi^5)\Bigg] \\ =& \frac{1}{2}\omega_z^2\xi^2 + \mathcal{O}(\xi^5). \end{aligned} \tag{3.8}$$

s Thus such a potential leads to individual approximately harmonic wells of frequency ω_z centered at $\approx \pm z_0$.

The combination of the double well potential (eq. 3.5) and the time averaged potential (eq. 3.2) of a linear trap yields

$$\begin{aligned} V(x,y,z) =& V_\mathrm{av}(x,y) + V_\mathrm{d}(z) \\ =& \frac{m}{2}\left(\omega_x^2 x^2 + \omega_y^2 y^2\right) \\ &+ \frac{1}{2}\left[\frac{m}{2}\omega_z^2(z+z_0)^2 + \frac{m}{2}\omega_z^2(z-z_0)^2 + \sqrt{4C^2 + \left(\frac{1}{2}m\omega_z^2(z+z_0)^2 - \frac{1}{2}m\omega_z^2(z-z_0)^2\right)^2}\right] \\ =& \frac{m}{2}\left(\omega_x^2 x^2 + \omega_y^2 y^2 + \omega_z^2(z^2+z_0^2)\right) - \sqrt{C^2 + m^2\omega_z^4 z^2 z_0^2}. \end{aligned} \tag{3.9}$$

3.2 General Hamiltonian

Under the aforementioned assumptions, the total Hamiltonian of the system, including the radial trapping potential $V_{\mathrm{av}}(x,y)$, the axial trapping potential $V_{\mathrm{d}}(z)$ and the Coulomb interactions among the N ions reads as

$$\begin{aligned} H(\{\mathbf{r}_i,\mathbf{p}_i\}) =& \sum_{i=1}^{N}\frac{{\mathbf{p}_i}^2}{2m}+\sum_{i=1}^{N}\left[V_{\mathrm{d}}(z_i)+V_{\mathrm{av}}(x_i,y_i)\right] \\ &+\frac{1}{2}\sum_{i}^{N}\sum_{j,j\neq i}^{N}\frac{Q^2}{4\pi\epsilon_0 r_{ij}} \end{aligned} \tag{3.10}$$

with the position $\mathbf{r}_i=(x_i,y_i,z_i)$, the impulse of the i^{th} ion $\mathbf{p}_i=(p_x,p_y,p_z)$ and the distance between ion i and j $r_{ij}=|\mathbf{r}_i-\mathbf{r}_j|$. By rescaling the time, introducing the scaling factor

$$K\equiv[Q^2/(4\pi\epsilon_0 m\omega_z^2)]^{1/3} \tag{3.11}$$

and defining

$$\begin{aligned} &t^*=\omega_z t;\ x^*=\frac{x}{K};\ y^*=\frac{y}{K};\ z^*=\frac{z}{K};\ z_0^*=\frac{z_0}{K};\ r_{ij}^*=\frac{r_{ij}}{K}; \\ &C^*=\frac{C}{K^2\omega_z^2};\ \alpha=\frac{\omega_x}{\omega_z};\ \beta=\frac{\omega_y}{\omega_z}. \end{aligned} \tag{3.12}$$

one arrives at the dimensionless Hamiltonian H^*. Note that the star is omitted for simplicity and all results are represented in these dimensionless units from now on. The resulting Hamiltonian for the linear trap with a double well potential in axial direction (eq. 2.2.4) is given by

$$\begin{aligned} H(\{\mathbf{r}_i,\mathbf{p}_i\}) =& \sum_{i=1}^{N}\mathbf{p}_i^2+\sum_{i=1}^{N}\left[\frac{1}{2}\left(\alpha^2x^2+\beta^2y^2+z^2+z_0^2\right)-\sqrt{C^2+z^2z_0^2}\right] \\ &+\frac{1}{2}\sum_{i}^{N}\sum_{j,j\neq i}^{N}\frac{1}{r_{ij}}. \end{aligned} \tag{3.13}$$

This Hamiltonian describes N ions trapped in a double well potential composed of harmonic wells. The corresponding equations of motion read

$$\ddot{x}_i = -\alpha^2 x_i + \sum_{i,j\neq i}^{N} \frac{x_i - x_j}{r_{i,j}^3} \tag{3.14}$$

$$\ddot{y}_i = -\beta^2 y_i + \sum_{i,j\neq i}^{N} \frac{y_i - y_j}{r_{i,j}^3} \tag{3.15}$$

$$\ddot{z}_i = -2z_i + \frac{z_i z_0^2}{\sqrt{C^2 + z_i^2 z_0^2}} + \sum_{i,j\neq i}^{N} \frac{z_i - z_j}{r_{i,j}^3}. \tag{3.16}$$

These differential equations of motion are not solvable numerically. The preparation of the initial state and an overview over the solving algorithm are presented in the next chapter.

CHAPTER 4

Numerical Algorithms

The presented work deals with the numerical simulation of the classical dynamics of ions arranged as Coulomb crystals (CCs) out of their equilibrium state. The lowest-energy equilibrium configuration is used as initial state which is then excited either by a displacement of an ion (chap. 5) or by a quench of the trapping potential (chaps. 6, 7). In this chapter, the initial state preparation and the numerical algorithms to solve the equation of motion are discussed. The description of the algorithms follows [98, 99].

4.1 Initial state

To prepare the initial state for the simulations, equilibrium configurations have to be found. Since the number of metastable configurations increases exponentially with the number of ions, it becomes extremely difficult to find the minimum energy state. In general Monte-Carlo [100] or Molecular Dynamics simulations [101, 102] are employed to derive the energetically lowest equilibrium configuration.

Numerical algorithms, which use random sampling of variables to approximately solve or simulate a process, are referred as Monte-Carlo methods (MC). In many cases such a stochastic algorithm is the only simulation method, which is able to yield reliable results at manageable computational costs. The basic MC strategy consists of four ingredients: the random variables, the probability distribution function (PDF), moments of the PDF and the variance. The random sampled variables build the foundation of the MC strategy. Furthermore, the mathematical or physical system has to be described by a PDF. Finally, one needs to perform a high number of such simulations since the result has to be averaged over multiple realizations (moments of the PDF) with the variance $\sigma \approx 1/\sqrt{N}$ (N number of samples).

The molecular dynamic algorithm (MD) solves the classical N-body problem starting with a random initial particle distribution and employing the given boundary conditions.

The Newtonian equations of motion of the chosen ensemble, including a cooling or damping term, are solved iteratively with an integration algorithm (e.g. Runge-Kutta [99]) until all particles come to a rest (in the classical description, their momenta become zero) in a minimum of the energy surface.

Both above discussed algorithms are in principle applicable for all kinds of external potentials, but are both computationally demanding. For a well investigated system with a high degree of symmetry such as the harmonic potential, a third simpler strategy can be used.

With a good initial guess for the CC structure the equilibrium position of the ions can be calculated by minimizing the energy with the help of a root finding algorithm. The wells of the trap potential in equation 3.9 are approximately harmonic and the CC structures in the harmonic potential [38, 101, 103] are well investigated. Hence, in this work, the strategy is to determine the CC structures by arranging the ions, using the harmonic configurations from literature, one CC per well, and exploiting a root finding algorithm.

4.1.1 Root finding algorithm

The algorithm used to determine the energetically minimal structure (root finding algorithm) is a modified version of the Powell Hybrid method from the GNU scientific library [99]). To find the equilibrium state of N ions in the double well potential (eq. 2.2.4, the root of the derivative of the energy for ion i

$$\mathbf{g}_i(x_i, y_i, z_i) = \begin{pmatrix} \alpha^2 x_i - \sum_{j\neq i}^{N} \frac{x_i - x_j}{r_{i,j}^3} \\ \beta^2 y_i - \sum_{j\neq i}^{N} \frac{y_i - y_j}{r_{i,j}^3} \\ 2z_i - \frac{z_i z_0^2}{\sqrt{C^2 + z_i^2 z_0^2}}) - \sum_{j\neq i}^{N} \frac{z_i - z_j}{r_{i,j}^3}. \end{pmatrix} \tag{4.1}$$

has to be found for all ions.

Here, for simplicity, the general formalism is presented for $f(s)$. Starting with an initial guess s_0, the value for the function $f(s)$, will become closer to zero for every iteration step n from s_n to s_{n+1}.

The Powell Hybrid method combines the Newton algorithm [99] with a gradient direction. The algorithm uses a trust region to find the direction of the next step in a multidimensional landscape. This trust region is characterized by the condition $|D(s_{n+1} - s_n)| < \delta$. Where δ is the size of the trust region chosen by the algorithm without knowing whether the root is within the region. D is a diagonal scaling matrix whose components are computed internally, using the column norms of the Jacobian [99].

Each new iteration step is determined using the Newton algorithm [99] to solve

$$Jds = -f \tag{4.2}$$

The solution s^* has to be in the trust region. Then s^* is taken as the next step in the iteration $s_{n+1} = s^*$. If this is not the case a linear combination of the outcome of the Newton method and gradient direction

$$ds = -\alpha J^{-1} f(s) - \beta \nabla |f(s)|^2 \tag{4.3}$$

is computed. This solution is again tested by evaluating, if s^* is in the trust region and $f(s^*)$ is closer to zero than $f(s_n)$, than is $s_{n+1} = s^*$ and the trust region is increased to improve the propability that the root is in this region. If this is not the case, the trust region is decreased to guide the algorithm in another direction of the landscape. The above procedure is repeated until an error occurs, the maximum iteration number is reached or a user specified precision ϵ is achieved. The precision here is calculated by

$$|f| < |\epsilon|. \tag{4.4}$$

This is a fast method for finding an equilibrium configuration if the initial guess is close to the equilibrium.

4.1.2 The double well configurations

One configuration of a Coulomb crystal (CC), introduced in section 2.1, is chosen as the initial distribution of the ions in a well. Each well holds one CC which interacts with its neighboring CC via the Coulomb interaction. Each CC is prepared in the lowest energy equilibrium configuration for a chosen symmetry, which will be called ground state (GS) throughout this work. The ansatz to treat the ion configurations as two separated but interacting CCs limits the number of ions per well.

The chosen configuration does not necessarily have to be the global ground state of all ions which would be the lowest energy of all ions of both wells. The global ground state is a configuration in which the number of ions per well is as uniformly as possible distributed ($N_1 = N_2$ or $N_1 = N_2 \pm 1$). The wells of the double well potential (eq. 3.9) are an approximation to the well investigated harmonic potential (compare eq. 3.8). Hence, the ground state configurations of N_i ($i = 1, 2$) ions trapped in the corresponding harmonic potential (same frequency ratios α and β and shifted in axial direction by $\pm z_0$) are close to the GS configuration of N_i ($i = 1, 2$) ions trapped in one of the wells (see fig. 4.1).

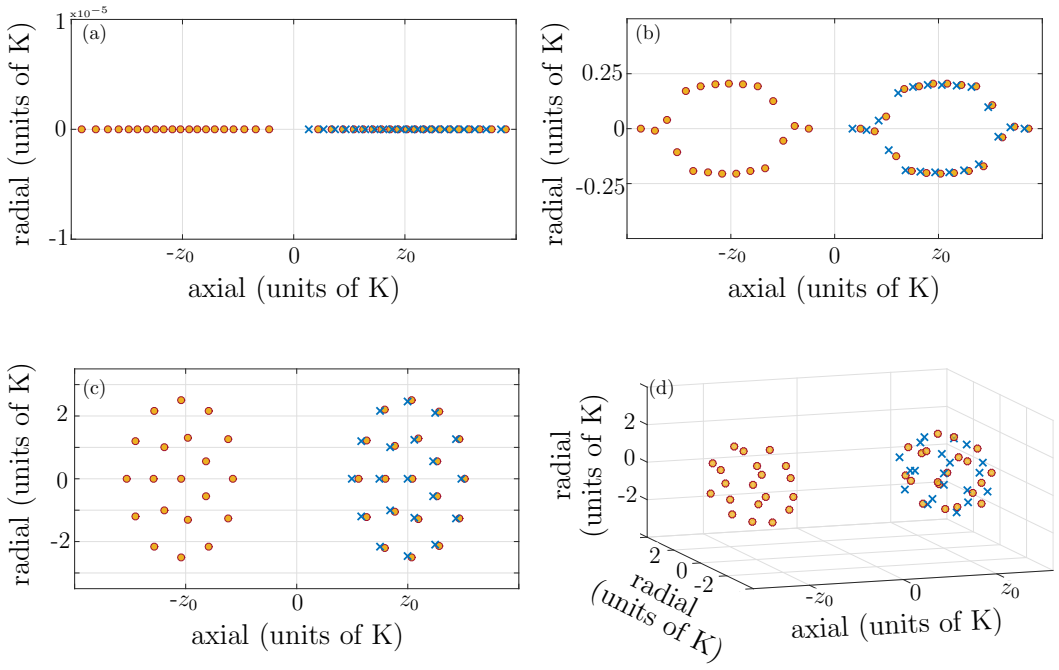

Figure 4.1: Comparison of the GS structures for the harmonic potential (blue crosses) centered at $z_0 = 5$ and the double well potential (orange circles) for the (a) the linear chain, (b) the zigzag chain, (c) circles and (d) spheres

The interaction of the two CCs results in a compression in axial direction and a shift of the center of mass compared to the harmonic system (see fig. 4.1). For the circular ($\alpha = 8, \beta = 1$) and the spherical ($\alpha = 1, \beta = 1$) configurations with $N = 20 + 20$, this is of the order of $1 - 4\%$.

In the case of the linear chain the compression can result in a phase transition to the zig-zag chain [36, 38, 67]. In an harmonic potential this transition follows the principle of a critical value

$$\alpha_c = {}^{3N}/_{4\sqrt{\log N}} = \frac{\omega_x}{\omega_z}\Big|_{\text{transition}} \tag{4.5}$$

for large number of ions ($N \gg 1$) (fig. 4.2, blue line). The critical value is the frequencies ratio of the confinement of the trapping potential at which the transition from linear to zig-zag chain takes place. For small N the critical frequency ratio in the harmonic well is smaller than α_c (fig. 4.2, red dots). For the symmetrically populated double well potential ($N_1 = N_2$) α_c is larger than in the harmonic well (fig. 4.2, black crosses). The difference grows with the number of ions.

The Coulomb interaction of two crystals in the double well potential changes the

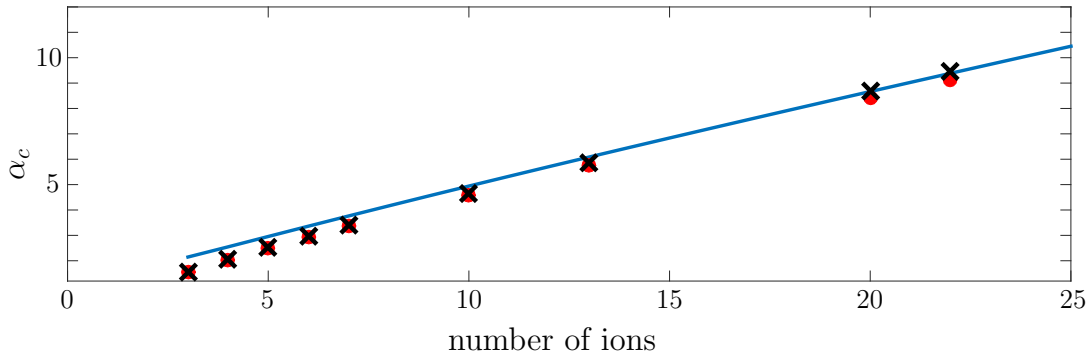

Figure 4.2: Comparison of the critical value α_c of the second order phase transition (linear to zig-zag chain) for the harmonic potential (red dots) and the double well potential with the parameters $z_0 = 5$, $C = 0.02$ (black crosses) calculated with the root finding algorithm and the principle equation for α_c from equation 4.5 (blue line).

effective potential (Coulomb interaction of the neighbored crystal and the trap potential) and causes a deformation of the CC in axial direction. This results in a change of the critical value, which implies that the transition from the linear to the zigzag chain happens at higher values for α_c (compare fig. 4.2). With this knowledge the parameter used in the simulations for the potential are chosen far from the critical ratios for this transition.

In the simulations using the zig-zag configurations, the number of particles and the parameters are chosen such that the shape of the structures is well defined zig-zag chains with large radial dilation in the center of the chains and small radial dilation at the ends.

In all cases, the distance of the potential wells (z_0) is chosen such that the wells are close to harmonic potentials but the Coulomb interaction of the CCs should be nevertheless strong enough for intra crystal effects.

For all simulations in this work, the number of particles should be small because the computation time scales as $\mathcal{O}(N^3)$.

4.2 Solving the equations of motion

The computed GS is disturbed by a displacement of one ion (chap. 5) or by a quench in the barrier height (chaps. 6 and 7) which induces movement of the ions. The solution for the out-of-equilibrium dynamics is obtained by solving the 3N coupled differential equations (see eq. 3.16), in which N particles interact via the Coulomb force and are confined in an external potential (see eq. 2.2.4) is given by $3N$ coupled differential equations (eq. 3.16). Therefore, the equations are solved numerically with the help of an implicit Gaussian 4th order Runge-Kutta algorithm [99].

The Runge-Kutta algorithm is an iterative method used to approximate the solution of ordinary differential equations with given initial conditions. The idea is to provide an intermediate step in the computation of ξ_{n+1} ($\xi = x_i, y_i, z_i$) with the following definitions:

$$\frac{d\xi(t)}{dt} = f(\xi, t), \tag{4.6}$$

$$\xi(t) = \int f(t, \xi)dt. \tag{4.7}$$

After discretizing time one gets

$$\xi_{n+1} = \xi_n + \int_{t_n}^{t_{n+1}} f(t, \xi)dt. \tag{4.8}$$

By employing an approximation for the integral (eq. 4.8), based on the order of the Runge-Kutta method, the equation can be solved. In this work the Simpson rule [104] is used to compute the integral (eq. 4.8) in an approximated way. Defining a finite step size h¿0 and setting $\xi(t_n + h/2) = \xi_{n+1}$ and $t_{n+h/2} = t_{n+1/2}$ the integral becomes

$$\int_{t_n}^{t_{n+1}} f(t)dt \approx \frac{h}{6}[f(t_n, \xi_n) + 4(f(t_{n+1/2}, \xi_{n+1/2}) + f(t_{n+1}, \xi_{n+1}))] + \mathcal{O}(h^5). \tag{4.9}$$

This in turn means:

$$\xi_{n+1} = \xi_n + \frac{h}{6}[f(t_n, \xi_n) + 4(f(t_{n+1/2}, \xi_{n+1/2}) + f(t_{n+1}, \xi_{n+1}))] + \mathcal{O}(h^5). \tag{4.10}$$

The algorithm works as follows:

1. The slope $k_1 = hf(t_n, \xi_n)$ at t_n is calculated.
2. The slope at the midpoint is computed: $k_2 = hf(t_n + h/2, \xi_n + k_1/2)$.
3. The improved slope at the midpoint results in: $k_3 = hf(t_n + h/2, \xi_n + k_2/2)$.
4. With this, the slope $k_4 = hf(t_n + h, \xi_n + k_3)$ can be computed.
5. The new iteration value is :

$$\xi_{n+1} = \xi_n + \frac{1}{6}(k_1 + 2k_2 + 2k_3 + k_4) \tag{4.11}$$

Computing the new value ξ_{n+1} requires four function evaluations. The fourth order Runge-Kutta method has a global truncation error of $\mathcal{O}(h^5)$ [98]. Using this algorithm one gets a data set of the form $t_n, x_i(t_n), y_i(t_n), z_i(t_n), \dot{x}_i(t_n), \dot{y}_i(t_n), \dot{z}_i(t_n)$ for each simulation step t_n. In the following chapters, these data sets are the basis for the investigation and analysis of the interaction of two coupled Coulomb crystals in the double well potential (eq. 3.9).

CHAPTER 5

Characterization of the interaction of two Coulomb crystals

An exemplary system to investigate the interaction of separated Coulomb crystals (CCs) is that of CCs in potentials with multiple wells. The chosen model consists of a double-well potential (eq. 3.9) with a trapped CC in each of the two wells. As discussed in the previous chapter, the coupling of the CCs depends on the parameters C_i and z_0 of the potential. The dynamical behavior of these CCs is investigated in this chapter for the initial values $C_i = 0.02$ and $z_0 = 5$. The study focuses on the case of equally populated potential wells corresponding to a trap with aspect ratios $\alpha = 5.6$ and $\beta = 8$, allowing for a ground state consisting of two identical zig-zag chains ($N_1 = N_2 = 22$ ions) confined in each well, which is assumed to be the initial configuration.

In a first approach to understand the basic behavior of the coupled CCs, the potential parameters are kept constant and only one of the outermost ions (ion **1**, see fig. 5.1) is displaced either in the axial (z-coordinate) or in the radial direction (x coordinate). Already this simple case of coupled CCs displays interesting dynamics initiated by the displacement of the ions, including an energy transfer between the crystals and the onset of ion transfer over the potential barrier.

As a first attempt to show the impact of interaction between the two CCs separated by a potential barrier, the energy transfer between them is studied. A small displacement of ion **1** (fig. 5.1) in the radial or in the axial direction introduces a small change of the total energy (sum of the kinetic and the potential energy) in one of the crystals (CC **1**). In a decoupled system the total energy of each crystal will remain constant after the initial displacement. In contrast, if the two CCs are coupled, the excited CC **1** can transfer energy to the neighboring crystal (CC **2**). In the next subsection 5.1 the time evolution of the energy of both CCs is analyzed in order to examine the strength of their coupling.

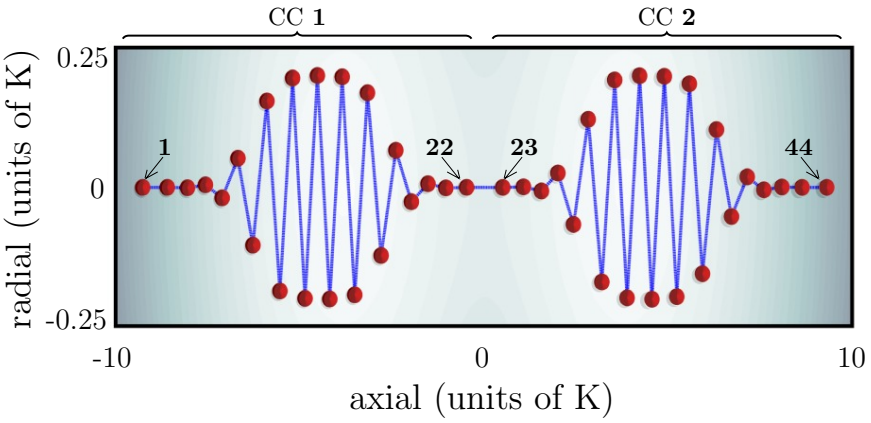

Figure 5.1: Schematic representation of the initial zig-zag ground state configuration of the ions in a double well potential with $\alpha = 5.6$, $\beta = 8$, $C_i = 0.02$ and $z_0 = 5$.

5.1 Energy transfer

Here, in a system of two zig-zag CCs the energy dynamics, introduced by the displacement of ion **1** in the axial direction, e.g. $\Delta z = 0.2$, is investigated. In figure 5.2 the time evolution of the total energy (kinetic and potential energy) for both crystals is shown for long times (approximately 90 periods of the oscillation of ion **1**). Obviously, the total energy of CC **2** is not constant, i.e. an amount of energy is transfered from the excited crystal to crystal **2** and back. The total energy of both crystals evolves in anti-phase and the energy transfer occurs fast in less than half a period of oscillation of ion **1** as depicted in figures 5.2(a) and (b).

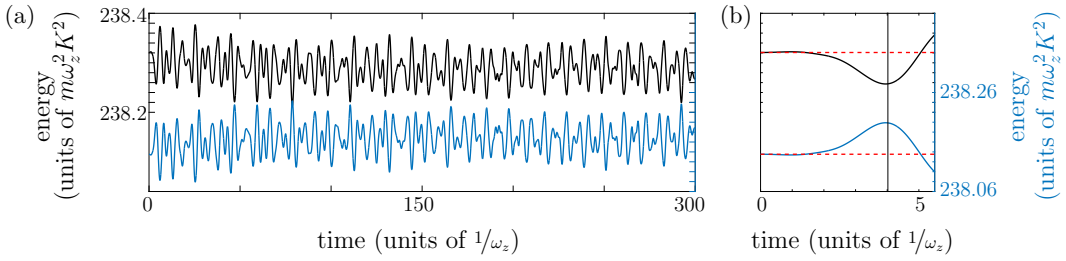

Figure 5.2: Time evolution of the total energy of the excited crystal **1** (black) and crystal **2** (blue) in the course of the dynamic (up to final time (a) $t_f = 300$ and (b) $t_f = 5.5$) for a displacement of ion **1** in the axial direction ($\Delta z = 0.2$).

For each of the two CCs the potential energy consists of two contributions, the Coulomb energy between the ions and their potential energy due to the trap. The

energy transfer affects both of these contributions as shown in figure 5.3 (a). For both CCs the Coulomb energy and the trap potential energy oscillate in time with a phase difference π between them (figs. 5.3 (a) and 5.4 (a)). The amplitudes of the oscillations are roughly $\Delta E = 0.02$ in CC **1** (fig. 5.3 (a)) and $\Delta E = 0.01$ in CC **2** (fig. 5.4 (a)) indicating a considerable amount (approximately 50 %) of energy transfer as shown in figure 5.5. The total potential energies of the two CCs oscillate also in time with a phase difference of π indicating their correlation.

The sum of kinetic energies of all ions in both crystals is more than two orders of magnitudes lower (see figs. 5.3 (a) and 5.3 (b)) compared to the contribution of the total potential energy. The reason for this is, that even a small change in the position of an ions results in a large change in the Coulomb energy as well as in the trapping potential energy.

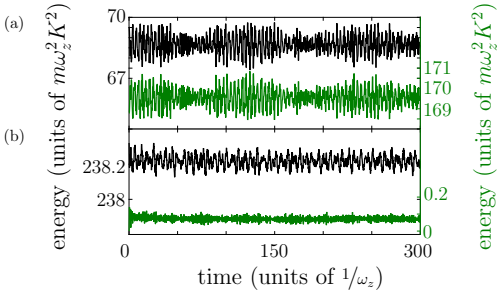

Figure 5.3: For the perturbed crystal: Time evolution of (a) trapping potential (black) and Coulomb energy (green) (b) trapping potential plus Coulomb energy (black) and kinetic energy.

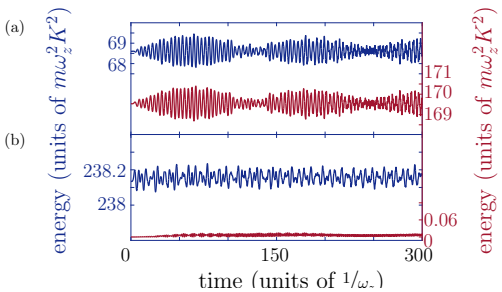

Figure 5.4: For the unperturbed crystal: Time evolution of (a) trapping potential (blue) and Coulomb energy (red) (b) trapping potential plus Coulomb energy (blue) and kinetic energy (red).

To summarize, the displacement of an outermost ion of one crystal influences considerable of the time evolution of the energy in both crystals. While the kinetic energy of all ions is almost unaffected, the change of the total potential energy of both CCs dominates the energy transfer, indicating a strong Coulomb coupling between them.

Another possibility to show the effect of coupling between two CCs is to compare the motion of ions in the crystals **1** and **2** initiated by a displacement of an outermost ion. In subsection 5.2 these motions are characterized allowing to estimate the propagation of excitation above the potential barrier.

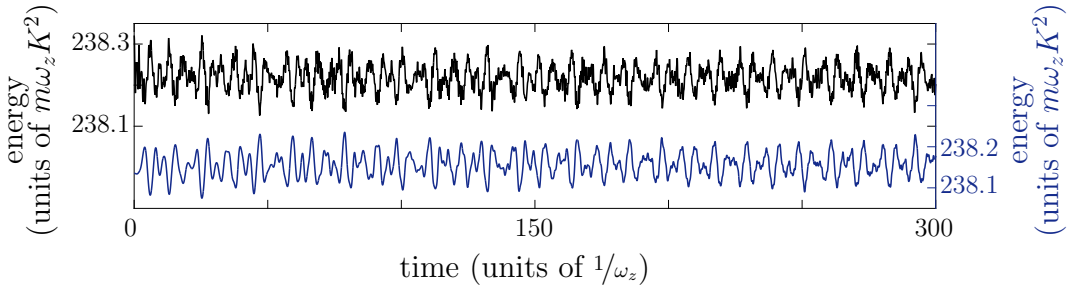

Figure 5.5: The counter propagating total potential energy of the perturbed (black) and unperturbed (blue) crystal.

5.2 Excitation propagation

As discussed in the previous section 5.1, a considerable amount of energy is transfered between the CCs trapped in the double well potential. Although the ratio of kinetic energy compared to the potential energy of the particles is small, the energy transfer affected by the dynamics of the ions provides significant insight to understanding of the coupling. As in section 5.1 the initial configuration is the symmetric double zig-zag chain with the potential parameters $C_i = 0.02$, $z_0 = 5$, $\alpha = 8$, $\beta = 5.6$, while a displacement of ion **1** excites the system. The initial excitation of ion **1** will delocalized in the course of time as a result of the coupling of ions via the Coulomb interaction. In particular, this excitation will travel in the form of distortion waves through the whole CC. The pattern of the waves is expected to be different depending on whether displacement is radial or axial, discussed separately in subsections 5.2.1 and 5.2.2, respectively.

In order to help the reader to identify different characteristic wave patterns in the dynamics of individual ions, some toy examples [3] of possible wave dynamics are presented in figures 5.6 and 5.7. In figure 5.6(a) the simplest possible case is plotted when all ions in the CC oscillate in phase with the same amplitude. With the index number of the ion on the x-axis and the time on the y-axis, the amplitude of each ion is encoded by color, leading to the stripes. Introducing a small phase shift between the ions, causes waves travel through the crystal and the formerly horizontal stripes will become tilted (fig. 5.6(b)). The checkerboard pattern in figure 5.6(c) is caused by a phase shift of π and can be interpreted as an opposite motion of neighboring oscillators. A shock wave resulting from an excitation propagating through the crystal (fig. 5.7(a)) can be reflected at the end of the crystal flipping its amplitude (fig. 5.7(b)). A distortion wave can be scattered either in the medium of the crystal itself or hitting another wave prop-

[3] The shown examples assume a cosine motion for the distortion waves and a Gaussian pulse for the shock wave.

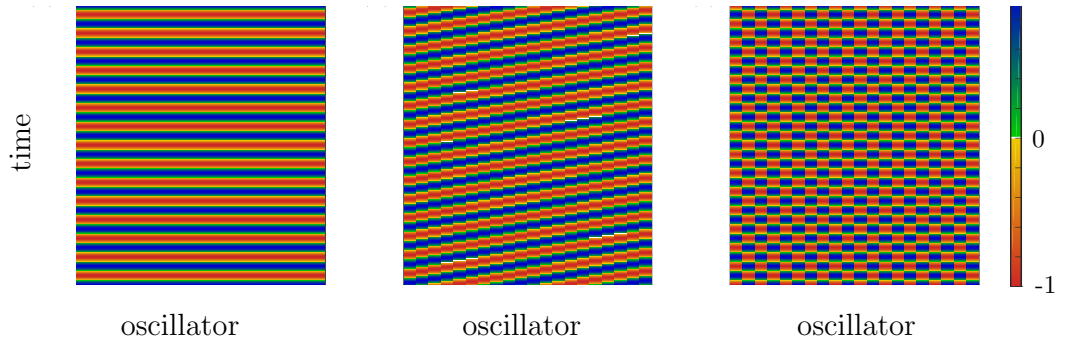

Figure 5.6: Schematic toy examples of ion motions: (a) in phase oscillations of ions, (b) oscillations of ions with a small constant phase difference and (c) oscillations with a phase difference of π between neighboring ions.

agating through the crystal. In both cases bifurcations as in figure 5.7(c) will appear. The different waves (distortion and shock waves) do not appear isolated but in complex combinations. An example for such a combination of a shock wave (fig. 5.7(c)) propagating in the background of ions oscillating in phase (fig. 5.6(a)) is shown in (fig. 5.7(d)).

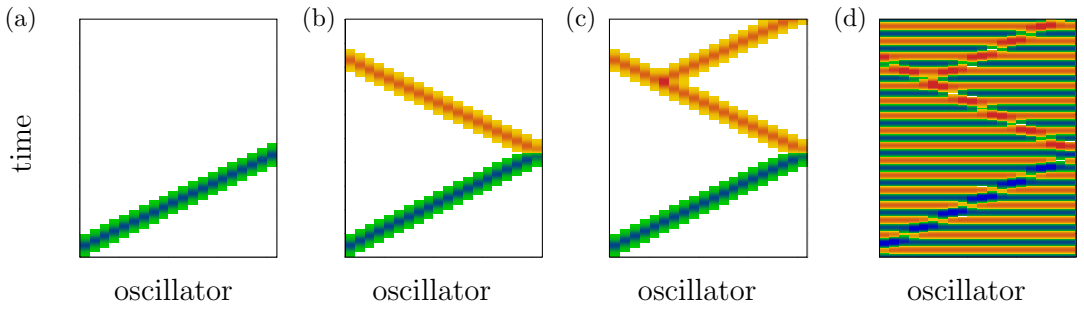

Figure 5.7: Schematic toy examples of a shock wave: (a) propagation through a crystal, (b) reflected on the end of the crystal flipping its amplitude and (c) scattered in the medium, causing bifurcations. (d) Combination of (c) and the case of figure 5.6(a).

There are two possible excitations of ion **1**, a displacement in the radial (x) or in the axial direction (z). The dynamics following the displacement of ion **1**, heavily depends on the magnitude of the displacement. A scan over the magnitudes of the displacement in radial direction Δx and, respectively, in axial direction Δz, as well as the characterization of the dynamics of the ions depending on their axial order are used to categorize the regimes of excitations.

In particular, for values larger than $\Delta x > 0.33$ or $\Delta z > 0.6$ a reordering of the ions in the excited crystal (figs. 5.8(b) and 5.9(b), respectively) can be observed, whereas

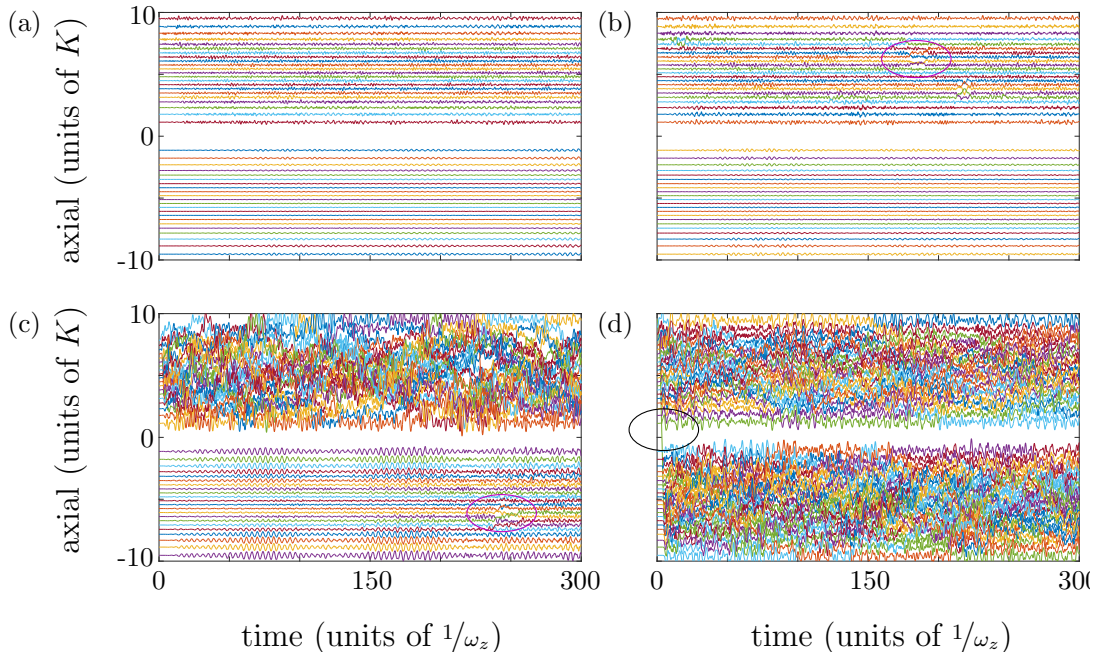

Figure 5.8: The axial position for each ion in the Coulomb crystal to evaluate the order of ions for (a) no reorder in both crystals ($\Delta x = 0.32$), (b) reorder only in the excited crystal ($\Delta x = 0.37$), (c) reorder in both crystals ($\Delta x = 1.64525$) and (d) ion transfer ($\Delta x = 1.745$) by a **radial displacement** (Δx) of ion **1** in the zig-zag chain configuration ($z_0 = 5$, $C = 0.02$, $\alpha = 8$, $\beta = 5.6$). Examples are marked with a pink ellipse for reordering and with a black ellipse for transfer.

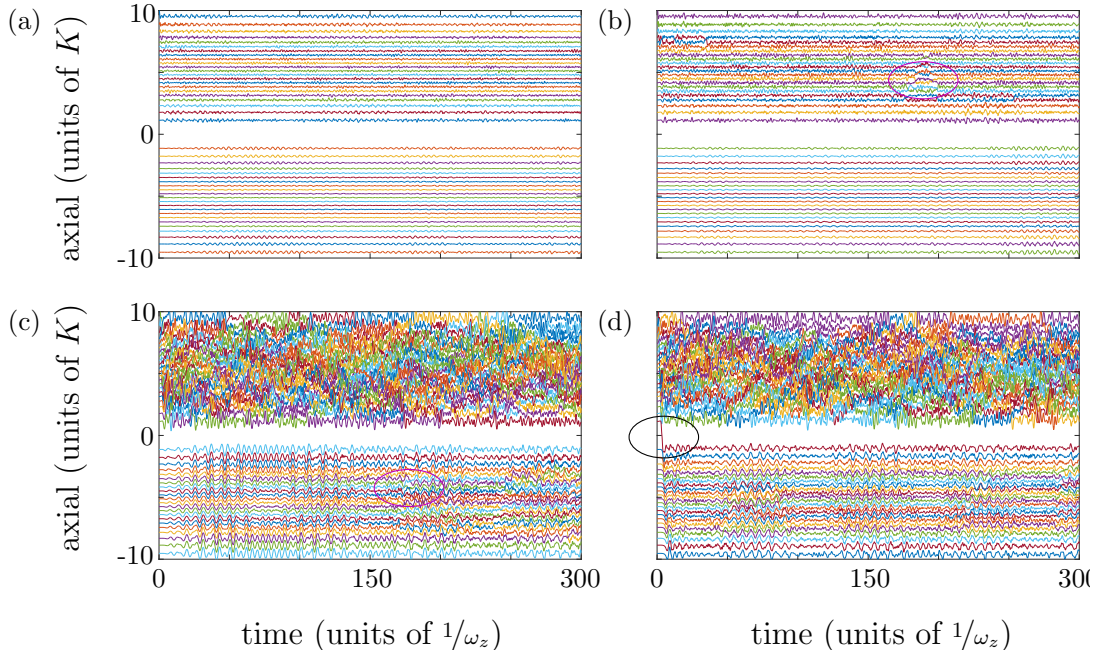

Figure 5.9: The axial position for each ion in the Coulomb crystal to evaluate the order of ions for (a) no reorder in both crystals ($\Delta z = 0.5$), (b) reorder only in the excited crystal ($\Delta z = 0.9$), (c) reorder in both crystals ($\Delta z = 5.11$) and (d) ion transfer ($\Delta z = 5.12$) by an **axial displacement** (Δz) of ion **1** in the zig-zag chain configuration ($z_0 = 5$, $C = 0.02$, $\alpha = 8$, $\beta = 5.6$). Examples are marked with a pink ellipse for reordering and with a black ellipse for transfer.

for values larger then $\Delta x > 1.6445$ or $\Delta z > 5.11$ a reordering in the second crystal (figs. 5.8(c) and 5.9(c), respectively) can also be observed. For values larger then $\Delta x > 1.646$ or $\Delta z > 5.12$ (fig. 5.8(d) and fig. 5.9(d), respectively) even a transfer of an ion above the barrier occurs. Since the focus of the current section is on the study of wave propagation through the CCs, small values for the initial displacement (radial and axial) are chosen such that the ions do not reorder, but perform smooth non-linear oscillations around their equilibrium position in the crystal.

In the subsections (subsecs. 5.2.1 and 5.2.2) the dynamics following a radial (Δx) and an axial (Δz) displacement of the ion **1**, respectively, is investigated.

5.2.1 Radial displacement of the outermost ion 1

Without loss of generality the ion **1** is displaced by $\Delta x = 0.01$, a value, which is much smaller than the radial expansion (maximal radial distance between two ions) $\Delta x = 0.4$ of the initial zig-zag chain[4]. For such a displacement the axial order of the ions is preserved. In order to develop an understanding of the ion dynamic, the analysis concentrates on the time directly after the excitation of the ion **1**, i.e., for a time period $t \leq 30$. Later time periods are dominated by the interference of ion oscillations, making it particularly difficult to distinguish the different contributions.

The displacement of ion **1** alters the total potential energy of ion **1** as well as the total energy of every other ion in the two crystals due to their Coulomb coupling. Therefore, with this displacement the total potential energy of all other ions in the system is altered too. The ions of both CCs start to oscillate in the radial and the axial directions as shown in figures 5.10(b), (c) and 5.11(b), (c), respectively.

A clear view on the time evolution of the radial and axial displacements of ion **1** and **44** is provided by figures 5.10(a),(d) and 5.11(a),(d) allowing for an estimation of the character and the period of their oscillations. Finally, figures 5.10 (e) and 5.11(e) depict the initial configuration of the ions in the CCs, so that their axial position is indicated by the values of the x-axis of figures 5.10(b), (c) and 5.11(b), (c).

In the radial component (figs. 5.10(b),(c)) the displacement shows a tilted stripe structure as the one of figures 5.6(b), indicating the presence of a transversal wave running through the CC. As shown by its distortion this is partly reflected in crystal **1** and partly transmitted in crystal **2**. The amplitude of this wave is largest in the excited crystal (compare fig 5.10(b) and (c)), as expected. Moreover, the dynamics of the oscillation amplitudes exhibits bifurcations in crystal **1** as shown in figure 5.10(b) and (c), whereas the oscillation dynamics in CC **2** is more regular and the tilted stripe

[4]For an impression of the ion dynamics see movie [M.1].

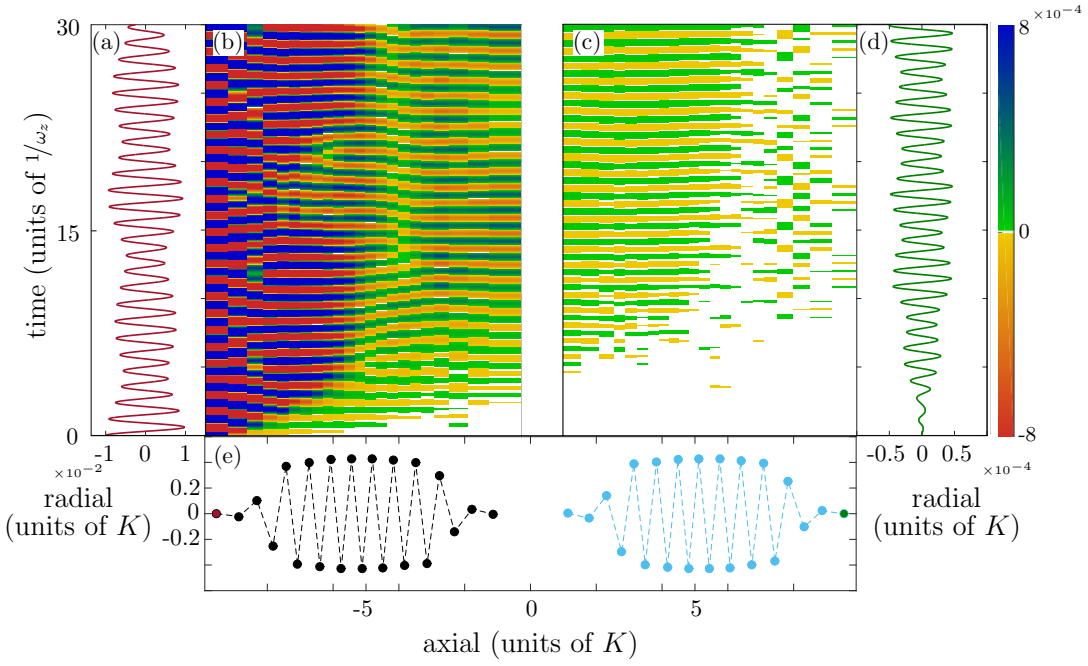

Figure 5.10: For a **radial displacement** ($\Delta x = 0.01$) of the ion **1** in the zig-zag chain configuration ($z_0 = 5$, $C = 0.02$, $\alpha = 8$, $\beta = 5.6$) (a) the radial oscillation of ion **1** around its equilibrium position, (b) the radial oscillations of all ions in crystal **1**, and (c) crystal **2** around their equilibrium positions, (d) the dynamic of ion **44** in radial direction around its equilibrium position and (e) the crystal ground state configuration is depicted. The colors stand for the displacement of each ion from its equilibrium position.

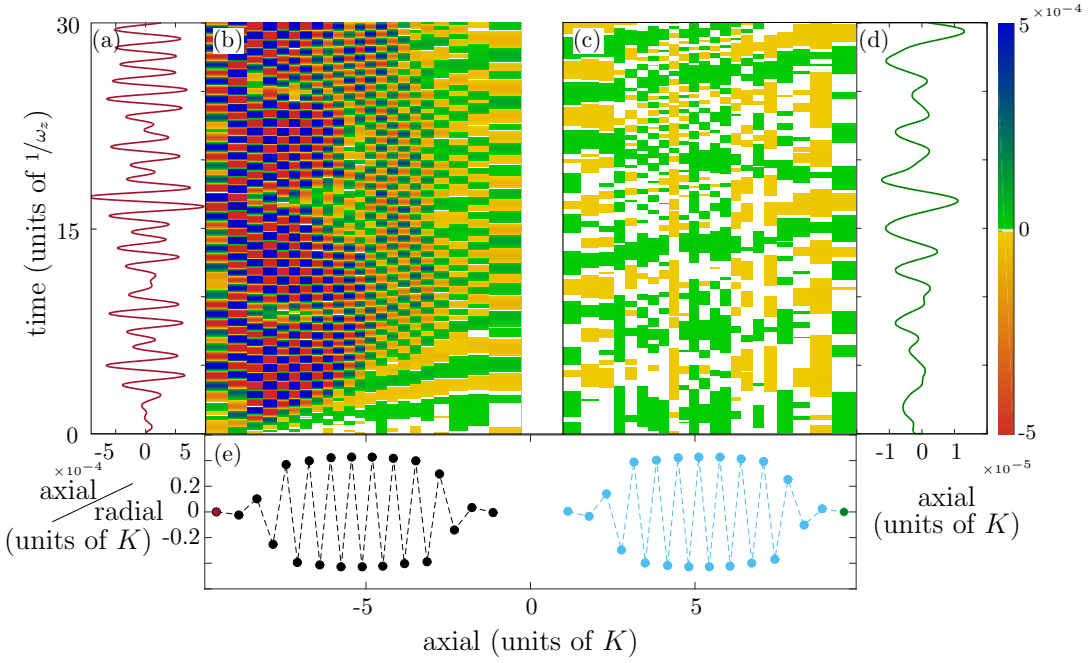

Figure 5.11: For a **radial displacement** ($\Delta x = 0.01$) of the ion **1** in the zig-zag chain configuration ($z_0 = 5$, $C = 0.02$, $\alpha = 8$, $\beta = 5.6$) (a) the axial oscillation of ion **1** around its equilibrium position, (b) the axial oscillations of all ions in crystal **1** and (c) crystal **2** around their equilibrium position, (d) the dynamic of ion **44** in axial direction around its equilibrium position, and (e) the crystal ground state configuration. The colors stand for the displacement of each ion from its equilibrium position.

structure is unperturbed by bifurcations for the shown time period. This is caused by the much smaller oscillation amplitudes in crystal **2** compared to the one in crystal **1**.

The displacement of ion **1** alters the effective potential of the ions resulting, apart from their radial, also in their axial rearrangements, an effect that is stronger in crystal **1**. The ions move collectively closer to the displaced ion and start to oscillate. This results in adumbrating stripes, whose shape changes very fast in the perturbed crystal and leads soon to a checker-board pattern of the amplitude, where neighboring ions oscillate out-of-phase. Note that the amplitudes in the axial direction are half of the corresponding ones in the radial direction.

5.2.2 Axial displacement of the outer most ion 1

In this subsection an outer most ion is displaced in the axial direction away from the barrier[5]. The magnitude of the excitation is in the regime where the order of the ions in the axial direction is preserved. The dynamics for this displacement will be analyzed similarly to the case of radial displacement.

In figure 5.12 and figure 5.13 the dynamics of the ions following the displacement $\Delta z = 0.05$ of ion **1** is shown up to time $t = 30$. For longer times the dynamics is dominated by interference, making it complex to analyze it. The dynamics of ion **1** is depicted in figure 5.12(a) (radial direction) and figure 5.13(a) (axial direction) whereas the dynamics for ion **44** in figures 5.12(d) and 5.13(d). The collective dynamics of the ions is shown for crystal **1** in figures 5.12(b) (radial) and 5.13(b) (axial) respectively and for crystal **2** in figures 5.12(c) (radial) and 5.13(c) (axial) respectively, whereas the ground state configuration is presented in (e).

As shown in subsection 5.2.1 the axial and radial components are coupled and an excitation in one direction generates ion dynamics in both spatial directions. For the axial displacement in the zig-zag chain, the radial component of the dynamics (fig. 5.12) reaches the aforementioned checkerboard-like patterns very fast. The ions come closer in the axial direction during their oscillations, a fact compensated by their spreading in radial direction. This is indicated of the ions moving oppositely to their neighboring ions in order to minimize their Coulomb interaction. It turns out that the subsequent radial oscillations of the ions are two times smaller than the axial one.

In the axial direction the change of the total potential energy, caused by the displacement, results in a longitudinal wave visible in figure 5.13 as a green stripe propagating through crystal **1**. At time $t \approx 2.8$ (fig. 5.18(b) and (c)) the wave reaches ion **22** and then it partly overcomes the barrier and induces ion dynamics in crystal **2**. There, due

[5]For an impression of the ion dynamic see movie [M.2].

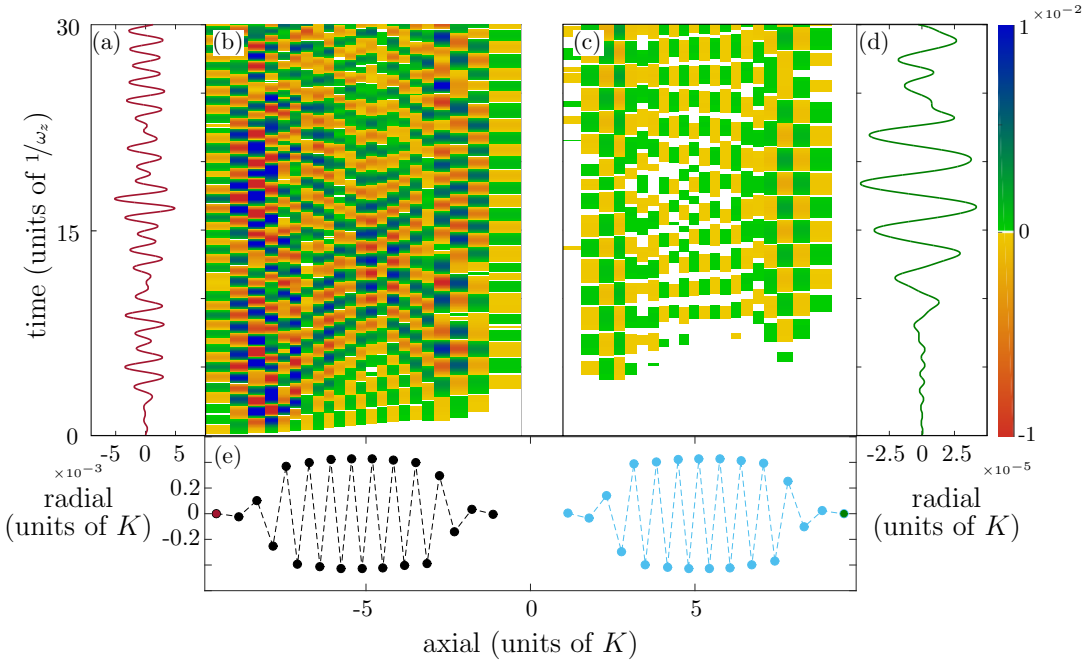

Figure 5.12: For an **axial displacement** ($\Delta z = 0.05$) of the ion **1** in the zig-zag chain configuration ($z_0 = 5$, $C = 0.02$, $\alpha = 8$, $\beta = 5.6$) (a) the radial oscillation of ion **1** around its equilibrium position, (b) the radial oscillations of all ions in crystal **1** and (c) crystal **2** around their equilibrium position, (d) the dynamic of ion **44** in radial direction around its equilibrium position, and (e) the crystal ground state configuration. The colors stands for the distance of the ion from its equilibrium position.

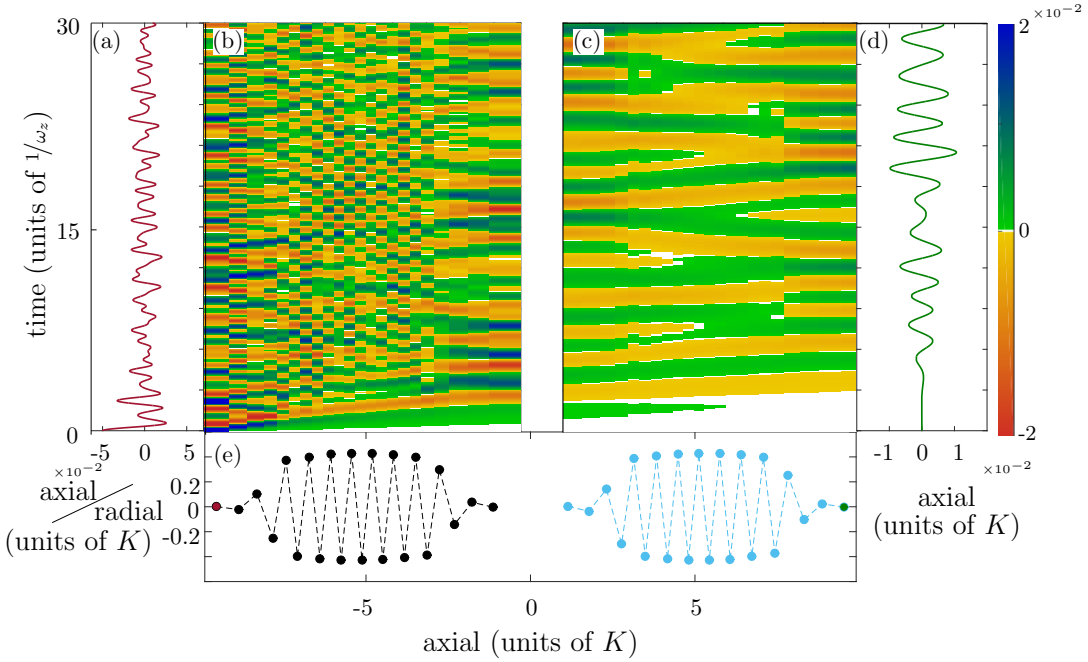

Figure 5.13: For an **axial displacement** ($\Delta z = 0.05$) of the ion **1** in the zig-zag chain configuration ($z_0 = 5$, $C = 0.02$, $\alpha = 8$, $\beta = 5.6$) (a) the axial oscillation of ion **1** around its equilibrium position, (b) the axial oscillations of all ions in crystal **1** and (c) crystal **2** around their equilibrium position, (d) the dynamic of ion **44** in axial direction around its equilibrium position, and (e) the crystal ground state configuration. The colors stands for the distance of the ion from its equilibrium position.

to the small amplitude, the propagation of the longitudinal wave is less influenced by interference, the stripe structure is robust and, in the shown time period, it exhibits only three bifurcations. Due to its larger excitation amplitude, the wave propagation in the excited crystal is more structured (compared to the ion dynamics in crystal **2**) with many bifurcations and an exhibition of the checker-board pattern before the longitudinal wave reaches for the first time the end of crystal **2**. An enlarged picture (fig. 5.18) of (a) the axial dynamics of ion **1**, (b) of all ions in the excited crystal, (c) of ion **22** and (d) the equilibrium configuration of the excited crystal are shown in order to analyze the dynamics in more detail. The longitudinal wave (the first green stripe in figure 5.18(b)), created by the displacement, runs unperturbed through the crystal.

Directly after the longitudinal wave passes ion **2** a second axial distortion influences the subsequent wave dynamics. The second axial distortion is created by the motion of ion **1** from its initial position (displaced by $\Delta z = 0.05$) back to its equilibrium position and runs as a shock wave trough the crystal **1** (fig. 5.18). The shock wave reaches the end of crystal **1** at time $t = 3.49$. The propagation of the shock wave through the crystal is visible in figure 5.18 as the stripe structure superimposed with the longitudinal waves. The shock wave is mainly reflected at the barrier and thus affects less the crystal **2** (fig. 5.13(c)). Due to the crystalline zig-zag structure (fig. 5.14) the waves are scattered at the boundaries of the different parts (outer and inner part) of the crystal. The

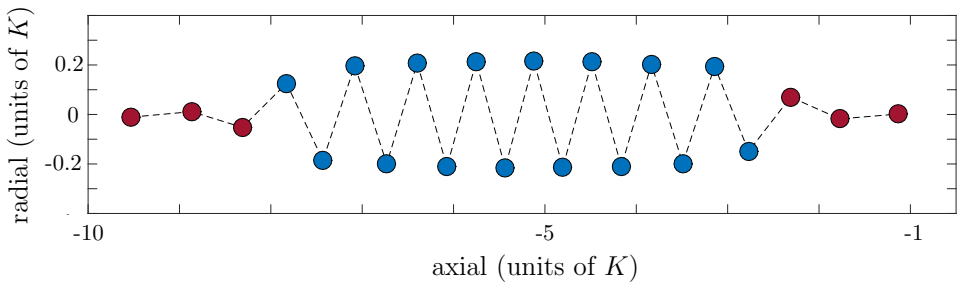

Figure 5.14: Schematic representation of a zig-zag chain configuration divided in the inner part (blue circles) and outer parts (red circles).

scattering of the shock waves produces bifurcations and the interference of the waves results immediately in a checker-board pattern starting on the boundaries of the inner and outer parts of the crystal (compare fig. 5.18), dominating finally the wave dynamics.

In order to visualize better this shock wave the crystal should not exhibit boundary effects and therefore the shock wave dynamic is investigated in the paradigmatic case of a linear chain configuration[6]. In the linear chain configuration the outer ion **1** is displaced

[6]For an impression of the ion dynamic see movie [M.3].

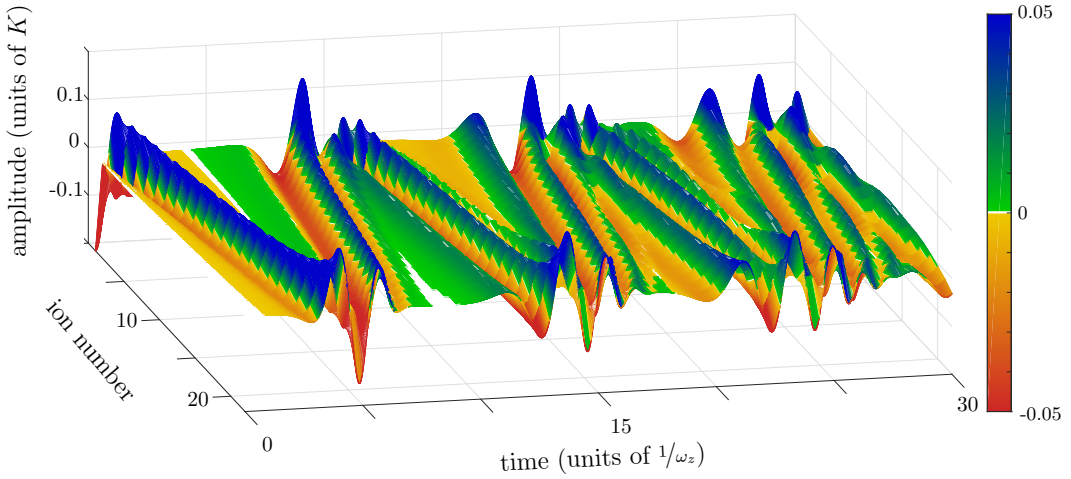

Figure 5.15: Ion dynamics in crystal **1** in the linear chain configuration ($z_0 = 5$, $C = 0.02$, $\alpha = 100$, $\beta = 100$) introduced by the axial displacement $\Delta z = 0.2$ of ion **1**. The oscillations of the ions around their equilibrium position is encoded as color as well as height in the 3 dimensional plot.

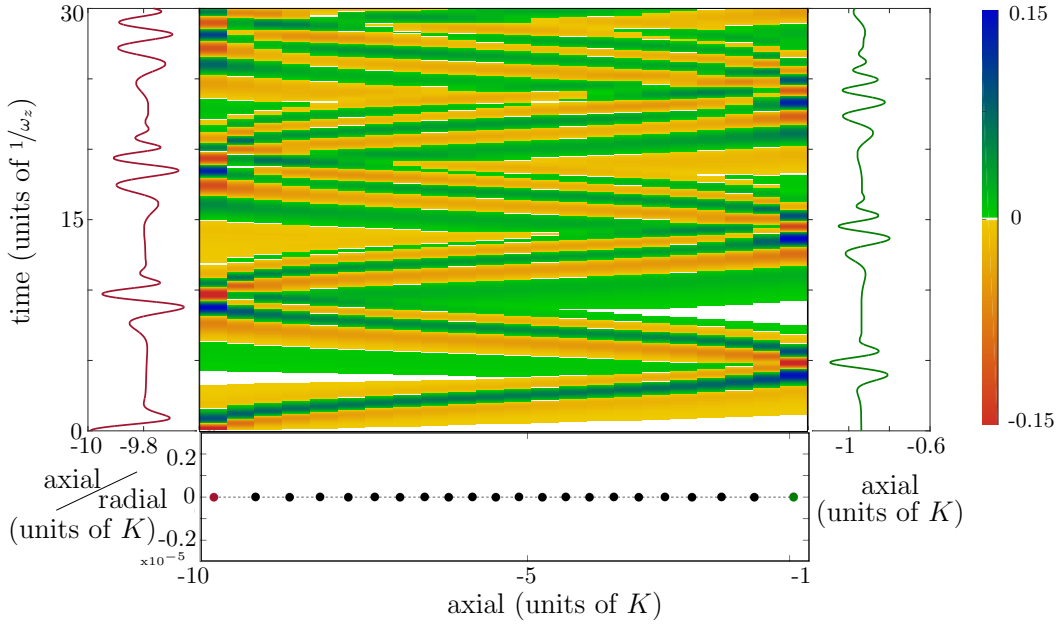

Figure 5.16: Ion dynamics in crystal **1** in the linear chain configuration ($z_0 = 5$, $C = 0.02$, $\alpha = 100$, $\beta = 100$) introduced by the axial displacement $\Delta z = 0.2$ of ion **1** (a) the axial oscillation of ion **1**, (b) the axial oscillations of all ions in crystal **1** and (c) crystal **2** around their equilibrium position, the dynamic of ion **22** in axial direction, and (d) the crystal ground state configuration.

exemplary in axial direction by $\Delta z = 0.2$ away from the crystal. The axial amplitude dynamics of the excited linear chain for crystal **1** is depicted in fig. 5.15 as a three dimensional plot presenting the time evolution of the amplitudes and in figure 5.16(b) as a color plot accompanied by the axial trajectories of ion **1** (a) and **22** (c). In both figures one can clearly observe the propagation of the shock wave. The displacement of ion **1** creates a longitudinal wave (the first yellow/orange stripe) followed directly by the shock wave (the blue/green stripe). The shock wave dominates the wave dynamics visible also in the trajectories of ions **1** and **22** in figures 5.16 (a) and (c). It is reflected at each edge of the crystal and thus propagates through the crystal several times. Note that the scattering at the boundaries is reduced compared to the wave propagation in the zig-zag chain (see fig. 5.18). As in the zig-zag chain the shock wave interferes apart with itself also with the longitudinal waves introduced by the change of the total potential energy following the motion of the ions **1** and **22**. These longitudinal waves affect the shock wave propagation and cause bifurcations when they collide. Once again, one observes that the interference effects are much smaller for the linear chain than for the zig-zag chain. The shock wave is mainly reflected at the barrier (fig. 5.17). After its first propagation through the excited crystal nearly 10% of the shock wave reaches crystal **2**.

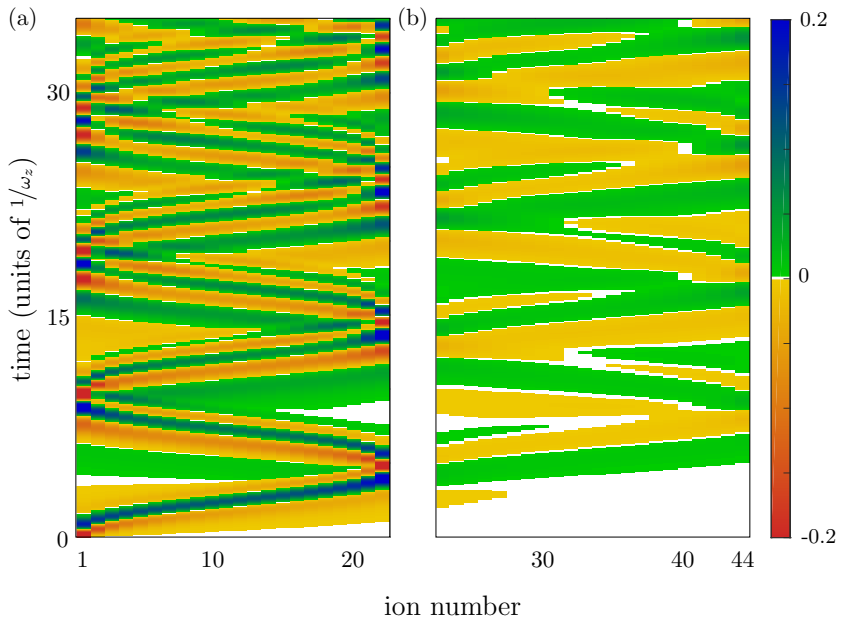

Figure 5.17: Shock wave propagation in the linear chain configuration ($z_0 = 5$, $C = 0.02$, $\alpha = 100$, $\beta = 100$) introduced by the axial displacement $\Delta z = 0.2$ through (a) the excited crystal and (b) crystal **2**.

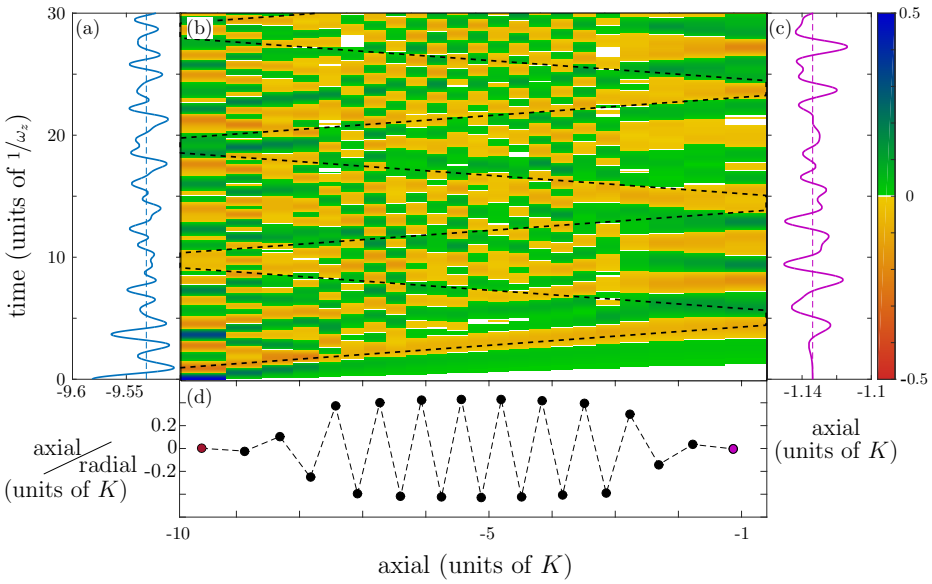

Figure 5.18: Ion dynamics in crystal **1** (axial displacement $\Delta z = 0.05$) in the zig-zag chain configuration ($z_0 = 5$, $C = 0.02$, $\alpha = 8$, $\beta = 5.6$), (a) axial dynamic of ion **1**, (b) the axial oscillations of all ions in crystal **1** around their equilibrium, (c) axial dynamic of ion **22**, and (d) the ground state configuration for crystal **1**. The propagation of the shock wave through the crystal is marked by straight black dashed lines.

From the understanding of the wave dynamics of the linear chain configuration one can identify also for the zig-zag chain configuration the shock wave and its propagation through the excited crystal marked with the black dashed line in figure 5.18. The axial displacement in the zig-zag chain configuration induces a longitudinal wave and a shock wave. The specific structure of the crystals with inner and outer parts induces scattering phenomena in the excited crystal. The interference of the waves results in checker-board patterns directly after the start of the wave propagation.

5.2.3 Conclusions

In this chapter the ion dynamics and the energy propagation in a double zig-zag chain, induced by a displacement of a single ion, is investigated. It turns out, that the main energy transfer takes place between the external potential energy of the double well trapping potential and the Coulomb energy. Furthermore, it was shown by investigating the energy propagation that the two CCs are always strongly coupled by the Coulomb interaction despite the presence of the potential barrier.

The ionic motions depend among others on the direction of the initial displacement. For a radial displacement a stripe-like structure in the radial direction is found, identified as transversal waves propagating through the two crystals. A displacement in the axial

direction induces longitudinal waves as well as a shock wave. The waves generated by the displacement are partly reflected at the barrier and partly overcome the barrier initiating also a motion in the second crystal. The propagation of the shock wave, in contrast to the longitudinal wave, is reflected on the barrier up to 90%. The zig-zag chain configuration consists of an inner and two outer parts. The boundaries between these parts induce scattering effects which influence strongly the propagation of the shock wave. As a result of the interaction of the two existing waves including their reflections in the crystal structure, bifurcations can be also found. Each directed displacement of a single ion, either in the radial or in the axial direction, induces oscillations of all ions even in the initially unexcited direction (axial or radial, respectively). For both kinds of initial displacements a checker-board pattern for the ion dynamics can be found in all directions of motion. This pattern results from the interference of different waves which dominates the long time ($t \gg 500$) crystal dynamics.

CHAPTER 6

Quench dynamics of coupled zig-zag ion chains of equal size

The planar double zig-zag configuration is one of the main objectives for the present thesis, because it is one of the most popular Coulomb crystals (CCs) realized in experimental setups [34, 105] and used in theoretical works [32, 33]. Some of the characteristics have been introduced already in chapter 5. Here, the dynamics for two zig-zag chains of equal size after the quench of the double well barrier will be discussed. Two initial zig-zag chain configurations can be prepared in the wells by applying a rotational symmetry in the coordinate origin (ground state: GS) (fig. 6.1(b)- right) or by applying a mirror operation on the radial axis through the barrier (mirror state: MS) (fig . 6.1(b)-left). These configurations are nearly degenerate with their potential energy differing only by 10^{-10}. Both configurations (GS and MS) are investigated here. The results of this chapter are published in [106] and the discussion follows the line of arguments there.

The initial configurations for the GS and the MS consist of 22 ions per well of the double well potential (fig. 6.1) and are characterized by the parameters $C_i = 1.26 \cdot 10^{-2}$, $z_0 = 3.97$ $\alpha = \omega_x/\omega_z = 8.3$ and $\beta = \omega_y/\omega_z > 10$.

The strong confinement in the y-direction prevents strong dynamics out of the x-z plane. The intra-plane oscillations are quadratically suppressed for increasing distance of the ions from the x-z plane.

The dynamics of the ions is started by a sudden quench of the barrier height between the wells, here exemplary from $C_i = 1.26 \cdot 10^{-2}$ to $C_f = 6.3$ (For an impression of the dynamic see movie [M.4]). The quench increases the coupling between the zig-zag chains[7] resulting in movement of the CCs closer to each other. The post-quench configurations are still two zig-zag chains separated by a now lower barrier and the energy excess of the quench is less than 2% in comparison with the initial system. In

[7] Before the quench (pre-quench) and after the quench (post-quench) the ion crystals in both wells are coupled by Coulomb forces (compare chap. 5)

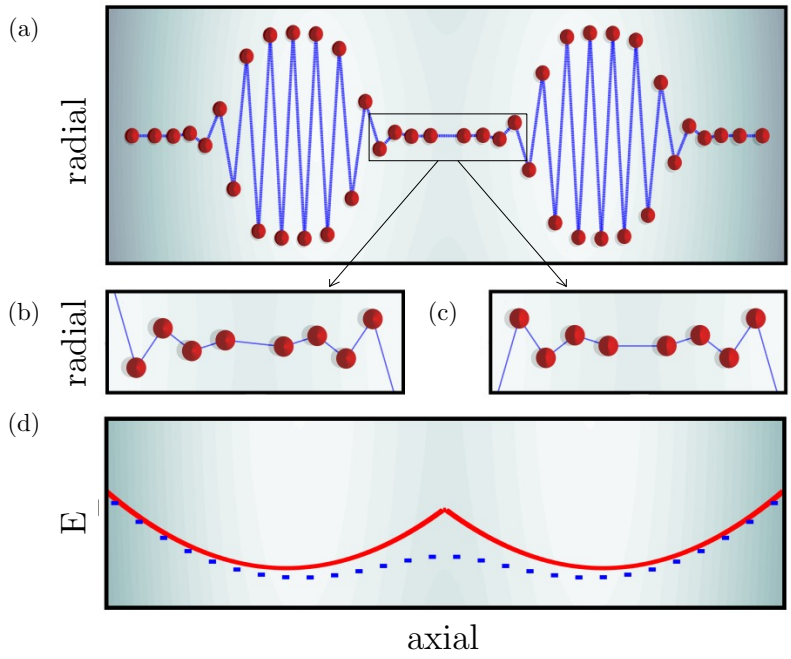

Figure 6.1: (a) The double zig-zag equilibrium configuration in the double well potential, calculated for $\alpha = 8.3$, $\beta > 10$, $z_0 = 3.97$ and $C = 1.26 \cdot 10^{-2}$. (b, c) Magnifications of the link between the two ion chains for (b) the GS and (c) the MS. (d) The red/blue line shows the double well potential before/after the quench. A lowered barrier enhances the coupling between the two ion chains [106].

the section 6.1 the post-quench dynamics of the ions is described and snapshots of the arrangement of the ions in the course of the dynamics are presented and discussed. To characterize these arrangements, the Voronoi measure is introduced in section 6.2 and the dynamics of the ions is compared to the time evolution of this measure. The transition of the dynamics in the basis of eigenvectors in section 6.3 is used to analyze the nonlinear dynamics.

6.1 Results

Before the quench the system is in the GS or the MS, respectively, and the ions oscillate slightly around their equilibrium position. By changing the potential barrier height, the new equilibrium state of the ions is no more congruent with the initial state, which induces dynamics as depicted in figure 6.2 and movie [M.4]. Up to $t \sim 1.5$ the dynamics of the CCs is dominated by the center-of-mass motion of both zig-zag structures towards each other (compare movie [M.4]). This collective motion is accompanied by

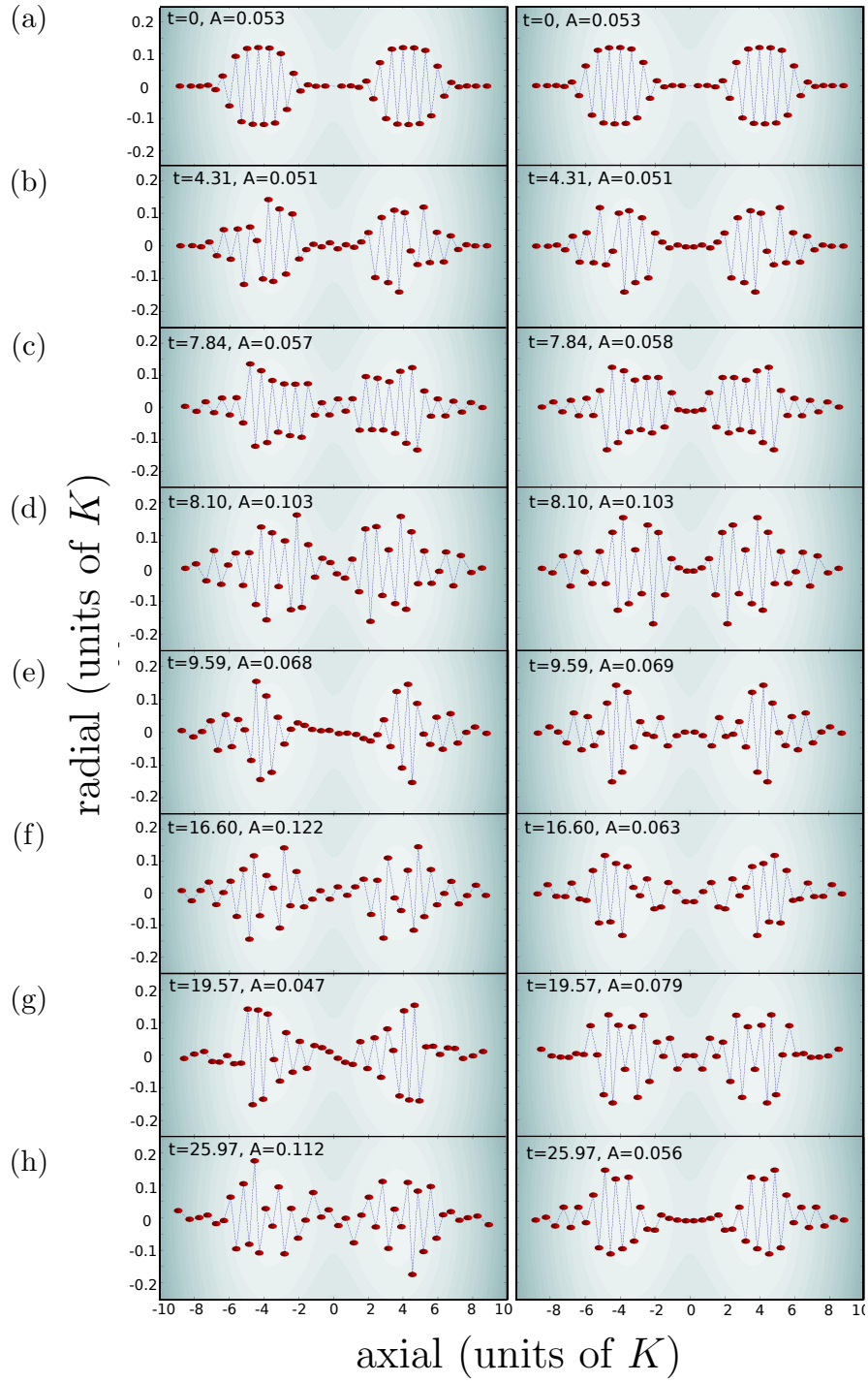

Figure 6.2: Snapshots of the time evolution of $N = 44$ ions in the double well for the ground state configuration (left column) and the mirror configuration (right column) as initial states. Parameters (in scaled units): $\alpha = 8.25; z_0 = 5/2^{1/3}$; C is changed from 0.0126 to 6.26 [106].

small oscillations of the individual ions. At $t \sim 1.5$ the two chains begin to rearrange at their boundaries close to the barrier, until the initial zig-zag order in radial direction is completely destroyed. The axial order of the ions is still conserved for the whole simulation. In radial direction, a reordering process is observed, which is characterized by phases having irregular ion oscillations alternating with phases featuring an unexpected degree of order. As depicted in the sequence of figures in 6.2 (a) -(h), the ions can form ordered structures such as lines, arcs and cross-like structures. Also partial revivals of configurations in the dynamics can be observed. The symmetries of the chosen initial configuration (rotational symmetry for the GS and mirror symmetry for the MS) is conserved in the course of the dynamics. The set of ordered structures for the different initial configurations can look similar (fig. 6.2(c)) or disparate (fig. 6.2(g)). For small times $t < 10$ the visual impression of structural order seems to be in a good agreement for both initial structures (fig. 6.2(a)-(e)). With increasing time the similarity in the order decreases.

To classify the degree of order for the structures shown in figure 6.2, they have to be quantified with a measure. In the next section such a measure based on Voronoi diagrams [48] is introduced to characterize the structure dynamics.

6.2 Voronoi measure

In crystallography, the lattice unit cell is an important tool to characterizes the periodic structure of a solid. For micro-structures with heterogeneous volume fractions, including concentrations and patterns such as clusters, the unit cell is not a proper tool to describe the arrangement of particles. Therefore, one often resorts to a method using Voronoi cells or Voronoi diagrams (eg. [48]). A Voronoi diagram partitions a given region into subsets based on the distance of each point in the region from the so called seeds (see fig. 6.3). Each subset assigned to a specific seed (Voronoi cell) constitutes a region consisting of all points closer to that seed than to any other. The Voronoi cells in the d-dimensional Euclidean space possess in general an arbitrary polyedric shape. Here, the minimum distance of the ions is of particular importance, hence a simple version of the Voronoi diagrams is employed. Around each ion a d-dimensional sphere is constructed, whose diameter is given by the distance to its nearest neighbor and the sum over all the spheres yields the Voronoi measure:

$$A(t) = \gamma \sum_i \left(\frac{r_{ij}(t)}{2} \right)^d \tag{6.1}$$

where r_{ij} is the distance of particle i from its nearest neighbor j. The dimensionality

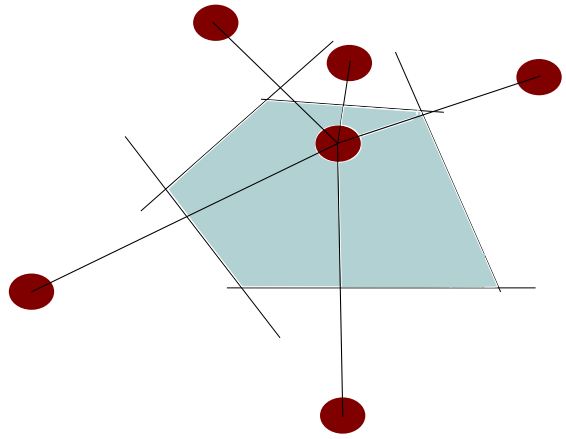

Figure 6.3: Schematic representation of a Voronoi cell (gray area) of a seed/particle (red circles).

of the configuration is given by the variables d and γ. For the zig-zag chain it yields $d = 2$ and $\gamma = \pi$, appropriate for a circular surface. For one dimensional configurations like the linear chain, $d = 1$, and $\gamma = 1$ and for a three dimensional problem like spherical configurations, $d = 3$ and $\gamma = 4\pi/3$. The Voronoi measure $A(t)$ (eq. 6.1) is a measure for the clustering of ions. Straight lines, arcs or crosses lead to low values, caused by the small distances between the ions in these structures. $A(t)$ would be also small for a macro-cluster of ions. In this work ion clustering is prevented by the chosen trap parameters. Larger values can be identified with a rather homogeneous distribution of the ions.

For the initial configuration of the double zig-zag chain, in both cases (GS and MS) the displacement in radial direction is much smaller than in axial direction. With the Voronoi measure (eq. 6.1) the axial extension dominates and the dynamics in the structure formation is lost. The average radial distance of adjacent ions is equated to their average distance in axial direction by rescaling the z-coordinates of all ions to $z^* = z \cdot k$ with $k = 0.04$.

In figures 6.4(a) and 6.4(b), $A(t)$ for the GS and the MS is shown, respectively. The labeled points correspond to the snapshots presented in figure 6.2. All structures which appear to be ordered from a visual impression and show ions arranged in arcs, lines or crosses (fig. 6.2), lead to distinct minima in $A(t)$. Irregular structures (fig. 6.2 (d) left and right, (f) left, and (g) right) generate larger values for $A(t)$.

The dynamics of $A(t)$ for the GS (fig. 6.4(a)) and for the MS (fig. 6.4(b)) as initial configuration are similar for small times $t < 10$. Hence, the alternating process generating ordered and disordered structures follows the same sequence. For larger times the difference in the Voronoi measure increases. The very small difference in the distances between the ions in the initial state change the complete course of the structure dynam-

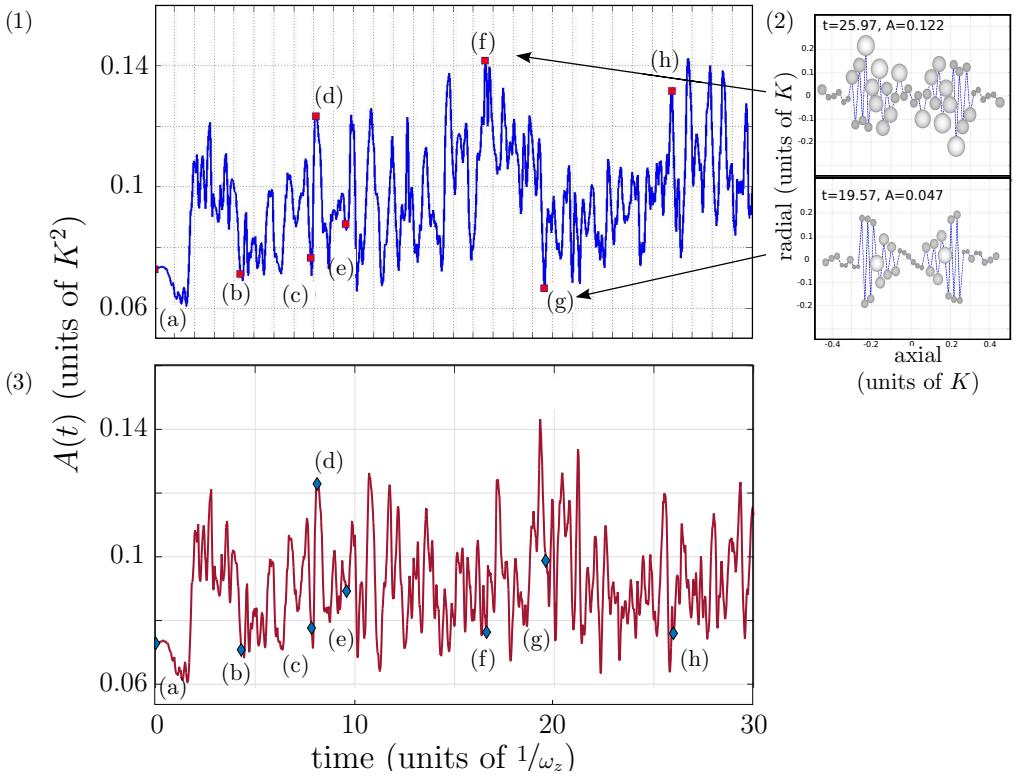

Figure 6.4: Time evolution of the Voronoi measure $A(t)$ as defined in equation 6.1 for (1) GS and (3) MS as initial configuration. Red squares show times at which snapshots in fig. 2 were taken for the ground configuration (left column) and blue diamonds for the mirror configuration (right column). (2) Insets illustrate the definition of $A(t)$ as the sum of the areas of all shown circles. Upper and lower insets illustrate how $A(t)$ accounts for typical irregular and regular configurations respectively [106].

ics. This is visible in the time evolution of $A(t)$ (see fig. 6.4) as well as in the sequence of structures (fig. 6.2). The Voronoi measure is a suited tool to classify the emergence of ordered ion structures originating from the double zig-zag structures. To visualize the ensemble motion of the ions a normal mode analysis is used.

6.3 Normal mode analysis

For a small quench of the barrier, the dynamics can be approximated by linearized equations of motion. The dynamics is then governed a superposition of harmonic oscillations in terms of normal modes [107] with constant oscillation amplitudes. The perturbation induced by the chosen quench is beyond the linear dynamics. The crystal structure is destroyed, but revivals and the oscillation between order and disorder imply a nonlinear

regime which is not so far away from the linear one. It is possible to chose an arbitrary basis to interpret the dynamics and it turns out that the linear modes are still useful. In the nonlinear regime generally different normal modes are generally coupled and energy transfer between them results in variation of normal mode amplitudes.

The eigenvectors $\mathbf{E}_i$ of the post-quench equilibrium configuration are numerically calculated by diagonalizing the Hesse matrix of the system. These eigenvectors form a basis of the N-dimensional configuration space (sorted by their eigenfrequencies). The position of each ion at a fixed time t in this basis is:

$$(\mathbf{r}_1, .., \mathbf{r}_N)(t) = \left(\mathbf{r}_1^{\mathrm{eq}}, .., \mathbf{r}_N^{\mathrm{eq}}\right) + \sum_i p_i(t)\mathbf{E}_i; \tag{6.2}$$

Here, $\mathbf{r}_m^{\mathrm{eq}}$ is the position of the m-th ion in the post-quench GS/MS configuration and $p_i(t)$ describe the population of the linear eigenvectors $\mathbf{E}_i$. In the linear regime the population coefficients reduce to $p_i(t) = P_i \cos(\omega_i \cdot t)$ with P_i being constant amplitude.

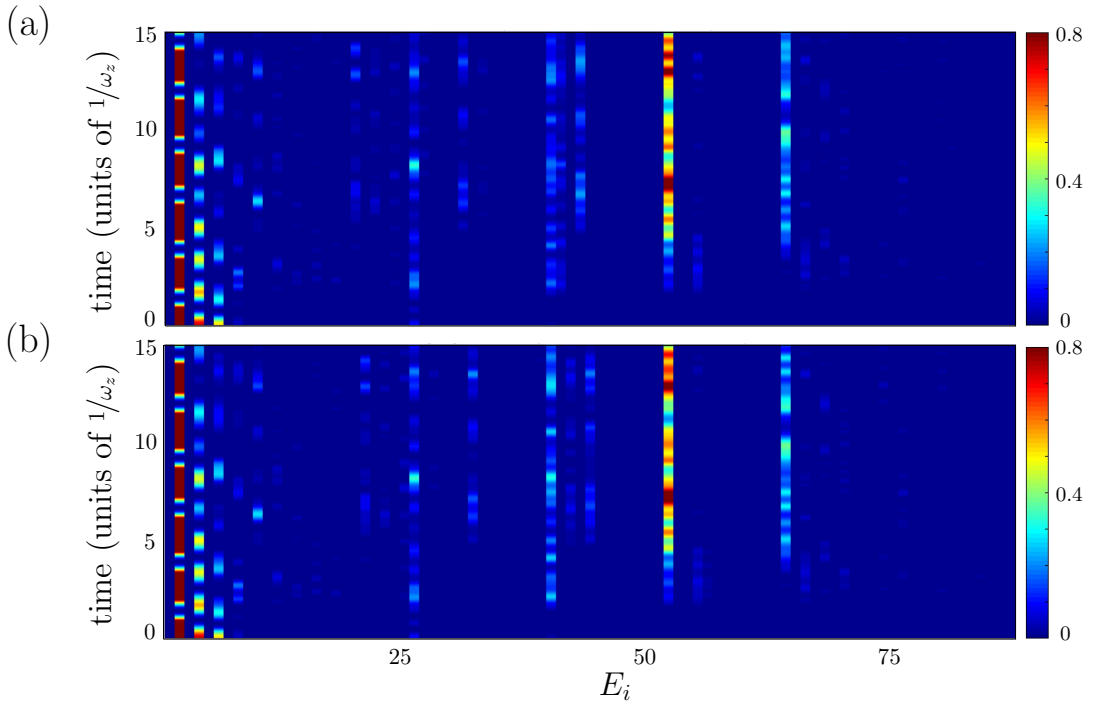

Figure 6.5: Time evolution of the eigenvectors contributions $p_i^2(t) = (d_i(t)\cos(\omega_i t))^2$ (color) for (a) the ground state [106] and (b) the mirror state.

The population dynamics of the eigenvectors $\mathbf{E}_i$ as induced by nonlinear effects is shown for the GS and MS in figures 6.5 (a) and (b). The population dynamics of both

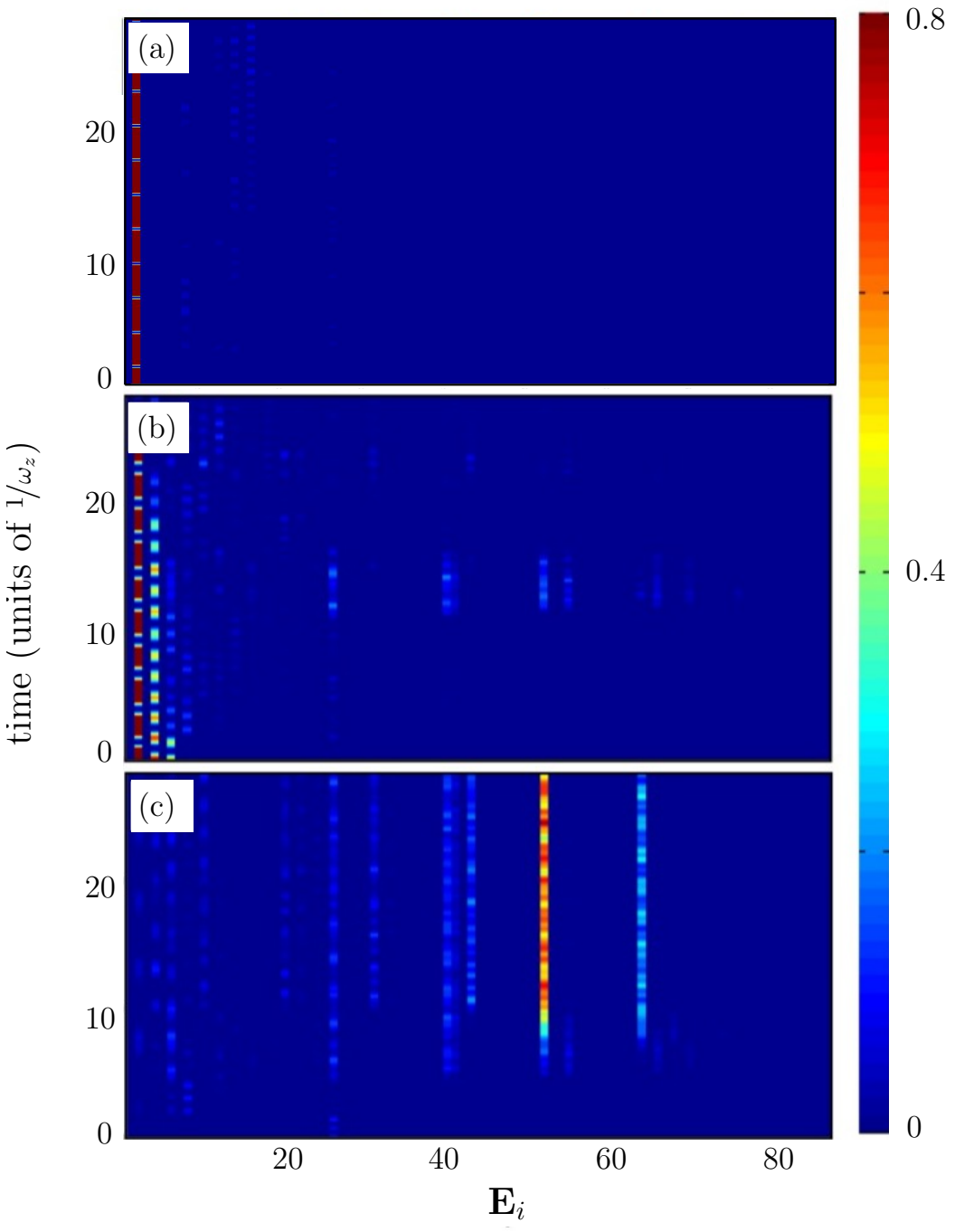

Figure 6.6: Time-dependent population of linear eigenvectors defined as $p_i^2(t) = (d_i(t)\cos(\omega_i t))^2$ (color) for different initial populations of the eigenvectors: (a) for the ground state configuration as initial configuration with setting all but the population p_2 to zero. (b) as in (a) but after setting all but the three largest initial populations (p_2, p_4, p_6) to zero. (c) Population of only one mode with $p_{26}(t = 0) = 0.11524$. Parameters as for figure 6.2 [106].

configurations are similar and therefore the analysis is done for the GS exemplarily. The population dynamics of the MS shows a similar behavior with respect to the mirror symmetry of the system. The initial quench mainly populates the vectors $\mathbf{E}_2, \mathbf{E}_4, \mathbf{E}_6$ (fig. 6.5 (a) at $t = 0$). These belong to the slowest modes whose population is allowed by symmetry parity. Figure (6.5 (a) shows that at $t \sim 1.5$ a first significant energy transfer to higher modes takes place, which is the time where the zig-zag configurations start to rearrange, and then spreads more and more to other modes. Notably, the energy does not spread in an arbitrary manner over a whole band of modes as expected for a purely irregular or strongly chaotic system, but rather many of the eigenvectors either keep their population for longer time periods or exchange them only pairwise (fig. 6.7) (compare [108] for mode coupling within kinked crystal). This indicates that the dynamics of the

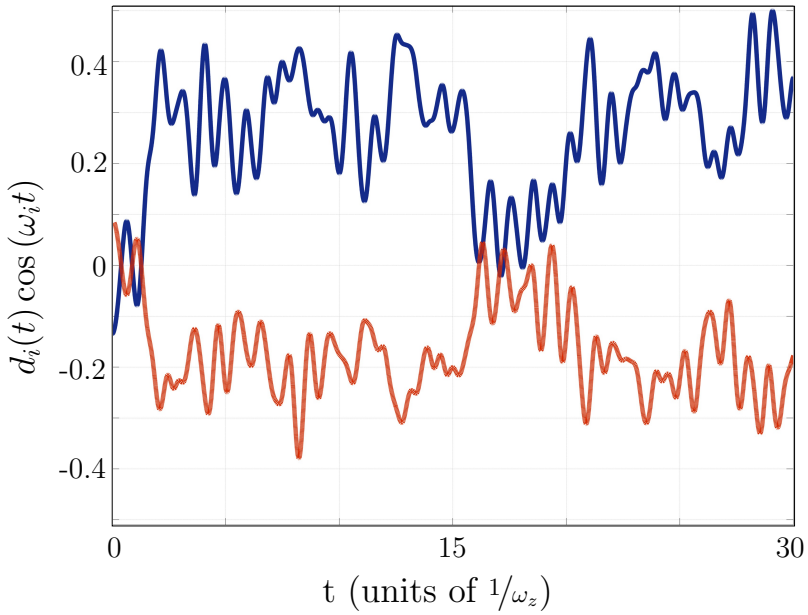

Figure 6.7: Magnification of the population dynamics of $d_{40}(t)\cos(\omega_{40}t)$ and $d_{41}(t)\cos(\omega_{41}t)$ as defined in equation 6.2 for the GS as intial state.

ions is not irregular but possesses a high degree of order. The population transfer, which takes place between individual linear normal modes, will be studied in the following. To study the effects induced by the population of specific eigenvectors, one excludes the remaining modes from the dynamics and only one (or several) of the linear eigenvectors is populated and the resulting dynamics is explored. Thus, the contribution of $\mathbf{E}_2$ (see fig. 6.6 (a)) which has the largest population after the quench, leads to a permanent 'breathing' oscillation of all ions in the left well and an opposite motion of the ions in the right well. Accordingly, almost no transfer of population to other eigenvectors

can be observed and the considered single mode excitation leads to persistent small and periodic oscillations rather than inducing a reordering of the double zig-zag. Populating, e.g., the three eigenvectors ($\mathbf{E}_2$, $\mathbf{E}_4$ and $\mathbf{E}_6$), which attract the strongest population, leads to similar results: Only a small amount of energy is transferred to other modes (fig. 6.6 (b)). There are, however, eigenvectors belonging to higher modes, whose initial population, even if it is small, induces a hierarchical spreading of population between different eigenvectors. In particular, a weakly populated vector $\mathbf{E}_{26}$ above $p_{26}(t = 0)$ results in population dynamics which reproduces large parts of the occupation dynamics as induced by the full problem (fig. 6.6(c)). Already a weak population of this vector does therefore lead to significant nonlinear effects strongly mixing the linear eigenvectors. As a result, it depends on the population of the eigenvectors whether the system responds with small oscillations or with a complete loss of order in radial direction and the dynamical reconfiguration of the ions into ordered (transient) structures.

6.4 Conclusions

Depending on the details of the excitation, the symmetric Coulomb crystal configurations show a rich variation of dynamics. Regular oscillations around the equilibrium configuration or a complete loss of order in radial direction followed by a sequence of structures with ions arranged in lines, arcs and cross-like formations can be obtained. The Voronoi measure (eq. 6.1) proves to be a suitable measure to characterize the structure/formation dynamics. With the aid of eigenvector analysis, the linearity of the dynamics can be evaluated. The presented case is in the nonlinear regime. The breathing mode (eigenvalue E_2) dominates the dynamics, but the emergence of the obtained complex formation bases on the coupling of some of the eigenvectors due to the non-linearity of the dynamics.

CHAPTER 7

Ion transfer among Coulomb crystals in a double-well potential

In the last chapter the rotational and mirror symmetric zig-zag chain configurations of the double well potential have been analyzed. When the wells are symmetrically populated, a quench in the barrier height results in symmetric dynamics of the ions in the wells prohibiting mass and energy transport. In order to observe mass and energy transfer, the symmetry of the initial configuration needs to be broken. Such an asymmetric initial configuration can be achieved by displacing an ion far away from its equilibrium position or by an imbalance of the number of ions per well. The dynamics will be triggered by a quench of the barrier height[8]. The results from this studies have been published in [109] and the discussion in this chapter follows from this publication.

7.1 Transfer dynamics

From the vast number of asymmetric distributions of ions in both wells, four prominent ordered structures have been chosen (fig. 7.1): (a) the linear chain, (b) the already known zig-zag configuration from chapters 5 and 6, (c) a ring structure in two dimension and (d) a three dimensional shell structure. As stated above, the dynamics of the system is initiated by a sudden quench of the barrier height between the two wells which is characterized by the parameter C, i.e. a quench of the axial potential V_d from $C = C_i$ to $C = C_f$. The following non-equilibrium dynamics of the CCs including mass and energy transfer between the Coulomb crystals (CCs) is therefore studied as a function of C_f. Due to the excess of energy resulting from the quench of the barrier height, the ions constituting the Coulomb crystals are set in motion.
Their dynamics is complex, involving among others a rather regular center of mass (CM) motion of the crystals, shock waves, multiple scattering processes and transfer of ions over the barrier caused by the asymmetric population of the two potential wells.

[8]For an impression of the ion dynamics see movies [M.5–M.7]

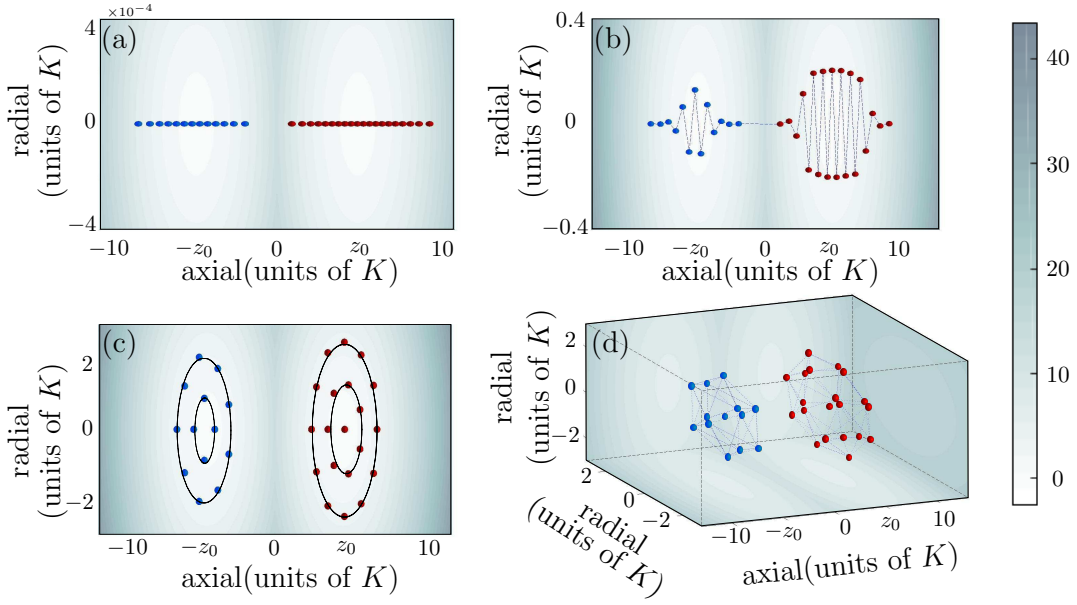

Figure 7.1: Initial ion ground state configurations for different potential parameters: (a) linear chains for $\alpha = 100, \beta = 100$, (b) zig-zag chains for $\alpha = 5.6, \beta = 8$, (c) circles for $\alpha = 1, \beta = 8$, and (d) spheres for $\alpha = 1, \beta = 1$. The background of the figures encodes the values of the corresponding trapping potential. All configurations and their dynamics are calculated in three dimensions with their dimensionality being restricted only by the frequency ratios α and β [109].

Especially rotations and reordering of the crystals can be observed for the cases of the circular and spherical GS configurations.
The ion transfer process between the two potential wells is analyzed first and then its effects on the structure of the two Coulomb crystals is discussed.

7.1.1 Ion transfer

Among the features characterizing the ion transfer following a quench of the barrier height, two aspects are particularly of interest: the time instant at which an arbitrary ion passes above the barrier for the first time (t_{first}) and how often each ion in the Coulomb crystal travels back and forth between the two wells.

The results for the time t_{first} of an arbitrary ion leaving the large crystal as a function of the final quench value C_f are presented in figure 7.2 for the different trapping geometries depicted in figure 7.1. For simplicity only the first four traveling ions are shown. For all cases two qualitatively different regions can be distinguished. The first one – occupying the upper part of the plots in figures 7.2 (a)-(d) (large times $t_{\text{first}} > 10$)- shows a step-like behavior (with varying C_f) consisting of several smooth regions separated by gaps, whereas the lower part (small times $t_{\text{first}} < 10$) exhibits a continuous behavior.

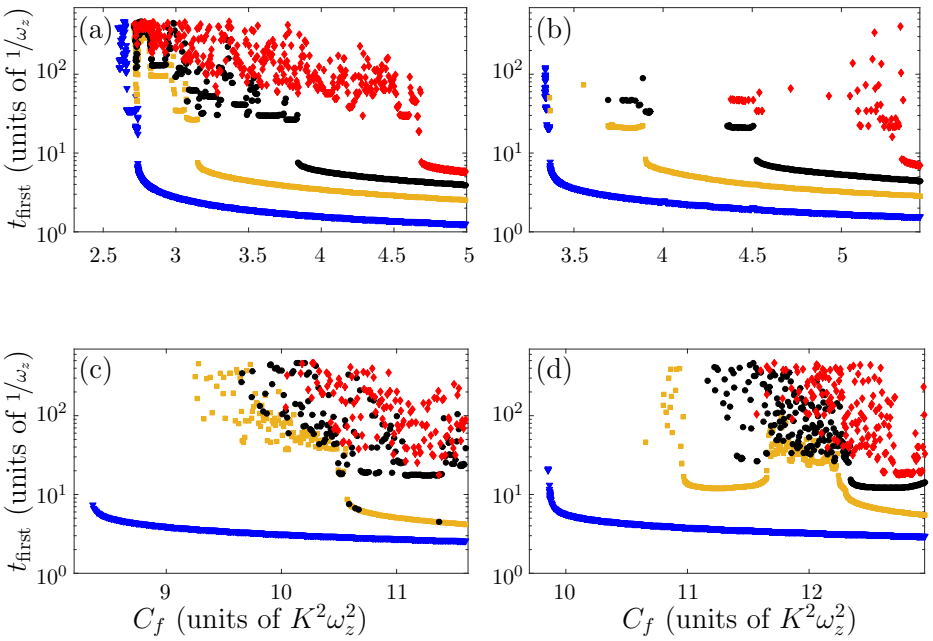

Figure 7.2: Time instant of the first transfer (t_{first}) of the first four traveling ions (order: first- blue triangle, second- yellow squares, third- black dots, fourth- red diamonds) as a function of C_f for (a) linear chains, (b) zig-zag chains, (c) circles, and (d) spheres. For smaller C_f values than the ones depicted in the figures there is no ion transfer as explicitly shown in (a).

The value of C_f governs the number of ions that can be transferred. Each individual ion transfer follow the same qualitative behavior with respect to its time scale. For small quench amplitudes and subsequently large times t_{first} the time instant of the first transfer of each ion has a step-like character, whereas beyond a certain quench amplitude it continuously decreases as a function of the final value C_f.

Without loss of generality, the focus is on the zig-zag configuration (fig. 7.2(b)) as a characteristic example of this behavior, and only the transfer of the first ion (fig. 7.3) is considered in the remaining part of this subsection. A necessary condition for the transfer of an ion above the barrier is obviously that this ion is close to the barrier. Of all the ions of the CCs, the ion closest to the barrier of the CC will be the most probable candidate for an initial ion transfer. This is referred to as the innermost ion and its transfer dynamics is analyzed. Such an analysis can be facilitated by examining a case in which ion transfer, although energetically possible does not occur. This corresponds to a quench value inside a gap in the graph of figure 7.3. which can be fulfilled by choosing, for e.g. a value of $C_f = 3.3403$, thereby allowing an analysis of the long-time dynamics of the innermost ion without interruptions by the ion transfer processes. The time evolution of the axial position of the innermost ion of the large crystal, as well as

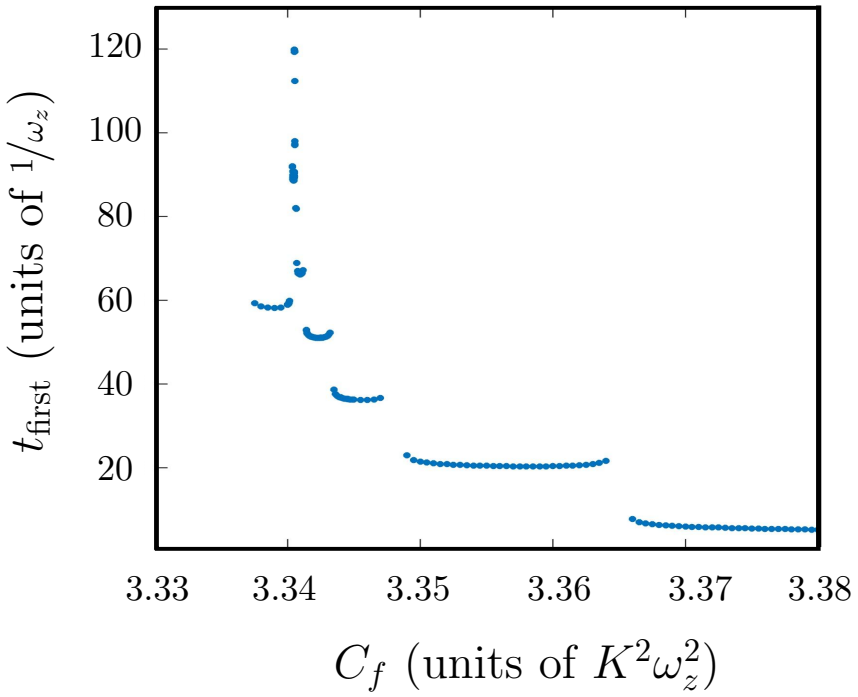

Figure 7.3: Time instant of the first transfer of the first traveling ion as a function of C_f for the case of the zig-zag chain (zoom of fig. 7.2(b))

its Fourier spectrum for $C_f = 3.3403$ are shown in figure 7.4. The motion appears to be oscillatory and quite regular with a single dominant frequency. This is supported also by the Fourier spectrum which essentially shows the contribution of three frequencies with one frequency (largest amplitude) being dominant. In order to find out whether this frequency is generic for this system, the Fourier spectra of the innermost ion motion for four different values of C_f, which do not lead to transfer (fig. 7.5), are investigated.

Obviously, in all cases there is one predominant frequency in the range of $\omega \approx 0.84$ to 0.88, corresponding to a period T ranging approximately between 7.1 and 7.4. A comparison of this period with the time t_{first} in figure 7.3 leads to the conclusion that the latter is equal to one or two times the period T (fig. 7.6) within a range of 3.5%. This explains the existence of the steps in the ion transfer process as a direct consequence of a preferred oscillation phase (closest to the barrier) of the innermost ion. What remains to be answered is why not every time separation equal to the period T leads to transfer and why some time separations between the steps are twice the period T, i.e. why some steps are absent. To provide an answer to this question, it is essential to take into account also the dynamics of the other ions in the Coulomb crystals.

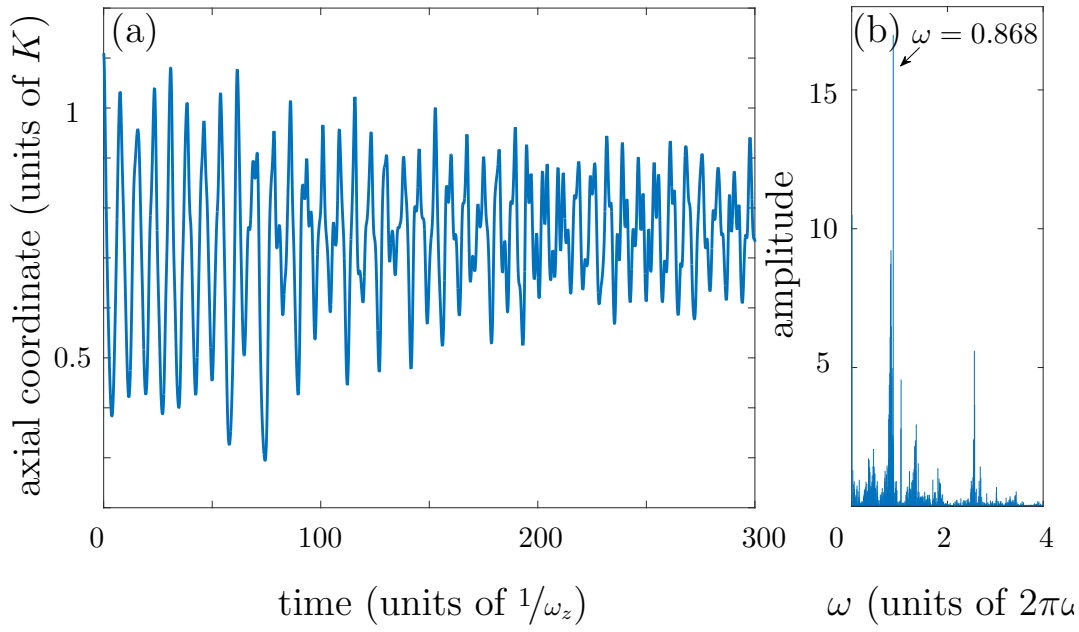

Figure 7.4: (a) The axial motion of the innermost ion of the zig zag configuration and (b) its Fourier spectrum for $C_f = 3.3403$

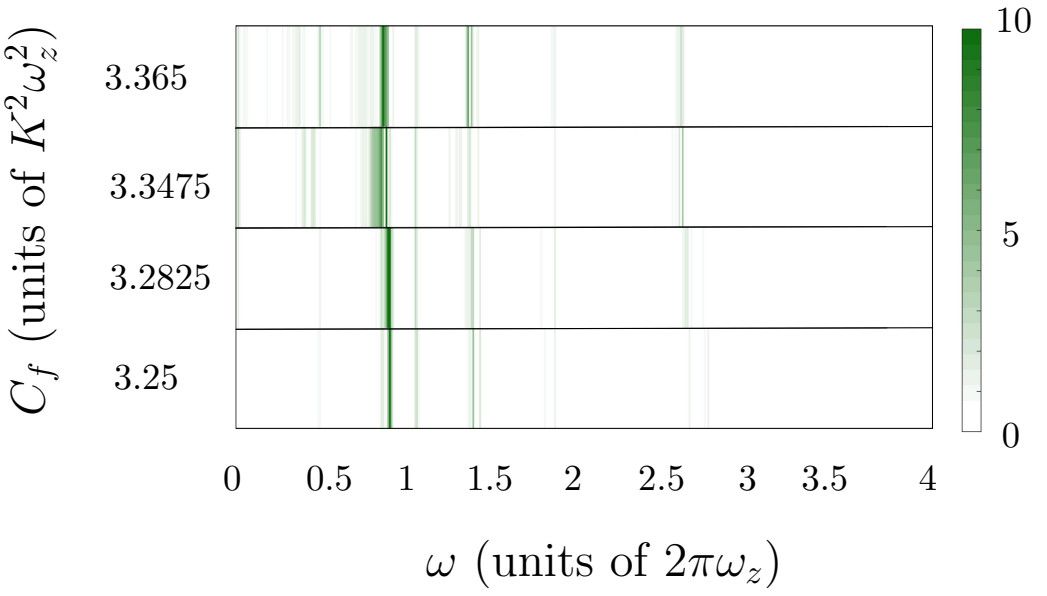

Figure 7.5: Comparison of the Fourier spectra of the innermost ion motion for 4 different values of C_f. The color depicts their amplitude.

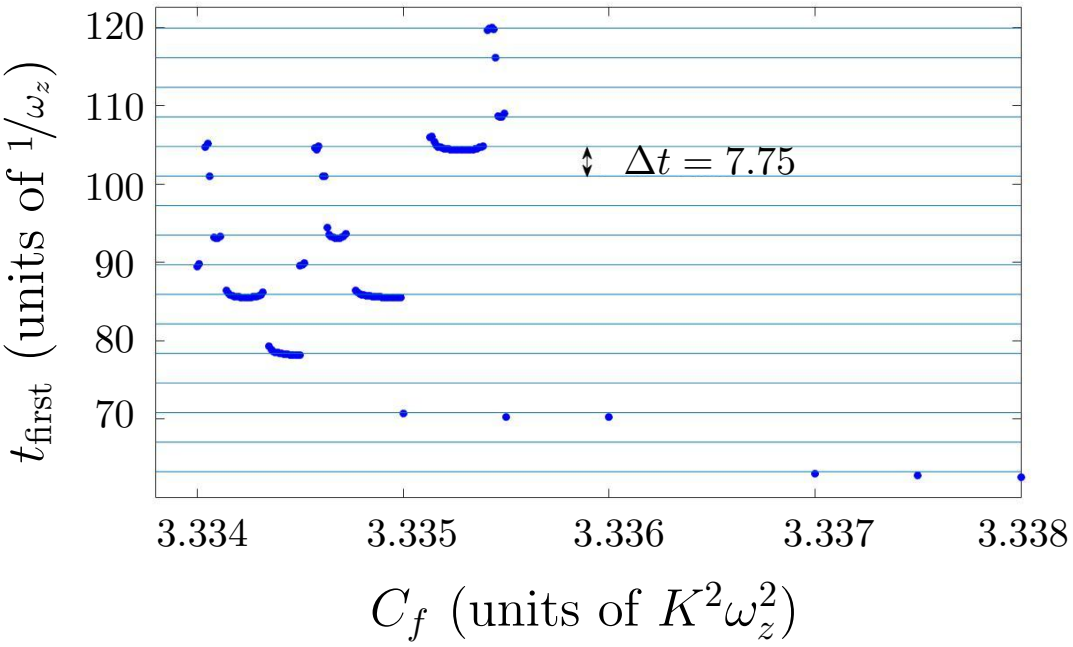

Figure 7.6: The time instant for the first transfer of the innermost ion as a function of C_f for the zig-zag configuration (zoom of fig. 7.3 with smaller stepsize of the scan). The horizontal lines mark the multiples of the period T of the innermost ion.

Following the quench, all ions constituting the two Coulomb crystals move collectively towards the barrier, as can be seen by inspecting their CM motion (fig. 7.7 (a)). Since the two crystals interact via repulsive Coulomb forces, the repulsion exerted by the small crystal hinders the transfer of the innermost ion of the large crystal. If the energy introduced by the quench is high enough to overcome the Coulomb interaction and the barrier, the innermost ion travels to the other well. Otherwise the two crystals start to oscillate without any ion transfer, as depicted in their CM dynamics (fig. 7.7 (a)). The Fourier analysis of this CM motion shows that the frequencies of the left and right crystal differ (fig. 7.7 (b)) due to their different sizes. Therefore, there is a variety of possibilities for the position of the CM of the both crystals during the time evolution (see fig. 7.7(a)): (i) they can both be close to the barrier (line A in fig. 7.7(a)), (ii) both can be far away from the barrier (line B in fig. 7.7(a)), (iii) the large crystal can be close to the barrier and the small far away (line C in fig. 7.7(a)) or (iv) vice-versa of (iii) (line D in fig. 7.7(a)). Obviously, case C is optimal for the transfer. The two CM frequencies depend on the value of the barrier height, thus the time instant when the optimal conditions are fulfilled changes slightly with C_f. This leads to different time scales for ion transfer which appears as different steps in figure 7.6. Depending on C_f

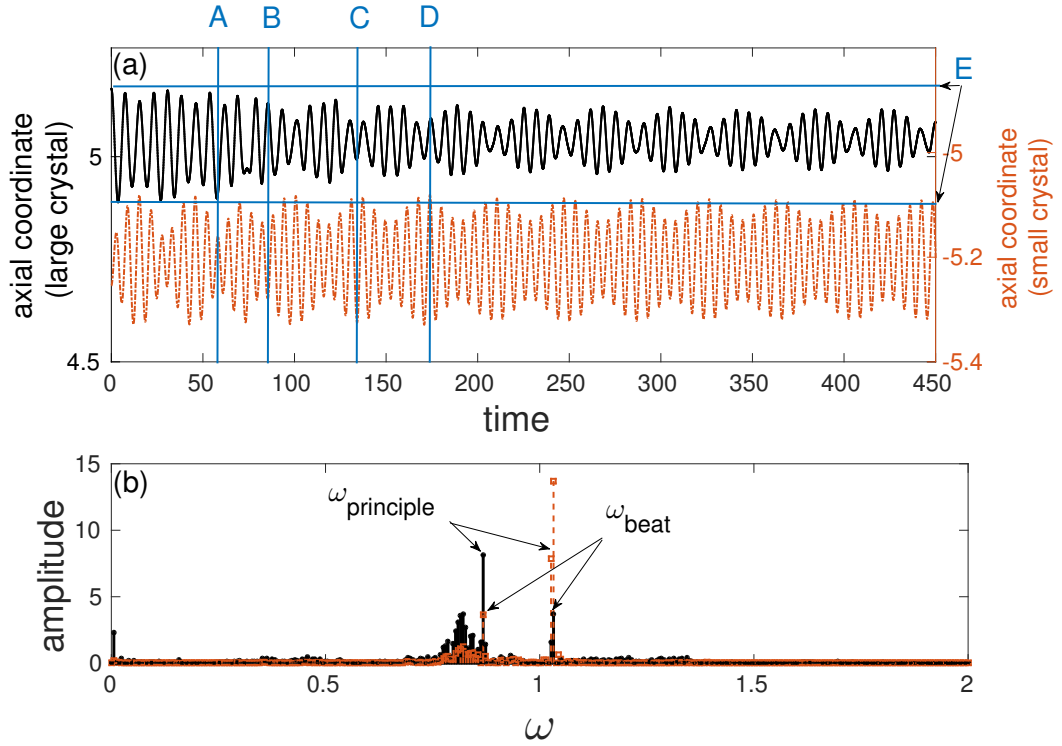

Figure 7.7: (a) CM motion of the two crystals (large crystal solid black line and small crystal red dashed line) for the zig-zag configuration with $C_f = 3.3403$. The vertical lines A,B,C,D mark the time instants during the dynamics corresponding to qualitatively different positions of the two Coulomb crystals. The horizontal line E denote the initial amplitudes of the CM motion of the large crystal. (b) The corresponding Fourier spectra for the large (black- $\omega_p = 0.868$ and $\omega_b = 1.0264$) and the small crystal (dashed red with squares- $\omega_p \approx 1.0323$ and $\omega_b \approx 0.868$).

it is possible, that the innermost ion is close to the barrier when the CM of the larger crystal is not and thus due to the lack of energy the ion transfer is prohibited. This leads to some steps being suppressed. The subsequent steps appear after a time $2T$ (fig. 7.6). Apart from the main frequencies ω_p for the two crystals, additional beating frequencies ω_b (fig. 7.7(b)) can be observed as well. As a consequence, the amplitude is modulated (see fig. 7.7 (a)) which also influences the transfer dynamics. The pairs of ω_p, ω_b frequencies for the small and the large crystal are approximately degenerate, a fact that can be attributed to their Coulomb coupling.

Another feature of the CM dynamics is the damping of the oscillations of the big crystal within time (fig. 7.7(a) line E), thereby limiting the time available for ion transfer and giving rise to the observed gaps of figures 7.2 and 7.3. The origins of this damping are the repulsive interactions between the two crystals, the transfer of energy in the radial directions, especially along the least confinement, and the mode coupling between the CM modes and other modes due to the inherent nonlinearity of the system.

On the other hand, if the energy introduced by the quench is large enough, the dynamics of the CM motion cease to rule the transfer process of an ion, resulting in a smooth behavior of the time t_{first} as a function of C_f (fig. 7.2 the lowest stairs in the transfer dynamics).

So far the focus of the discussion has been on the first time instant at which an ion is transferred from one well to the other. But an ion can travel back and forth thereby crossing the potential barrier several times. To extract information on the number of transfers per ion, the ions are sorted in their initial configuration according to their positions in the axial direction in increasing order and for each state the number of transfers occurring during the course of the dynamical evolution was counted . Accordingly, the first 13 ions are in the small and the next 20 in the big crystal at $t = 0$. In figure 7.8 the results for the different initial configurations (fig. 7.1) are shown. For the

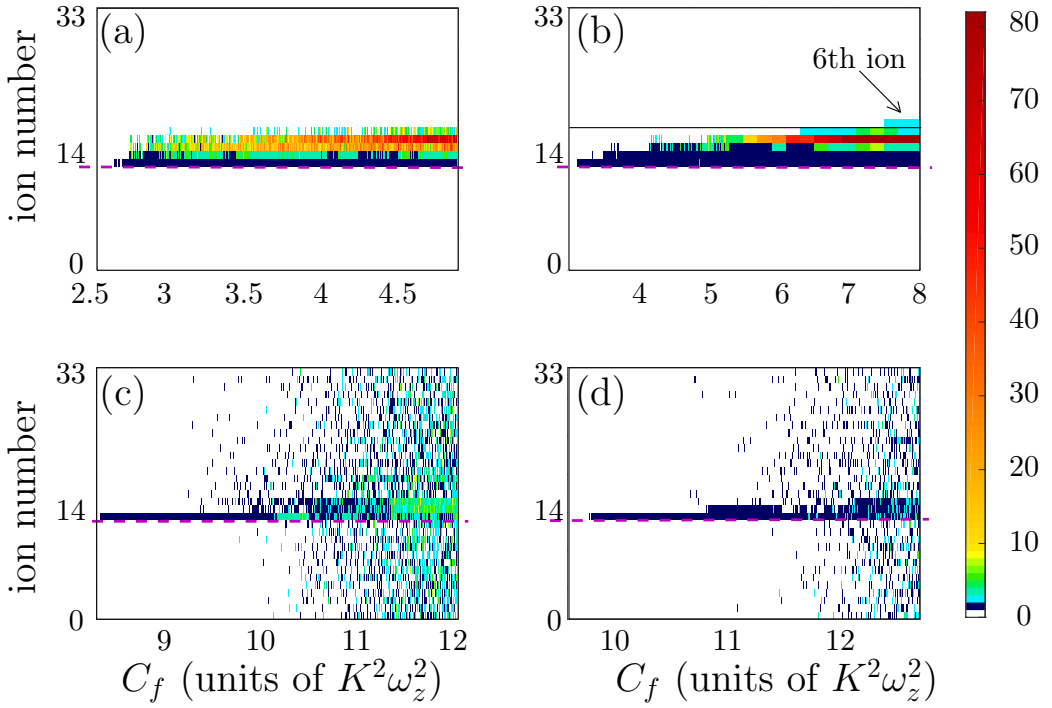

Figure 7.8: Number of transfers per ion as a function of C_f for (a) linear chains (b) zig-zag chains (c) circles (d) spheres. The (pink) dashed line separates the ions of the small from the ions of the large crystal.

linear and the zig-zag configurations (the considered region of C_f in figure 7.2) only five ions travel (compare figs. 7.8(a) and (b) for $C_f < 6$) . These are the ions which are located in the big crystal closest to the barrier (ion numbers 14 to 19). These 5 ions

travel forth and back over the barrier several times during the simulation time, whereas none of the other ions in the two crystals ever crosses the barrier (fig. 7.8 (a), (b)). The reason for this is the strict confinement in the radial direction for these two cases which is especially true for the linear chains. For the zig-zag chain, as long as the order of the ions in the axial direction is preserved, the exclusive transfer of only 5 ions is observed. But for larger values of $C_f > 6.5$, (where the strict axial order is destroyed) other ions cross the barrier. (compare fig. 7.8 (b)).

In contrast to the above to cases, for the cases of the circle and sphere configurations (fig. 7.8 (c), (d)) all ions can be transferred. Because of the low frequency aspect ratios ($\alpha = 1$) of the radial confining potentials, these configurations enable rotations of the whole crystal as well as rearrangements with respect to the order of the ions. Thus, in the course of the dynamics, the order of the ions in the axial direction changes for larger C_f as a nearly uniform distribution of the number of transfers among the ions of the two crystals. The ion transfer processes affect the order and the structure of the involved CCs. This is analyzed in the next subsection.

7.1.2 Crystalline order

The ion transfer processes discussed above yield complex non-equilibrium dynamics of the two resulting Coulomb crystals involving alternating disordered and re-ordered phases. In order to characterize and analyze the ordering of the resulting crystals, the Voronoi measure introduced in chapter 6 is used. The time evolution of this measure has been proven to capture well the change in the crystalline order of Coulomb crystals during dynamics [106]. In contrast to chapter 6 the two Coulomb crystals have different sizes causing them to behave differently. Therefore, for each crystal located in a certain well, its Voronoi measure is determined, taking as well into account that the number of ions per well (crystal) changes in time due to the ion transfer processes. The Voronoi measure is redefined as:

$$\Omega(t) = \gamma \frac{1}{N} \sum_i \left(\frac{r_{ij}(t)}{2} \right)^d \tag{7.1}$$

where N is the number of ions in the well and r_{ij} is the distance of each ion i from its nearest neighbor j.

In the course of the dynamics, the system of ions alternates between clustered and dispersed phases resulting in an alternating Voronoi measure. The clustered structures, which at first glance give the impression of an ordered phase, lead to low values of the Voronoi measure, whereas a scattered distribution of the ions leads to larger values of $\Omega(t)$ [106].

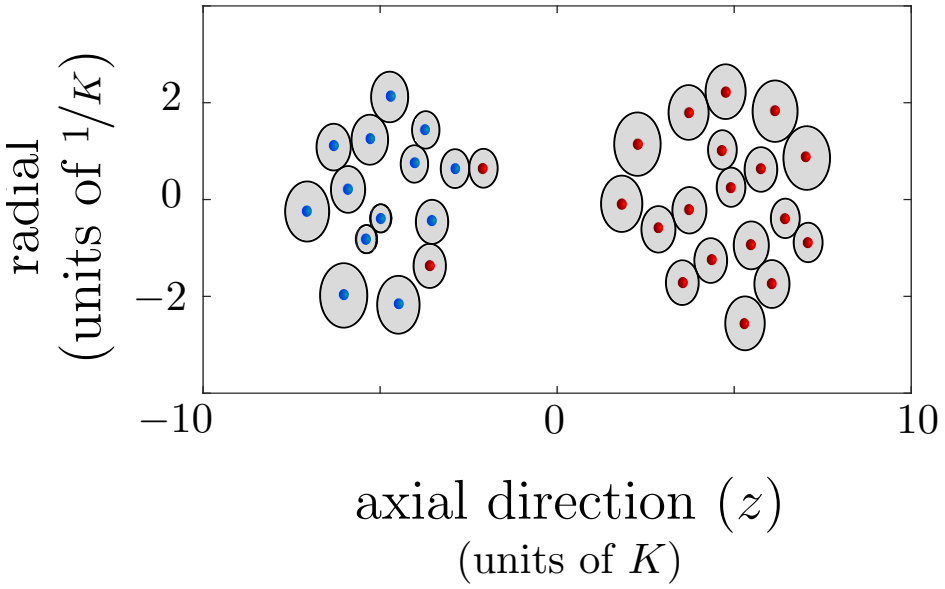

Figure 7.9: Snapshot of the two Coulomb crystals (small blue dots, large red dots) and the respective Voronoi spheres (gray circles) used to calculate the Voronoi measure. Here the trapping parameters are chosen so that the two crystals self-organize in circular shells (see fig. 7.1 (c)). The snapshots correspond to a value $\Omega = 2.85$ for the small and $\Omega = 3.35$ for the larger crystal.

An example of the time evolution of the Voronoi measure $\Omega(t)$ after the quench of the barrier height is shown in figure 7.10 (a) for the zig-zag Coulomb crystals (fig. 7.1 (b)) for the final quench value $C_f = 3.34$, for which a single ion is transfered at $t \approx 59$ (figs. 7.2 (b) and 7.3). For comparison, the time evolution of the axial coordinate of the traveling ion is presented in figure 7.10 (b). Initially (i.e. before the ion transfer) one can observe that the Voronoi measure exhibits regular oscillations with a much larger amplitude for the large crystal compared to the smaller one. This can be attributed to the larger shell diameter of the former which allows for larger deformations (i.e. compressions and expansions).

At the time instant when the ion crosses the barrier (fig. 7.10 (b)), the Voronoi values of both the large and the small crystal exhibit a prominent peak (fig. 7.10 (a)). This results from the change in the number of ions per crystal and the fact that the distance of the traveling ion from its nearest neighbors is maximum when it crosses the barrier. After the ion transfer, the Voronoi measure of the small crystal performs highly irregular oscillations with an increased amplitude, relating to the irregular and disordered dynamics of the ions constituting the crystal (crystal melting). In contrast, the oscillation amplitude of the Voronoi measure for the large crystal decreases slightly after the ion transfer due to the increase in the available space for the ion dynamics and

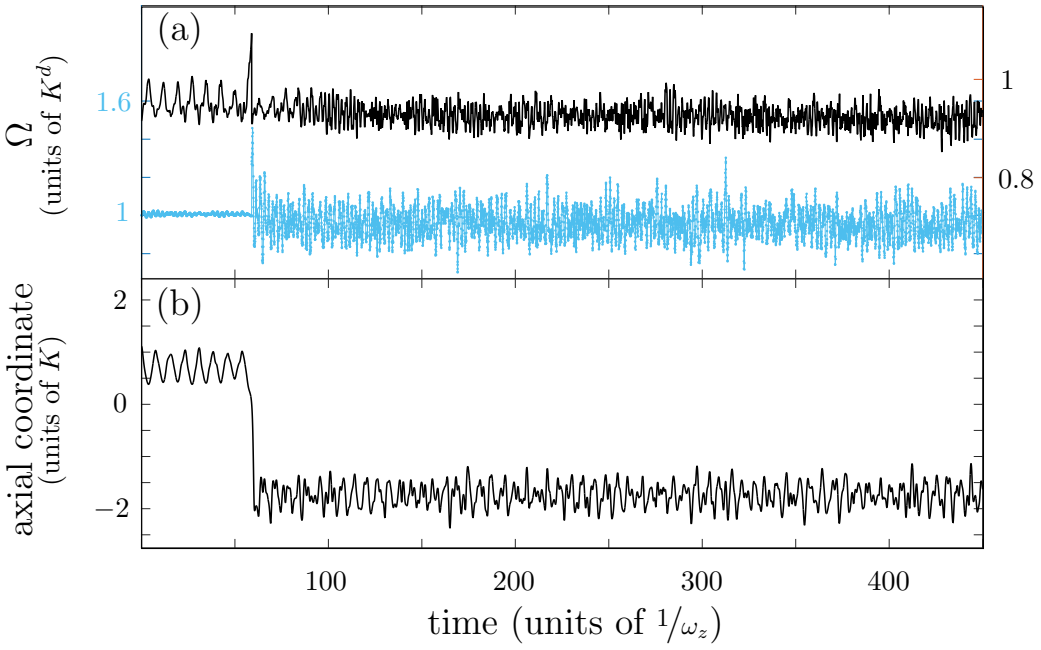

Figure 7.10: The time evolution of (a) the Voronoi measure (Ω) of the two ion crystals (large ion crystal- black and small ion crystal- light blue) and (b) the axial position of the innermost ion for the zig-zag configuration and $C_f = 3.34$

the substantial loss of energy caused by the loss of the highly energetic traveling ion. Similar to the case of the smaller crystal the oscillations after the transfer become more irregular involving multiple frequencies.

These results suggest that the Voronoi measure $\Omega(t)$ and especially its oscillation amplitude encapsulates substantial information on the out-of-equilibrium many-body ion dynamics following the quench of the barrier height. Nevertheless, in order to analyze the crystalline order as a function of the final quench parameter C_f, it would be useful to characterize each time series by a single value. A measure related closely to the average oscillation amplitude of $\Omega(t)$ (i.e. capturing well the average dynamics of the crystals) is its standard deviation $\Delta\Omega$ in time. An increase of $\Delta\Omega$ is accompanied by an increase of the fluctuations in the Voronoi measure $\Omega(t)$, i.e. the ion structures alternate strongly between the clustered and dispersed orientations.

The resulting values for the standard deviations $\Delta\Omega$ as a function of C_f are shown in figure 7.11 for the different trapping potentials examined (fig. 7.1). The standard deviation $\Delta\Omega$ for the one (fig. 7.11 (a)) and two-dimensional (figs. 7.11 (b),(c)) ion configurations are highly irregular but for the three-dimensional configuration (fig. 7.11 (d))

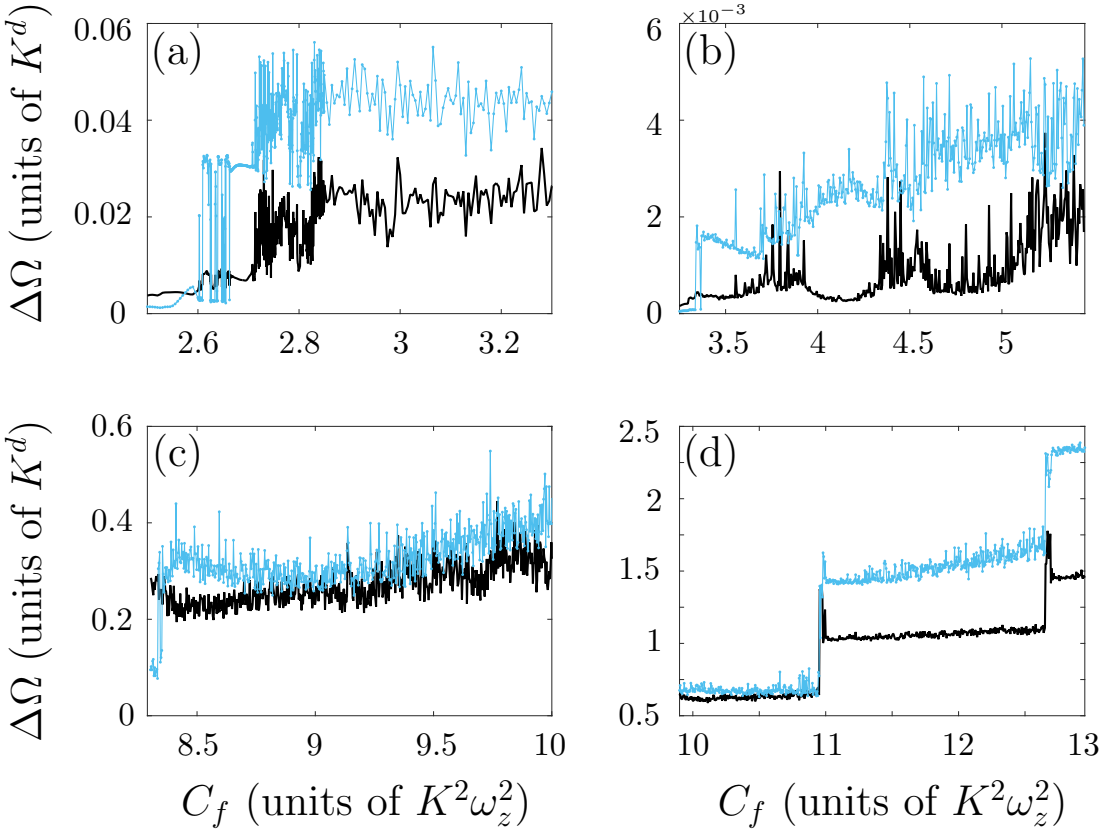

Figure 7.11: Standard deviation of Ω as a function of C_f for (a) linear chain, (b) zig-zag, (c) circle and (d) sphere configurations (black line for the large and light blue line for the small crystal)

it is rather well structured, giving immediate access to relevant information.

Focusing on the noisy character encountered for example in the case of the linear chain (fig. 7.11(a)), it turns out that this is due to multiple ion transfer processes. This can be inferred from an inspection of figure 7.12, where the behavior of $\Delta\Omega$ is compared to that of the number of transfers per ion as a function of C_f in the interval $C_f \in [2.6, 2.85]$. Obviously, every small change in the transfer dynamics results in a substantial change in the standard deviation of the Voronoi measure $\Delta\Omega$, yielding the highly irregular pattern of the latter (fig. 7.12). Although there are intervals of $\Delta\Omega$ exhibiting a relatively smooth behavior as a function of C_f (especially for lower values of C_f), the overall pattern for the zig-zag and the circle configurations (figs. 7.11 (b), (c)) is quite noisy and resembles the case of the linear chain (figs. 7.11 (a), 7.12). In contrast, for the case of the spherical configuration (fig. 7.11 (d)) a rather regular behavior of $\Delta\Omega$ as a function C_f can be observed.

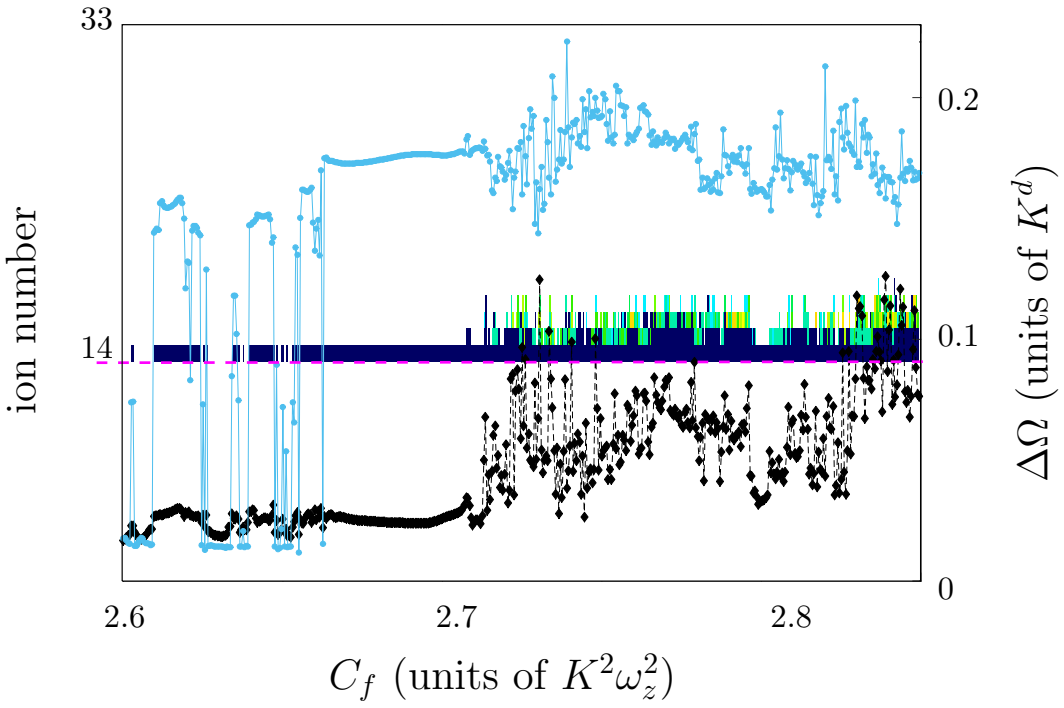

Figure 7.12: Standard deviation and number of transfers per ion for the linear chain configuration in the range $C_f \in [2.6, 2.85]$ (black dashed line with diamonds for the large crystal and light blue line with dots for the small crystal). The course of the Voronoi measure, especially for the small crystal (light blue line with dots), is strongly correlated to the number of transfers.

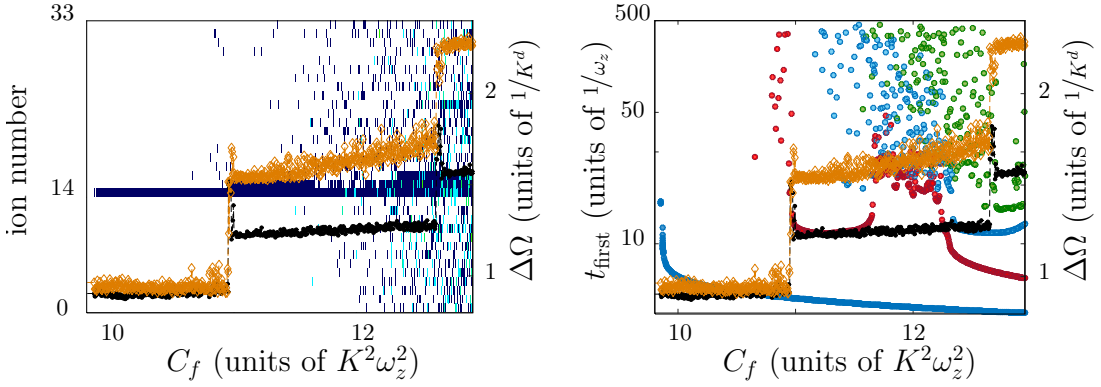

Figure 7.13: Standard deviation of the spherical configuration (black line with dots for the large and orange (gray) line with diamonds for the small crystal) combined with (a) the number of transfers per ion and (b) the time instant of the first transfer of ions (for the first 4 traveling ions marked with dots of different colors)

Note here that among others the Voronoi measure and its standard deviation depend also on the dimensionality of the configurations (eq. 6) and the space available for motion. Therefore, the values of $\Delta\Omega$ for the three-dimensional configuration (fig. 7.11 (d)), where the available volume for the corresponding motion is greatly enhanced, are orders of magnitude larger than those of lower dimensionality (fig. 7.11 (a)-(c)). This results in the former being less sensitive to small deviations, yielding the overall regular pattern of $\Delta\Omega$ for the case of spheres.

In particular, it is observed that $\Delta\Omega$ exhibits a quite smooth step-like behavior interrupted by pronounced peaks as C_f increases. In order to understand this behavior, the C_f- dependence of the two quantities characterizing the ion transfer, i.e. the number of times each ion in the Coulomb crystal travels back and forth between the two potential wells (fig. 7.13 (a)) and the time instant at which an arbitrary ion passes above the barrier for the first time (fig. 7.13 (b)), are compared. For a large range of C_f, in which an additional ion transfer occurs, the standard deviation of the Voronoi measure $\Delta\Omega$ possesses a peak, followed thereafter by the step-like behavior of the other quantities (figs. 7.13 (a) and (b)). This can be interpreted as an increase of the structural disorder in the two crystals induced by the increasing number of ion transfer processes. This is maximized each time a new ion gets transferred.

7.2 Conclusions

A quench of the potential barrier height in the double well potential occupied by CCs of different sizes introduces complex dynamics governed by ion transfer processes from one well to the other, depending on the quench amplitude. The time instant at which an arbitrary ion passes the barrier for the first time shows a step-like behavior as a function of the quench amplitude. Analyzing the crystal dynamics, it turns out that the quantities determining whether ion transfer finally occurs are the center of mass motions of both crystals and the oscillation frequencies of the innermost ion. Following the ion transfer, the dynamics of the two crystals becomes rather irregular and is characterized by structural disorder as well as reordering of the particles. A good quantity to characterize the crystalline order is the so-called Voronoi measure. Its standard deviation in time reflects well the degree of the structural disorder resulting from the quench and serves as a good indicator for the ion transfer processes.

CHAPTER 8

Conclusions and future directions

Coulomb crystals are fascinating objects which can be used to study linear [31, 110] and non-linear dynamics of ions [52, 56]. In recent years, the development of segmented Paul traps [40, 41] opened new research fields with a manifold of physical questions, concerning transport [42], splitting of Coulomb crystals (CCs) [43–46] or the coupling of individual ionic structures [106, 109].

The presented work investigates the equilibrium states of coupled CCs in a double well potential which is disturbed by either a displacement of an outer ion or a quench of the barrier height.

In chapter 5, the symmetric double zig-zag chain configuration is disturbed by the displacement of an edge ion. The perturbation of the system results in an energy transfer between the crystals. This transfer can be observed as longitudinal and transversal waves as well as shock waves which run through the crystal and are reflected at or transmitted through the barrier due to the Coulomb coupling. Multiple reflections and transmissions, phase shifts and the coupling of the radial and the axial directions result in rich wave dynamics.

In chapter 6 the initial symmetric double zig-zag chain configuration is excited by a quench of the barrier height. Oscillations around the equilibrium configuration alternate between a complete loss of order in radial direction and regular patterns. Order can be observed as ions arrange in lines, arcs and cross like formations [106]. The structural dynamic is analyzed by a measure based on Voronoi diagrams [48]. Structures with a higher degree of order, e.g. arcs and lines, correspond to small values in the Voronoi measure. Furthermore, the dynamics of the crystals is analyzed in the basis of eigenvectors of the post-quench system. Population transfers from one eigenvector to the others can be observed. Some eigenvectors are coupled, their population dynamic proceed counter propagating. It is found that the analysis of the dynamics in the basis of eigenvectors is a suitable tool, as well for the investigated non-equilibrium dynamic.

The non-equilibrium dynamics of two Coulomb crystals of different sizes occupying the individual wells of a double-well potential, subject to a quench of the potential barrier height, has been explored in chapter 7. Depending on the quench amplitude, the complex dynamics is governed by ion transfers between the wells due to the asymmetric population of the wells [109]. For all investigated initial configurations the point in time at which an arbitrary ion passes the barrier for the first time exhibit a step-like dependence on the quench amplitude. By analyzing the double zig-zag chain configuration, without loss of generality, it turns out, that the main features of this dependence are determined by the center of mass motions of both crystals and the oscillation frequencies of the innermost ion, i.e. the ion closest to the barrier. Following the ion transfer, the dynamics of the two crystals become rather irregular and are characterized by structural disorder as well as reordering of the particles. As before the Voronoi measure has been used to characterize the crystalline order. Its temporal standard deviation reflects the degree of the structural disorder resulting from the quench and serves as a good indicator for the ion transfer processes well.

Possible future directions in the study of coupled Coulomb crystals include the investigation of two Coulomb crystals (with or without defects), separated by a potential barrier, which might allow a transport of medium-sized crystals (i.e., $10 - 100$ ions) as well as combining crystals. Another promising direction for future research is the non-equilibrium dynamics of Coulomb crystals in multiple-well potentials resembling the optical lattices as used in studies of ultra cold atoms [111]. Finally, an investigation of the parameter regime allowing the system to exhibit its quantum character would also be of interest. It is expected that in such a case quantum tunneling would add to the classical over-the-barrier ion transfer shown here, giving rise to even richer non-equilibrium dynamics.

8.1 Possible experimental realization

Finally, the possible parameters for the experimental realization of the presented setup, employing state of the art ion technology, is addressed. Typical experimental parameters for segmented Paul traps are $\omega_{rf}/2\pi$=(4.2 to 50) MHz and U_{rf}=(8 to 350) V with applied DC voltages in the axial direction up to 10 V [44, 112]. Depending on the ion species and trap design this result in a radial confinement frequency $\omega/2\pi$=(1 to 5) MHz and in an axial confinement frequency $\omega_z/2\pi$=(0 to 5) MHz. For the ion dynamics only the frequency ratio $\alpha = \frac{\omega}{\omega_z}$ matters and given the aforementioned frequency ranges the scenario studied in this work of $\alpha = 8.25$ could be realized choosing e.g $\omega/2\pi = 4.5$ MHz and $\omega_z/2\pi = 0.545$ MHz. The parameters z_0 and C determining the well positions and

the barrier height, respectively, depend on the axial DC voltage and the trap geometry. Thus realistic values for the former are of the order of 30 µm and for the latter up to $300\,\mu m^2 \cdot MHz^2$. The ion configurations can be imaged during their non-equilibrium dynamics by using fluorescence light [35, 44].

Bibliography

[1] L. D. Landau and E. Lifshitz, *Statistical physics, Part 1*, 2nd rev.-enlarg. ed. (Pergamon International Library of Science, Technology, Engineering, Social Studies, Oxford: Pergamon Press, and Reading: Addison-Wesley, 1969).

[2] K. Pyka, J. Keller, H. L. Partner, R. Nigmatullin, T. Burgermeister, D. M. Meier, K. Kuhlmann, A. Retzker, M. B. Plenio, W. H. Zurek, A. del Campo, and T. E. Mehlstäubler, Nat. Commun. **4**, 2291 (2013).

[3] W. Paul and H. Steinwedel, Z. Naturforschg. **8**, 448 (1953).

[4] F. Penning, Physica **3**, 873 (1936).

[5] H. Dehmelt, Rev. Mod. Phys. **62**, 525 (1990).

[6] P. H. Dawson, Int. J. Mass Spectrom. **21**, 317 (1976).

[7] R. E. March and J. F. Todd, eds., *Practical aspects of ion trap mass spectrometry: Chemical, environmental, and biomedical applications*, Vol. 3 (CRC press, 1995).

[8] A. Kreuter, C. Becher, G. Lancaster, A. Mundt, C. Russo, H. Häffner, C. Roos, J. Eschner, F. Schmidt-Kaler, and R. Blatt, Phys. Rev. Lett. **92**, 203002 (2004).

[9] M. Steiner, H. M. Meyer, C. Deutsch, J. Reichel, and M. Köhl, Phys. Rev. Lett. **110**, 043003 (2013).

[10] G. Guthöhrlein, M. Keller, K. Hayasaka, W. Lange, and H. Walther, Nature **414**, 49 (2001).

[11] J. I. Cirac and P. Zoller, Phys. Rev. Lett. **74**, 4091 (1995).

[12] D. J. Wineland, C. Monroe, W. M. Itano, D. Leibfried, B. E. King, and D. M. Meekhof, J. Res. Natl. Inst. Stan.d Technol **103**, 259 (1998).

[13] D. Kielpinski, C. Monroe, and D. Wineland, Nature **417**, 709 (2002).

[14] C. Schneider, M. Enderlein, T. Huber, and T. Schätz, Nat. Photon. **4**, 772 (2010).

[15] M. D. Hughes, B. Lekitsch, J. A. Broersma, and W. K. Hensinger, Contemp. Phys. **52**, 505 (2011).

[16] G. Wilpers, P. See, P. Gill, and A. G. Sinclair, Nat. Nanotechnol. **7**, 572 (2012).

[17] A. Härter and J. H. Denschlag, Contemp. Phys. **55**, 33 (2013).

[18] W. W. Smith, O. P. Makarov, and J. Lin, J. Mod. Opt. **52**, 2253 (2005).

[19] A. T. Grier, M. Cetina, F. Orucevic, and V. Vuletic, Phys. Rev. Lett. **102**, 223201 (2009).

[20] C. Champenois, J. Phys. B: At. Mol. Opt. **42**, 154002 (2009).

[21] D. J. Wineland and W. M. Itano, Phys. Rev. A **20**, 1521 (1979).

[22] W. Neuhauser, M. Hohenstatt, P. Toschek, and H. Dehmelt, Phys. Rev. Lett. **41**, 233 (1978).

[23] G. Morigi, J. Eschner, and C. H. Keitel, Phys. Rev. Lett. **85**, 4458 (2000).

[24] G. Morigi, Phys. Rev. A **67**, 033402 (2003).

[25] E. Wigner, Phys. Rev. **46**, 1002 (1934).

[26] J. J. Bollinger, D. J. Wineland, and D. H. E. Dubin, Phys. Plasm. **1**, 1403 (1994).

[27] D. H. E. Dubin and T. M. O'Neil, Rev. Mod. Phys. **71**, 87 (1999).

[28] M. Bonitz, P. Ludwig, H. Baumgartner, C. Henning, A. Filinov, D. Block, O. Arp, A. Piel, S. Käding, Y. Ivanov, A. Melzer, H. Fehske, and V. Filinov, Phys. Plasm. **15**, 055704 (2008).

[29] N. Kjærgaard and M. Drewsen, Phys. Rev. Lett. **91**, 095002 (2003).

[30] L. Hornekær, N. Kjærgaard, A. M. Thommesen, and M. Drewsen, Phys. Rev. Lett. **86**, 1994 (2001).

[31] G. Birkl, S. Kassner, and H. Walther, Nature **357**, 310 (1992).

[32] G. Morigi and S. Fishman, Phys. Rev. Lett. **93**, 170602 (2004).

[33] G. Morigi and S. Fishman, Phys. Rev. E **70**, 066141 (2004).

[34] J. D. Baltrusch, C. Cormick, and G. Morigi, Phys. Rev. A **86**, 032104 (2012).

[35] M. Mielenz, J. Brox, S. Kahra, G. Leschhorn, M. Albert, T. Schaetz, H. Landa, and B. Reznik, Phys. Rev. Lett. **110**, 133004 (2013).

[36] S. Ulm, J. Roßnagel, G. Jacob, C. Degünther, S. T. Dawkins, U. G. Poschinger, R. Nigmatullin, A. Retzker, M. B. Plenio, F. Schmidt-Kaler, and K. Singer, Nat. Commun. **4**, 2290 (2013).

[37] D. H. E. Dubin, Phys. Rev. Lett. **71**, 2753 (1993).

[38] S. Fishman, G. De Chiara, T. Calarco, and G. Morigi, Phys. Rev. B **77**, 064111 (2008).

[39] M. J. Madsen, W. K. Hensinger, D. Stick, J. A. Rabchu, and C. Monroe, Appl. Phys. B **78**, 639 (2004).

[40] S. A. Schulz, U. G. Poschinger, F. Ziesel, and F. Schmidt-Kaler, New J. Phys. **10**, 045007 (2008).

[41] U. Tanaka, K. Suzuki, Y. Ibaraki, and S. Urabe, J. Phys. B: At. Mol. Opt. **47**, 035301 (2014).

[42] G. Huber, T. Deuschle, W. Schnitzler, R. Reichle, K. Singer, and F. Schmidt-Kaler, New. J. Phys. **10**, 013004 (2008).

[43] T. Ruster, C. Warschburger, H. Kaufmann, C. T. Schmiegelow, A. Walther, M. Hettrich, A. Pfister, V. Kaushal, F. Schmidt-Kaler, and U. G. Poschinger, Phys. Rev. A **90**, 033410 (2014).

[44] H. Kaufmann, T. Ruster, C. Schmiegelow, F. Schmidt-Kaler, and U.G.Poschinger, New J. Phys. **16**, 073012 (2014).

[45] M. D. Barrett, J. Chiaverini, T. Schaetz, J. Britton, W. M. Itano, J. D. Jost, E. Knill, C. Langer, D. Leibfried, R. Ozeri, and D. J. Wineland, Nature **429**, 737–739 (2004).

[46] M. A. Rowej, A. Ben-Kish, B. Demarco, D. Leibfried, V. Meyer, J. Beall, J. Britton., J. Hughes, W. Itano, B. Jelenkovic, C.Langer, T. Rosenband, and D. Wineland, Quant. Inf. Comp. **2**, 257 (2002).

[47] J. Abraham and M. Bonitz, Contributions to Plasma Physics **54**, 27–99 (2014).

[48] F. P. Preparata and M. I. Shamo, *Computational geometry* (Springer Verlag, New York, 1985).

[49] F. G. Major, V. N. Gheorghe, and G. Werth, "Charged Particle Traps", in , Vol. 37, 1st ed. (Springer-Verlag Berlin Heidelberg, 2005) Chap. Buffer Gas Cooling, p. 203.

[50] M. Knoop, I. Marzoli, and G. Morigi, eds., *Ion Traps for Tomorrow's Applications*, Vol. 189 (IOS Press, 2015).

[51] D. Gerlich, Adv. Chem. Phys. **82**, 1 (1992).

[52] J. Hoffnagle, R. DeVoe, L. Reyna, and R. Brewer, Phys. Rev. Lett. **61**, 255 (1988).

[53] E. Pollock and J. Hansen, Phys. Rev. A **8**, 3110 (1973).

[54] W. M. Itano, J. J. Bollinger, J. N. Tan, B. Jelenković, X.-P. Huang, and D. J. Wineland, Science **279**, 686 (1998).

[55] H. M. Van Horn, Science **252**, 384–389 (1991).

[56] N. Kjærgaard, K. Mølhave, and M. Drewsen, Phys. Rev. E **66**, 015401 (2002).

[57] P. Herskind, A. Dantan, J. Marler, M. Albert, and M. Drewsen, Nat. Phys. **5**, 494 (2009).

[58] K. Pyka, N. Herschbach, J. Keller, and T. E. Mehlstäubler, Appl. Phys. B **114**, 231 (2014).

[59] A. Hansen, O. Versolato, L. Klosowski, S. Kristensen, A. Gingell, M. Schwarz, A. Windberger, J. Ullrich, J. Crespo López-Urrutia, and M. Drewsen, Nature **508**, 76 (2014).

[60] D. Porras and J. I. Cirac, Phys. Rev. Lett. **92**, 207901 (2004).

[61] A. Friedenauer, H. Schmitz, J. Glueckert, D. Porras, and T. Schätz, Nat. Phys. **4**, 757 (2008).

[62] D. Leibfried, R. Blatt, C. Monroe, and D. Wineland, Rev. Mod. Phys. **75**, 281 (2003).

[63] C. Monroe, D. Meekhof, B. King, W. M. Itano, and D. J. Wineland, Phys. Rev. Lett. **75**, 4714 (1995).

[64] W. Slattery, G. G.D. Doolen, and H. DeWitt, Phys. Rev. A **21**, 2087 (1980).

[65] D. J. Wineland, J. C. Bergquist, W. M. Itano, J. J. Bollinger, and C. H. Manney, Phys. Rev. Lett. **59**, 2935 (1987).

[66] F. Diedrich, E. Peik, J. M. Chen, W. Quint, and H. Walther, Phys. Rev. Lett. **59**, 2931 (1987).

[67] E. Shimshoni, G. Morigi, and S. Fishman, Phys. Rev. Lett. **106**, 010401 (2011).

[68] S. Earnshaw, Trans. Camb. Phil. Soc **7**, 97 (1842).

[69] A. Ashkin, Phys. Rev. Lett. **24**, 156 (1970).

[70] A. Ashkin and J. Dziedzic, Appl. Phys. Lett. **19**, 283–285 (1971).

[71] K. Neuman and S. Block, Rev. Sci. Instr. **75**, 2787 (2004).

[72] R. Grimm, M. Weidemüller, and Y. B. Ovchinnikov, "Optical dipole traps for neutral atoms", in *Advances in atomic, molecular, and optical physics*, Vol. 42 (Elsevier, 2000), pp. 95–170.

[73] G. Gabrielse and H. Dehmelt, Phys. Rev. Lett. **55**, 67 (1985).

[74] L. S. Brown and G. Gabrielse, Rev. Mod. Phys. **58**, 233 (1986).

[75] W. Paul, Rev. Mod. Phys. **62**, 531 (1990).

[76] N. W. McLachlan, *Theory and application of mathieu functions* (Clarendon Press, 1951).

[77] M. Abramowitz, I. A. Stegun, et al., *Handbook of mathematical functions with formulas, graphs, and mathematical tables*, Vol. 9 (Dover, New York, 1972).

[78] D. Berkeland, J. Miller, J. Bergquist, W. Itano, and D. Wineland, J. Appl. Phys. **83**, 5025–5033 (1998).

[79] H. Kaufmann, S. Ulm, G. Jacob, U. Poschinger, H. Landa, A. Retzker, M. B. Plenio, and F. Schmidt-Kaler, Phys. Rev. Lett. **109**, 263003 (2012).

[80] J. Keller, H. Partner, T. Burgermeister, and T. Mehlstäubler, J. Appl. Phys. **118**, 104501 (2015).

[81] G. Berman, D. James, R. Hughes, M. Gulley, M. Holzscheiter, and G. López, Phys. Rev. A **61**, 023403 (2000).

[82] D. F. James, Phys. Rev. Lett. **81**, 317 (1998).

[83] S. Brouard and J. Plata, Phys. Rev. A **63**, 043402 (2001).

[84] J. Cirac, L. Garay, R. Blatt, A. Parkins, and P. Zoller, Phys. Rev. A **49**, 421 (1994).

[85] Y. E. Lozovik, Soviet Physics Uspekhi **30**, 912 (1987).

[86] H. Dehmelt, W. Nagourney, and J. Sandberg, Proceedings of the National Academy of Sciences of the United States of America **83**, 5761 (1986).

[87] D. Möhl, G. Petrucci, L. Thorndahl, and S. Van Der Meer, Phys. Rep. **58**, 73 (1980).

[88] R. G. Gould, in The Ann Arbor conference on optical pumping, the University of Michigan, edited by P. Franken and R. Sands (1959), p. 128.

[89] T. Maiman, Solid-state Electronics **4**, 236 (1962).

[90] H.-W. Jiang and A. J. Dahm, Phys. Rev. Lett. **62**, 1396 (1989).

[91] V. J. Goldman, M. Santos, M. Shayegan, and J. E. Cunningham, Phys. Rev. Lett. **65**, 2189 (1990).

[92] J. Eschner, G. Morigi, F. Schmidt-Kaler, and R. Blatt, J. Opt. Soc. Am. B **20**, 1003 (2003).

[93] E. Peik, J. Abel, T. Becker, J. Von Zanthier, and H. Walther, Phys. Rev. A **60**, 439 (1999).

[94] C. Roos, D. Leibfried, A. Mundt, F. Schmidt-Kaler, J. Eschner, and R. Blatt, Phys. Rev. Lett. **85**, 5547 (2000).

[95] K. R. Brown, C. Ospelkaus, Y. Colombe, A. C. Wilson, D. Leibfried, and D. J. Wineland, Nature **471**, 196 (2011).

[96] M. Harlander, R. Lechner, M. Brownnutt, R. Blatt, and W. Hänsel, Nature **471**, 200 (2011).

[97] A. I. Streltsov, O. E. Alon, and L. S. Cederbaum, Phys. Rev. A **73**, 063626 (2006).

[98] M. O. Steinhauser, *Computer simulation in physics and engineering* (Walter de Gruyter, 2013).

[99] M. Galassi, J. Davis, J. Theiler, B. Gough, G. Jungman, P. Alken, M. Booth, and F. Rossi, *GNU Scientific Library Reference Manual*, edited by B. Gough, 3rd (Network Theory Ltd., 2009).

[100] G. Piacente, I. V. Schweigert, J. J. Betouras, and F. M. Peeters, Phys. Rev. B **69**, 045324 (2004).

[101] P. Ludwig, S. Kosse, and M. Bonitz, Phys. Rev. E **71**, 046403 (2005).

[102] R. W. Hasse and V. V. Avilov, Phys. Rev. A **44**, 4506 (1991).

[103] V. M. Bedanov and F. M. Peeters, Phys. Rev. B **49**, 2667–2676 (1994).

[104] K. E. Atkinson, *An introduction to numerical analysis* (John Wiley & Sons, 2008).

[105] M. Bussmann, U. Schramm, T. Schätz, and D. Habs, Journal of Physics A: Mathematical and General **36**, 6119 (2003).

[106] A. Klumpp, B. Liebchen, and P. Schmelcher, Phys. Lett. A **380**, 2644 (2016).

[107] H. Goldstein, C. P. Poole, and J. L. Safko, *Classical Mechanics: Pearson New International Edition*, edited by P. H. Ed. (Harlow, 2014).

[108] H. Landa, A. Retzker, T. Schätz, and B. Reznik, Phys. Rev. Lett. **113**, 053001 (2014).

[109] A. Klumpp, A. Zampetaki, and P. Schmelcher, Phys. Rev. E **96**, 032227 (2017).

[110] M. G. Raizen, J. M. Gilligan, J. C. Bergquist, W. M. Itano, and D. J. Wineland, Phys. Rev. A **45**, 6493 (1992).

[111] I. Bloch, Nature Physics **1**, 23 (2005).

[112] W. K. Hensinger, S. Olmschenk, D. Stick, D. Hucul, M. Yeo, M. Acton, L. Deslauriers, C. Monroe, and J. Rabchuk, Appl. Phys. Lett. **88**, 034101 (2006).

List of Movies

[M.1] zigzagRadialDisplacement.avi,
Two zig-zag chains of equal sizes are excited by the radial displacement of an edge ion. (2018).

[M.2] zigzagAxialDisplacement.avi,
Two zig-zag chains of equal sizes are excited by the radial displacement of an edge ion. (2018).

[M.3] Shockwave.avi,
The initial configuration are two equal sized linear chains. The axial displacement of an edge ion results in ashock wave traveling through crystal **1** and is mainly reflected on the barrier. (2018).

[M.4] zigzagSymmetric.avi,
The initial configuration is the energetically lowest state of two equal sized zig-zag chains (22 ions in each well). The quench of the barrier leads to a manifold of structures like arcs, circles and crosses alternated by disorder which follows up in the corresponding dynamic. (2016).

[M.5] IonTransferLinearChain.avi,
Two linear ion chains of different sizes (13 and 20 ions) are trapped in a double well potential. A quench of the barrier results in ions transfer. In contrary to the zig-zag chain configuration we find a rich tranfers dynamic of ions before the left crystal becomes bigger then the right one. (2017).

[M.6] IonTransferZigZag.avi,
The initial configuration is the energetically lowest state of two zig-zag chains of different sizes (13 and 20 ions). A quench of the barrier allows ions to travel over the barrier. In the bigger crystal the ion transfer results in small nonlinear oscillations of the ions around their equilibrium positions and a center of mass motion of the complete crystal. In the small crystal the center of mass motion is superposed with chaotic oscillations of the individual ions. (2017).

[M.7] IonTransferCircle.avi,
The initial configuration is the energetically lowest state of a circle configuration of different sizes (13 and 20 ions). A quench of the barrier allows ions to travel over the barrier. In the bigger crystal the ion transfer results in small nonlinear oscillations of the ions around their equilibrium positions and a center of mass motion of the complete crystal. (2017).

Danksagung

Mein besonderer Dank gilt meinem Doktorvater, Prof. Dr. Peter Schmelcher, für die Möglichkeit, in seiner Gruppe promovieren zu dürfen, und seine Betreuung meines Promotionsvorhabens. Für die Zeit und den Aufwand bei der Begutachtung meiner Arbeit bedanke ich mich bei Prof. Dr. Ludwig Mathey.

Für die vielen wissenschaftlichen Diskussionen, Ratschläge, Korrekturen bezüglich meiner schriftlichen Darlegungen und seiner umfassenden Unterstützung möchte ich Stephan Klumpp danken. Ohne ihn wäre diese Arbeit nicht zustande gekommen.

Um ein Kind großzuziehen benötigt man ja bekanntlich ein ganzes Dorf, um eine Dissertation zu schreiben eine ganze Arbeitsgruppe. In der Arbeitsgruppe haben mir viele mit Rat und Tat geholfen. Daher ein Danke an Alexandra Zampetaki, Christoph Petry, Jan Stockhofe, Sven Krönke, Johannes Schurer und Benno Liebchen für ihre Geduld und Hilfe bei wissenschaftlichen Diskussionen und dem Schreiben von Veröffentlichungen.

Für das sorgfältige Lesen meiner Dissertation gilt mein Dank außerdem Fabian Köhler, Christian Fey, Kevin Keiler, Maxim Pyzh, Aritra Mukhopadhyay, Jie Chen, Christian Morfonios, Frederic Hummel and Till Jahnke.

Vielen Dank an alle in der Arbeitsgruppe für die schöne Zeit und die aufmunternden Worte, wenn ich am Verzweifeln war. Speziell möchte ich der guten Seele der Arbeitsgruppe Anja Cordes danken für die unbürokratische Hilfe bei bürokratischen Problemen sowie für die netten Gespräche und kleinen Tipps.

Zu guter Letzt, aber genauso wichtig, möchte ich meiner Familie und meinen Freunden für die Unterstützung danken: Meinen Eltern für die schöne Kindheit, meinem Bruder, bei dem ich gelernt habe mich durchzusetzen, meinem Mann für seine Geduld, Hilfe und Ruhe, Thomas L. Klumpp, meinem Sohn, dafür, dass er existiert und meinen Freunden für die vielen schönen Spieleabende und Gespräche.

Eidesstattliche Versicherung / Declaration on oath

Hiermit versichere ich an Eides statt, die vorliegende Dissertationsschrift selbst verfasst und keine anderen als die angegebenen Hilfsmittel und Quellen benutzt zu haben.

Die eingereichte schriftliche Fassung entspricht der auf dem elektronischen Speichermedium.

Die Dissertation wurde in der vorgelegten oder einer ähnlichen Form nicht schon einmal in einem früheren Promotionsverfahren angenommen oder als ungenügend beurteilt.

Hamburg, den 2. Juli 2018 _____